Size Effects in Nanoscale Structural Phenomena

By

Kyle Matthew McElhinny

A dissertation submitted in partial fulfillment of

the requirements for the degree of

Doctor of Philosophy

(Materials Science)

at the

University of Wisconsin- Madison

2017

Date of final oral examination: 05/25/2017

The dissertation is approved by the following members of the Final Oral Committee:

Paul Evans, Professor, Materials Science and Engineering
Max Lagally, Professor, Materials Science and Engineering
Padma Gopalan, Professor, Materials Science and Engineering
Xudong Wang, Associate Professor, Materials Science and Engineering
Randall Goldsmith, Assistant Professor, Chemistry

Abstract

The creation of nanostructures offers the opportunity to modify and tune properties in ways inaccessible in bulk materials. A key component in this development is the introduction of size effects which reduce the physical size, dimensionality, and increase the contribution of surface effects. The size effects strongly modify the structural dynamics in nanoscale systems and leads to changes in the vibrational, electrical, and optical properties. An increased level of understanding and control of nanoscale structural dynamics will enable more precise control over nanomaterial transport properties.

My work has shown that 1-D spatial confinement through the creation of semiconducting nanomembranes modifies the phonon population and dispersion. X-ray thermal diffuse scattering distributions show an excess in intensity for nanomembranes less than 100 nm in thickness, for phonon modes with wavevectors spanning the entire Brillouin zone. This excess intensity indicates the development of new low-energy phonon modes or the softening of elastic constants. Furthermore, an additional anisotropy in the phonon dispersion is observed with a symmetry matching the direction of spatial confinement. This work has also extended x-ray thermal diffuse scattering for use in studying nanomaterials.

In electro- and photoactive monolayers a structural reconfiguration can be produced by external optical stimuli. I have developed an electro- and photoactive molecular monolayers on oxide surfaces. Using x-ray reflectivity, I have evaluated the organization and reconfiguration of molecular monolayers deposited by Langmuir-Blodgett technique. I have designed and probed the reconfiguration of optically reconfigurable monolayers of azobenzene donor molecules on semiconducting surfaces. These monolayers reconfigure through a cooperative switching process leading to the development of large isomeric domains. This work represents an

advancement in the interpretation of x-ray reflectivity from molecular monolayers and inhomogeneous surfaces.

The growth 2D materials depends on the interactions between the substrate and the 2D material. I have studied the competition between kinetics and surface energetics which lead to a faceted Ge surface during the growth of Graphene nanoribbons. As part of this work, I have developed new methodologies for interpreting x-ray reflectivity patterns from surfaces with multiple reflections. A systematic analysis of the temperature dependence of the faceting process indicates that the process is thermodynamically dominated at high temperatures.

Acknowledgements

I would not have been able to complete this work without the time and effort of my colleagues, collaborators, friends, family members, and mentors.

Thanks to my advisor Paul Evans for never losing his passion and enthusiasm for science even when I did through the ups and downs of my academic career. His hard-nosed approach to approach to scientific investigation and communication represents the best what the scientific community should stand for. I am a better experimentalist, scientist, writer, and presenter for having been in his group these past years.

Thanks to the current and former members of the Evans group who helped me over the years. Thanks to Josef Spalenka, Pice Chen, Margaret Cosgriff, and Sarah Thompson for getting my through the hurdles of my first few years of study and always lending an ear to the questions of an inexperienced researcher. Thanks to Jack Tilka, Joonkyu Park, Yajin Chen, Youngjun Ahn, Arunee Lakkham, Qingteng Zhang, Humed Yusef, and Anatasios Pateras for experimental manpower, productive discussions, and putting up with my attempts to organize the group into a more cohesive, collaborative, and close knit group. I truly hope I have left the group in a better place from my being a part of it. A special thanks to Gokul Gopalakrishnan who taught me so much about science and research and with whom I have had so many scientific adventures. Our work together makes up significant portions of Chapters 2 and 3.

Thanks to my collaborators especially to those in the Materials Research Science and Engineering Center. I greatly valued the interdisciplinary nature of the group and the many fruitful discussions and new friendships formed as part of this group. In particular, thanks to Yongho Joo and Prof. Padma Gopalan with I whom I had the privilege of publishing a few papers with. Yongho and Padma were always open to discussing questions, confusions, and

humoring my requests for additional samples. My work with Yongho Joo and Padma Gopalan makes up a significant portion of Chapter 4. I'd also like to give a great thanks to Bobby Jacobberger, Yu Liu, Stephany Herrara-Posada, Prof. Howard Katz, and Prof. Mike Arnold for introducing me to new opportunities to collaborate on publications outside my field and satiate my scientific curiosity. My work with Bobby Jacobberger and Mike Arnold makes up a significant portion of Chapter 5. Thanks to Prof. Kenji Sakurai, Jinxing Jiang, Yuwei Liu, Wenyang Zhao, and Megumi Iwamoto for being gracious hosts during my summer in Tsukuba Japan at the National Institute for Materials Science. I hope that when you visit the United States I can been as accommodating and informative host for you as you all were for me. My work with Kenji Sakurai makes up a significant portion of Chapter 4.

Thanks to my thesis committee, Max Lagally, Padma Gopalan, Xudong Wang, and Randall Goldsmith for their valuable input and constructive criticism that has often forced me to confront difficult questions, and for the reminders that there is always another level of excellence that can be achieved with a little extra work and careful thought.

Thanks to the Madison Ultimate Frisbee Association and Wisconsin Shorin-Ryu Karate for providing an outlet for the stress of graduate studies and a perspective possible only through friendships which extend beyond the ivory tower.

Thanks to my parents Matt and Sandy for encouraging my innate curiosity, providing the means for me to devote 10 years of my life to scientific study thanks to their hard work, and of course teaching me to balance my units from an early age. Thanks to my brother Ryan playing big brother as he stepped out into the real world before me. Thanks to my dog Lily who's love of the outside, innate joy with life, and boundless curiosity have kept me healthier and happier since she entered my life.

Finally, thanks to my wonderful wife, Megan, for her encouragement and patience during our first year of marriage, which overlapped with both my final year of graduate school and her final year of medical school. If nothing else good comes of my time during graduation school, I will always have you because of it. We never do things the easy way, but the universe hasn't been able to stop us yet. I look forward to many more adventures.

Table of Contents

List of Figures

List of Tables

List of Equations

Chapter 1: Motivation and Introduction

1.1 Motivation and overview

Synthesis-structure-property relations dominate the design and study of materials, particularly in nanoscience and nanotechnology. In nanoscience and nanotechnology controlling the physical size and molecular-scale structure provides an opportunity to create and tune properties in ways inaccessible in bulk materials. There are three primary size effects in nanomaterials. The first is the reduced physical dimensions down to the nm length scale. The second is the reduced dimensionality of the crystal from 3D bulk crystals, to 2D materials like membranes and monolayers, to 1D materials like nanowires and nanotubes, and 0D materials like quantum dots. The third is the increased importance of interfaces as a result of the increased surface area to volume ration. The important length scale for thermal and electrical transport is set by a combination of the mean free path and the wavelength of the phonon or electron being confined. This sets the critical length scale for confinement effects near 30 nm.

The problem addressed in this thesis is the impact of the size effects on the structural dynamics on nanomaterials. Changes in the atomic displacements of the atoms on the order of 0.01 Å RMS displacement impact the thermal and electronic properties of the nanostructure. Surface confinement and close packing in 2D molecular monolayers turn the 1 nm displacement from changes in molecular conformation result in orders of magnitude changes in charge transfer rates. Surface energetics between graphene and Ge control faceting at the interface at length scales less than 10 nm.

The goal is that if the dynamics can be characterized and controlled at sub-nm length scales, this will enable precise control over the nanoscale transport properties. With this increased

understanding and control challenges in thermal management in transistors, waste heat harvesting in thermoelectrics, control over charge transport and energy storage in carbon nanomaterials, and more efficient interfacial charge transfer can be overcome. The experimental challenge for nanostructures, monolayers, and surfaces is to characterize the structure in small volumes. However, with recent advances in x-ray scattering techniques and sample preparation, it is now possible to probe the modifications of structural phenomena introduced by material interfaces and surfaces.

Several recent research efforts across the scientific community have worked to isolate modifications to the phonon dispersion in an effort to advance the phonon engineering of materials. The goal of my work has been to determine how the phonon dispersion is modified by spatial confinement through the creation of 2D semiconductor nanomembranes. Research pursuits in the development of intelligent materials which enable external dynamic control over material structure have worked to develop of a model for the structural reconfiguration of optically reconfigurable monolayers. The goal of my work has been to obtain detailed structural information on the structural evolution of molecular monolayers via photoisomerization. The growth of 2D materials has blossomed in recent years with the competition between surface kinetics and thermodynamics during the growth of 2D materials playing a central role in their development. The goal of my research has been to understand the development of surface facets during the nanomaterial growth process.

These projects are unified by the drive to use nanotechnology to manipulate the properties of materials, particularly, to understand the role of spatial confinement on the structure and hence other physical properties of the system. Additionally, these projects demonstrate the role of fast dynamics in the vibrational phenomena in nanoscale materials. Finally, these projects have been

enabled by the advances in x-ray scattering techniques and nanofabrication. The controllable nanoscale structures and high fluxes of synchrotron x-ray sources have allowed me to study subtle nanoscale phenomena and the corresponding weak x-ray signatures.

The field of phonon-engineering has blossomed with the goal of obtaining comparable control of nanoscale vibrational properties as has been achieved for electronic and optical properties.[1–5] Improved control over the vibrational properties of nanomaterials is central to more efficient thermoelectrics through reducing the thermal conductivity and breaking the Wiedemann–Franz law,[6–14] the development of phononic crystals for a variety of applications including acoustic waveguides through the creation of a phononic band gap,[2,15–19] and heat removal and electron-phonon scattering in microelectronics.[20–26] In nanomaterials, mechanically-free surface boundary conditions replace the periodic boundary conditions of bulk crystals.[21,26–28] Changing the boundary conditions results in modification of the fundamental vibrational modes of the crystal when the confined dimension becomes comparable in length to the phonon mean free path of the material, on the order of tens of nanometers in Si.[7,21,28,29]

I have used x-ray scattering methods to address a long-standing problem underpinning the fundamental understanding of thermal transport in nanomaterials. Understanding changes in the phonon dispersion in nanoscale semiconductor structures is key for understanding thermal transport and electron-phonon interactions which play an important role in determining the properties and functionalities in these systems.[24,25,30,31] The key challenge has been the lack of an experimental probe capable of probing the small volumes of nanostructures with sufficient probe momentum to sample phonons with arbitrary wavevectors anywhere in the Brillouin zone. In bulk materials inelastic neutron scattering is used to measure the phonon dispersion. However, the volumes required for phonon measurements using neutron scattering on a

reasonable timescale are on the order of 1000s of μm^3, while the volumes available in nanomaterials are on the order of μm^3.[32] Instead, optical techniques have been extensively used to probe phonons in nanoscale volumes.[29,33–37] However, the inherent limitation of these techniques is that the optical photon momenta in Raman and Brillouin Light Scattering measurements is capable of sampling only 10^{-9} of the phonon modes of the crystal.[29, 33–37]

My solution has been to use x-ray thermal diffuse scattering to probe the population of phonons, and hence the modification of the phonon dispersion, in semiconductor nanomembranes with thicknesses as thin a 6 nm.[38–42] X-ray TDS is capable of probing small volumes through the use of high flux synchrotron x-ray sources. Additionally, the x-ray photon momenta on the order of 1 $Å^{-1}$ is large enough to probe phonons spanning the Brillouin zone. Chapters 2 and 3 outline the fabrication of nanomaterials and development of x-ray TDS tools to investigate the impact of spatial confinement on the phonon dispersion.

My second research area has focused on donor-semiconductor interfaces and reconfigurable monolayers. In donor-semiconductor systems the charge transfer rate and mechanism depend on the molecular structure as well as the conformation and configuration of molecules at the interface.[43–52] Charge transfer across the organic-inorganic interface is crucial to applications in solar energy harvesting,[53–55] photo- and electro-catalysis,[56,57] and molecular electronics and sensing applications.[58,59] In reconfigurable monolayers, which undergo a reversible change in molecular conformation through photoisomerization, the molecular structure, restricted free volume, and steric hindrance reduce photoisomerization rates and can limit the fraction the monolayer which reconfigures.[60–63] Optical reconfiguration has been developed for use in a variety of exciting applications including phostoswitchable surfaces,[64–66] high density solar fuels,[67–70] gas storage in metal-organic frameworks,[71] and as parts in molecular machines.[64, 65, 72–

[74] In molecular monolayers, the introduction of a surface results in anisotropic confinement of the molecular orientation to a particular geometry on the surface. This confinement to a surface, rather than the isotropic distribution present in solution, results in a complex dependency on the charge transfer and photoisomerization rates due to structural variation and intermolecular interactions.

I have used x-ray scattering methods to address the need for a structural probe capable of characterizing monolayer structural parameters and structural variation of the interface. Recent experimental and theoretical results for these donor-semiconductor systems have demonstrated the importance of molecular conformation and configuration on the electronic and vibrational properties of the interfacial system.[43,45,47] In donor-semiconductor monolayers, spectroscopic techniques have been used to infer the distance and orientation of donor molecules on the surface through measurements of the charge transfer rate.[45, 46] However, the charge transfer rate is a complex parameter which depends on a variety of other parameters and provides an indirect estimate of the monolayer structure. In reconfigurable monolayers, the photoisomerization kinetics are also evaluated using spectroscopic techniques such as UV-vis spectroscopy and sum-frequency generation spectroscopy. These spectroscopy techniques provide only indirect estimates of the timescale and evolution of photoisomerization within the monolayer.

I have addressed the problem of the determining the interfacial structure of donor-semiconductor and reconfigurable monolayers by using x-ray reflectivity (XRR). I have used the XRR signal as an indicator of the influence of the deposition parameters and molecular design on the interfacial structure and structural variation.[49, 75] Additionally, I have developed and characterized a donor-semiconductor system with tunable molecular conformation and configuration to enable studies of the structural impact of these two parameters on the resulting

properties. Chapter 4 discusses the development of XRR as a monolayer structural probe, the creation of reconfigurable electronic monolayers, and the development of a structural model for understanding the monolayer reconfiguration.

Finally, I have used x-ray scattering methods to evaluate the competition between the surface kinetics and thermodynamics during 2D materials growth. Advances in the development of two-dimensional materials have produced impressive new functionalities, but have also posed significant characterization challenges as a result of the small sample thickness and corresponding broadness of the reciprocal space features. This has made characterization using laboratory-based diffraction instrumentation challenging. My work has demonstrated that XRR can resolve this issue by leveraging simultaneous advances in x-ray sources, optics, area detectors, and reflectivity modeling. Without precise scattering measurements of the faceted structures, the atomic-scale structure is unknown. In particular, my reflectivity study of a high-angle-faceted graphene/Ge(001) interface provides timely and crucial insight into the interplay between surface energetics and kinetics in single-layer graphene/Ge systems.[76, 77] My work interprets multiple reflections from a single surface to extract statistical parameters of distribution of faceting angles with an accuracy of 0.1º. It also looks at the temperature dependence of this surface faceting to illuminate the competition between the surface kinetics and thermodynamics during graphene growth. This work opens the way to examine similar crucial issues in other emerging 2D materials including the transition metal dichalcogenides, silicene and germanene.

This thesis is divided into chapters: Chapter 1 provides the relevant background for the x-ray scattering techniques used as the primary characterization tools throughout this thesis.

Specific comments on my role in the development and advancement of the experimental and analytical methodologies are also discussed.

Chapter 2 discusses the development of processing techniques to eliminate the buckling instability in freestanding semiconductor nanomembrane windows through understanding the mechanics and surface energetics of the nanomembrane system during processing. The key results of this chapter include the development of an edge-induced flattening technique to produce silicon nanomembrane windows as thin as 6 nm with as little as 10 nm of vertical deviation over a 100 μm length scale. A second technique which confines the majority of buckling instability into narrow arms which attach the nanomembrane the surround substrate is developed to flatten Si/SiGe/Si nanomembranes. The additional technique is required as a result of additional contributions to the strain energy from the lattice mismatch between Si and Ge.

Chapter 3 describes the discovery of large-wavevector phonon confinement in Si and SiGe nanostructures through the use of x-ray TDS. The development of x-ray TDS as a nanoscale phonon probe is discussed. The key scientific results are the observation of evidence for phonon confinement at wavevectors spanning the entire Brillouin zone as well as the development of a three-dimensional anisotropy in the phonon population resulting from the mesoscopic structure of the nanomembrane.

Chapter 4 discusses the development and structural evolution of optically reconfigurable electronic monolayers through collaboration with Padma Gopalan's group and characterization of the static and dynamic monolayer structure using XRR. The key scientific result is the development of a structural model for the evolution of the monolayer in response to optical stimulus.

Chapter 5 outlines characterization of the competing kinetics and thermodynamics of a faceting process of a Ge surface during the growth of graphene nanoribbons. This chapter discusses the interpretation of the reflectivity patterns from a surface with multiple reflecting surfaces as well as reveals that the thermodynamics of the Ge-graphene system dominate at high temperatures.

1.2 X-ray scattering techniques: background

1.2.1 X-Ray thermal diffuse scattering: review

X-ray thermal diffuse scattering (TDS) describes phenomena associated with the scattering of x-rays by thermal lattice vibrations. Thermal lattice vibrations reduce the intensity of the Bragg peak by the Debye-Waller factor and redistribute the scattered x-rays across broad regions of reciprocal space.[78, 79] The momentum of x-ray photons used for TDS experiments is approximately 10 $Å^{-1}$. This is the same order of magnitude as the dimensions of the Brillouin zone that is used to describe the dispersion of phonons. Due to advances in synchrotron sources and x-ray optics, small spot sizes with high x-ray flux can be focused on small sample volumes.

A brief review of the origin of TDS is useful in understanding the how it can be used. Derivations in more detail than the summary presented here are available in the textbooks by Warren,[78] Als-Nielsen and McMorrow,[79] and Cohen and Schwartz.[80] Bragg diffraction is characterized by sharp peaks in reciprocal space. In real space, Bragg diffraction arises from the constructive interference of waves scattered from atomic planes. Bragg diffraction occurs when the path length difference between x-rays reflecting from different planes is an integer multiple of the x-ray wavelength. In reciprocal space, the diffraction condition requires that the scattered wavevector $\boldsymbol{S}$ is equal to a reciprocal lattice vector $\boldsymbol{G_{hkl}}$. $\boldsymbol{G_{hkl}}$ is perpendicular to the atomic plane

with indices (h k l) and has a magnitude of $2\pi/d_{hkl}$. Bragg reflections produce sharp peaks of intensity in reciprocal space because a Fourier transform relates the real space and reciprocal space structure. The Fourier transform of the infinite real-space lattice is a delta function.

Scattering amplitude from a static lattice can be modified to account for thermal vibration by replacing R_n, the time-averaged mean position, with the instantaneous position term, $R_n + u_n$ where u_n is the displacement from R_n. This replacement leads to the separation of the scattered intensity into two terms. The first term is the elastic scattering from the lattice where the atomic form factor has been reduced by an exponential term known as the Debye-Waller factor. This factor reduces the intensity of the Bragg peak, but does not broaden it. The second term is termed as first-order TDS. The intensity of TDS increases with increasing mean-square displacement and it is distributed over a width determined by the correlation of the displacements of its neighboring atoms. Due to the diffuse nature of TDS, the scattering contribution is spread out over large volumes of reciprocal space. Since TDS arises from the instantaneous displacements of the vibrating atoms, it provides information about the population and dispersion of phonons.

TDS is an energy-integrated analog of inelastic x-ray scattering capable of simultaneously probing phonons throughout the entire Brillouin zone. The TDS intensity distribution depends on the phonon dispersion and the polarization of the of the thermally populated phonon modes. The TDS intensity distribution is a direct indication of the phonon population at a given wavevector and temperature. The first-order TDS intensity for an infinitely periodic crystal at scattering wavevector $\boldsymbol{S}$ and sample temperature T, is given by Equation 1-1:[78]

$$I_1(\boldsymbol{S}) = C\,|f(\boldsymbol{S})|^2 e^{-2M} \sum_{j=1}^{6} \frac{\left|S \cdot \hat{e}_j\right|^2}{\omega_{Q,j}} coth\left(\frac{\hbar\omega_{Q,j}}{2k_B T}\right)$$

Equation 1-1

where ***S*** is the scattered x-ray vector, ***f(S)*** is the atomic scattering factor, *M* is the Debye-Waller factor, $\hat{e}_j$ is the phonon polarization, $\omega_{Q,j}$ is the dispersion of the jth phonon branch as a function of phonon wavevector Q, k_B is Boltzmann's constant and *T* is temperature. The *coth* () factor is derived from the mean total energy of a harmonic oscillator. The sum over *j* is the sum over all phonon branches, for a total of six phonon branches for crystal structures such as silicon that form crystals in which the unit cell has a two-atom basis. The constant *C* is related to the total number of atoms in the crystal, the mass of atoms involved in the vibration, and the thermal energy available. This constant is absorbed by the scaling parameter during TDS analysis, due to the difficultly of calculating the exact numerical value of the expected intensity. A complete discussion of TDS from an extended solid can be found in ref. 78.

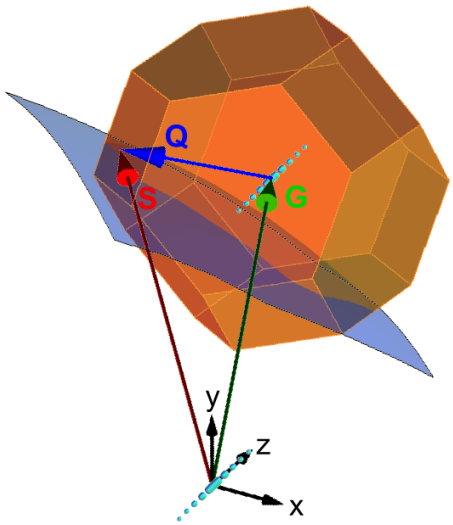

Figure 1-1: First-order thermal diffuse scattering with a momentum transfer S arises from phonons with wave vector Q. G is the reciprocal lattice vector closest to S. Bragg reflections from silicon membranes are elongated into rods of intensity along the direction normal to the surface of the membrane. The reciprocal-space representation of the x-ray detector (curved blue surface) passes near the zone center and intersects the boundary of the Brillouin zone centered on the (1, 3,-1) reciprocal lattice point (orange polyhedron)

The vector ***Q*** is the difference between the wavevector of the scattered x-ray ***S*** and the nearest reciprocal lattice vector ***G***. The intensity observed at ***S*** is determined by phonons with wavevector ***Q***. The relationship between ***S***, ***G***, and ***Q*** is shown schematically in Figure 1-1. The blue rods of intensity angled at approximately 45° are the crystal truncation rods arising from a sample with a finite dimension in one-direction. Since x-ray TDS measures the population of thermally populated phonon modes it is particularly sensitive to changes in the frequency of the lowest-lying acoustic modes.

1.2.2 X-Ray thermal diffuse scattering: extension to nanomaterials

My contribution to the field of x-ray scattering has been to extend x-ray TDS from a bulk technique into the regime of nanoscale volumes and to use x-ray TDS to evaluate phonon confinement in semiconducting nanomaterials. This technique allowed the reduction in the required sample volume for phonon characterization using x-ray radiation from 1000s of μm^3 for energy-resolving inelastic probes to as little as 4 μm^3 for TDS. The use of this x-ray technique has extended the probed phonon wavevector in nanomaterials from 0.002 $Å^{-1}$ to 10 $Å^{-1}$. It has also enabled the measurement of phonon modes with wavevectors in the confinement direction. Experimentally, the background and non-sample diffuse scattering has been significantly reduced such that signals as weak as 0.04 a.u./s can be resolved. For comparison, the crystal truncation rod of a 315 nm thick nanomembrane has an intensity of 7 a.u./s at a point approximately 0.25 $2\pi/a$ from the zone center. I have also developed new analytical methods for interpreting the data. The results of these advances in x-ray TDS experiments and analyses are presented as they apply to nanomembrane flatness in Chapter 2 and in their role in evaluating phonon confinement in Chapter 3.

1.2.3 X-Ray reflectivity: summary of methods

X-ray reflectivity (XRR) describes the phenomena associated with the scattering of x-rays at small incident angles from gradients in electron density at interfaces. XRR provides information about the layer thickness, roughness, and electron density of surfaces or buried layers and interfaces. The distribution of the electron density along the direction perpendicular to the interface reflect incident x-rays with a reflected amplitude and phase factor related to the magnitude of the density difference and position at which the reflection occurred. The wavelength of x-rays, in the range 1.0-1.5 Å, offers precise measurement of the interfacial structure with sensitivity to sub-nm levels of interfacial roughness. Additionally, the high fluxes available at synchrotron sources enable time resolved XRR measurements from monolayers of weakly scattering materials.

The interaction of x-rays incident on a surface of a material can be described by a simple model in which the index of refraction of the material characterizes the change in the direction of the incident x-rays when passing from air to the material.[79, 81] The x-rays can be reflected, transmitted, or absorbed. Using a simple model for when an electron in the material is accelerated by the x-ray field, the index of refraction for x-rays in a material, when absorption is neglected, is described as:

$$n = 1 - \delta$$

Equation 1-2

Where δ characterizes the scattering characteristics of the material. The values of δ depend on the on the materials electron density ρ:

$$\delta = \frac{\rho r_0 \lambda^2}{2\pi}$$

Equation 1-3

Where r_0 is the classical radius of the electron and λ is the wavelength of the incident x-ray. Hence, δ is typically on the order of 10^{-6}, making the index of refraction slightly less than unity. The materials critical angle for total external reflection can be approximated by $\theta_c \approx \sqrt{2\delta}$

When x-rays are reflected from an ideally flat surface, the reflected intensity is confined to the plane which includes the incident x-ray beam and the surface normal, with the incident and outgoing directions being symmetric. This is described as specular reflection. In the limiting case of small angles, Snell's law and the Fresnel equations can be used to describe the fraction of the incident intensity either reflected or transmitted. The Fresnel equation for amplitude reflectivity is:

$$r \equiv \frac{a_R}{a_I} = \frac{\theta - \theta'}{\theta + \theta'}$$

Equation 1-4

Where θ and θ' are the angle between the incident x-ray and the surface plane in air and inside the material, respectively. They are related through Snell's law:

$$cos\,\theta = n\,cos\,\theta'$$

Equation 1-5

The reflected intensity is the square of the amplitude reflectivity. For XRR phenomena it is more convenient to use wavevector transfers and their dimensionless counterparts. The wavevector and incident angle are related by:

$$Q = \frac{4\pi}{\lambda} sin\,\theta \; and \; Q' = \frac{4\pi}{\lambda} sin\,\theta'$$

Equation 1-6

The dimensionless counterparts are written as:

$$q = \frac{Q}{Q_c} \; and \; q' = \frac{Q'}{Q_c}$$

Equation 1-7

With these relations, the amplitude reflectivity can be rewritten using wavevector transfer notation as:

$$r(q) = \frac{q - q'}{q + q'}$$

Equation 1-8

The measured reflected intensity *R (q)* is denoted as the intensity reflectivity and defined as *r (q)* multiplied by the complex conjugate of *r (q)*. Substituting with previously defined relations yields *R (Q),* where Q is the experimental x-ray wavevector. In the limiting case where the incident angle is much greater than the critical angle, the intensity reflectivity *R (Q)* falls of proportional to Q^{-4}. This effect coupled with the total external reflection at angles below the critical angle gives rise the reflectivity curve for a perfectly smooth surface, known as Fresnel reflectivity. The ideal reflectivity curve, for a silicon substrate with zero roughness and an x-ray wavelength of 1.54 Å is shown in Figure 2-10. The reflected intensity reaches an approximately constant value below the critical angle of $Q_c = 0.031481$ $Å^{-1}$ for Si and falls off as $(2Q)^{-4}$ at higher angles.

In order to model the reflectivity from non-ideal surfaces and single/multilayer structures, the expression for *R (Q)* needs to be modified. With the assumption that the film is laterally homogeneous, meaning the electron density of the film varies only in the direction perpendicular to the substrate z, the x-ray reflectivity, *R(Q)*, of a rough interface calculated from the electron density profile $\rho(z)$ is:[44, 45]

$$R(Q) = R_f(Q)\left|\frac{1}{\rho(z \to -\infty)}\int \frac{d\rho(z)}{dz} e^{iQz} dz\right|^2$$

Equation 1-9

Here, $R_F(Q)$ is the Fresnel reflectivity of the substrate, Q is the x-ray wavevector, and $\rho(z \to -\infty)$ is defined such that $\rho(z \to -\infty) = \rho_{Substrate}$ and $\rho(z \to +\infty) = \rho_{Air}$ *or* ρ_{Vac}.[79, 82]

The reflectivity $R(Q)$ can be straightforwardly calculated using an analytic form of $\rho(z)$, allowing the prediction of XRR curves for arbitrary structures. The inversion of XRR data to obtain the density profile is more difficult however, in part because it is the square magnitude of the density profile that appears in Equation 1-9.[82] In order to extract insight into the physical and electronic structure of the surface and buried interfaces, a model for $\rho(z)$ must be assumed and model parameters adjusted until a fit to data is achieved. One possible model for $\rho(z)$ is to take the sample as a series of boxes or slabs with a given density, thickness, and interfacial roughness. To model the reflection of x-rays at these sample interfaces the kinematical approximation is used. The kinematical approximate assumes that refraction and multiple reflections make small contributions to the scattered intensity.[79, 82] The interfaces between boxes are assumed to be broadened by error functions. With these assumptions, the expression for $\rho(z)$, becomes:

$$\rho(z) = \rho_{Sub} + \sum_j \frac{\rho_{j+1} - \rho_j}{2}\left[1 + erf\left(\frac{z - z_j}{\sqrt{2}\sigma_j}\right)\right]$$

Equation 1-10

Here, ρ_j is the electron density of the j^{th} box, z_j is the position of the interface between the $j^{th}$and $(j+1)^{th}$ boxes, and σ_j is the RMS (root-mean-square) roughness of the interface between the $j^{th}$and $(j+1)^{th}$ boxes.[82] Then,

$$R(Q) = R_f(Q)\left|\frac{1}{\rho(z \to -\infty)}\int \frac{d\rho(z)}{dz} e^{iQz} dz\right|^2$$

$$= R_f(Q)\left|\frac{1}{\rho_{Sub}}\sum_j \left(\rho_{j+1} - \rho_j\right) \times e^{-\frac{Q^2{\sigma_j}^2}{2}} \times e^{iQz_j}\right|^2$$

Equation 1-11

The fitting of experimental data was carried out using the GenX software package. GenX is based on a differential evolution algorithm for fitting x-ray and neutron reflectivity data.[83] GenX uses the Parratt formalism which considers multiple reflections between interfaces and uses fitting algorithms to minimize a figure of merit.[83] For the samples used in this thesis, the difference between the kinematic and Parratt formalisms lead to negligible differences in the reflectivity curves and extracted parameters. For this work the figure of merit chosen is Log(R1), with R1 defined in ref. 84 and 85. Simple layer models, like those discussed above, are created to model the electron density profile. In the fitting of XRR data, it is important to account for the sample and x-ray beam size. As the incident x-ray angle increases, a larger fraction of the beam footprint is incident on the sample. This effectively varies the magnitude of I_0 as a function of angle at angles where:

$$\frac{Beam\ Width}{\sin\theta} > Sample\ Width.$$

The variation in I_0 with incident angle is accounted for with careful measurement of the x-ray beam width through a knife edge measurement and a measurement of the sample width. These are used as constant parameters during the reflectivity fitting process.

1.2.4 X-Ray reflectivity: extensions to time-dependent systems

Chapter 4 outlines my research to reduce the length scale and timescale of monolayer structural characterization. XRR has previously been used to study donor-semiconductor monolayers deposited on ~10 nm metal oxide layers deposited by atomic layer deposition.[51] The orientation and molecular density of porphyrin dyes were extracted from changes in the monolayer thickness extracted from small shifts in the reflectivity from the metal oxide layer.[51] My work has been to resolve XRR pattern of solely the molecular monolayer, on the order of a few nm with Å resolution. My approach allows a reduction in the fitting parameters leading to improved accuracy. The experimental accomplishment was achieved through the use of synchrotron x-ray sources, with careful calibration to avoid damaging the molecular monolayer, and the reduction of the background scattering to a relative intensity of 10^{-9}. I have been able to achieve dynamic ranges of 10^8 which allows the fitting of multiple reflectivity fringes from monolayers with thickness of ~ 3 nm. The presence of multiple fringes is crucial to the accuracy of the fitting parameters. This approach has been successful in resolving changes in the height of molecular monolayers on the order of 1 nm.

My work has improved the time resolution of XRR from minutes to seconds, even for complex, laterally inhomogeneous surfaces. XRR scans traditionally take on the order of minutes to hours to acquire, particularly for weakly scattering systems like monolayers. This

limits the inherent time resolution of the measurement. This limitation of XRR was overcome by moving beyond the traditional approach, where the sample is exposed to a set photon dose, then removed from illumination and measured. The expose and then measure approach relies on the stability of the structural states on the timescale of minutes to hours. However in reconfigurable monolayer systems, the timescale of the reverse isomerization reaction is on the order of seconds to minutes. This results in XRR measurements which do not reflect the true changes from the optical exposure and are composed of scattering from a constantly changing structural state. My approach increased the time resolution to the order of seconds through the monitoring of the reflected intensity at a point of maximum contrast to monitor the structure during exposure. The improved time resolution enabled XRR to be used to extract detailed structural models of the dynamic reconfiguration. This step towards increased time resolution has also represented an advance in time-resolved and pump-probe XRR towards eventual surface sensitive measurements with picosecond time resolution. These monolayer reflectivity results are discussed in depth in Chapter 4.

1.2.5 X-Ray reflectivity: extensions to faceted surfaces

Chapter 5 details my research to expand the experimental and analytical techniques needed to measure the reflectivity from faceted surfaces. The x-ray results required a detailed generalized mathematical model of the reflectivity from faceted surfaces. Detailed geometric relationships between the scattered x-ray wavevector and the structural parameters of the facets were developed. This approach accounts for reflection from three different surface orientations simultaneously. The mathematical model uses the position, shape, and orientation of the scattered x-ray intensity distributions to determine the angular distributions of the facets and the symmetry of the surface. Additionally, the experimental subtleties of sample alignment and

analysis were determined, allowing future impact in the field of surface scattering through methods for generalizing its usage in the field. The reflectivity of faceted surfaces is described in Chapter 5.

1.3 References

1. Balandin, A. A., Pokatilov, E. P., & Nika, D.L. Phonon engineering in hetero- and nanostructures. *J. Nanoelectron. Optoelectron.* **2**, 140–170 (2007).

2. Maldovan, M. Phonon wave interference and thermal bandgap materials. *Nat. Mater.* **14**, 667–674 (2015).

3. Chen, G. Phonon heat conduction in nanostructures. *Int. J. Therm. Sci.* **39**, 471–480 (2000).

4. Cahill, D. G. *et al.* Nanoscale thermal transport. *J. Appl. Phys.* **93**, 793 (2003).

5. Cahill, D. G. *et al.* Nanoscale thermal transport. II. 2003-2012. *Appl. Phys. Rev.* **1**, 011305 (2014).

6. Zhou, Y. & Hu, M. Record low thermal conductivity of polycrystalline Si nanowire: Breaking the Casimir limit by severe suppression of propagons. *Nano Lett.* **16**, 6178–6187 (2016).

7. Kwon, S., Wingert, M. C., Zheng, J., Xiang, J. & Chen, R. Thermal transport in Si and Ge nanostructures in the 'confinement' regime. *Nanoscale* **8**, 13155–13167 (2016).

8. Minnich, A. J., Dresselhaus, M. S., Ren, Z. F. & Chen, G. Bulk nanostructured thermoelectric materials: current research and future prospects. *Energy Environ. Sci.* **2**, 466–479 (2009).

9. Shi, L., Jiang, J., Zhang, G. & Li, B. High thermoelectric figure of merit in silicon-germanium superlattice structured nanowires. *Appl. Phys. Lett.* **101**, 233114 (2012).

10. Boukai, A. I. *et al.* Silicon nanowires as efficient thermoelectric materials. *Nature* **451**, 168 (2008).

11. Tripathi, M. N. & Bhandari, C. M. Thermal and thermoelectric behavior of silicon-germanium quantum well structures. *Eur. Phys. J. B -- Condens. Matter* **59**, 503–508 (2007).

12. Balandin, A. Thermoelectric applications of low-dimensional structures with acoustically mismatched boundaries. *Phys. Low-Dimens. Struct.* **5–6**, 73–90 (2000).

13. Balandin, A. Thermal properties of semiconductor low-dimensional structures. *Phys. Low-Dimens. Struct.* **1–2**, 1–28 (2000).

14. Hicks, L. D., Harman, T. C., Sun, X. & Dresselhaus, M. S. Experimental study of the effect of quantum-well structures on the thermoelectric figure of merit. *Phys. Rev. B* **53**, R10493–R10496 (1996).

15. Maldovan, M. Sound and heat revolutions in phononics. *Nature* **503**, 209–217 (2013).

16. Maldovan, M. Narrow Low-frequency spectrum and heat management by thermocrystals. *Phys. Rev. Lett.* **110**, 025902 (2013).

17. Balandin, A. A. & Nika, D. L. Phononics in low-dimensions: Engineering phonons in nanostructures and graphene. *arXiv:1211.4482* (2012).

18. Graczykowski, B. *et al.* Phonon dispersion in hypersonic two-dimensional phononic crystal membranes. *Phys. Rev. B* **91**, 075414 (2015).

19. Zen, N., Puurtinen, T. A., Isotalo, T. J., Chaudhuri, S. & Maasilta, I. J. Engineering thermal conductance using a two-dimensional phononic crystal. *Nat. Commun.* **5**, 1-9, (2014).

20. Alizadeh, A., Rostami, A., Baghban, H. & Bahar, H. B. Tailoring electron–phonon interaction in nanostructures. *Photonics Nanostructures - Fundam. Appl.* **12**, 164–172 (2014).

21. Bannov, N., Aristov, V., Mitin, V. & Stroscio, M. A. Electron relaxation times due to the deformation-potential interaction of electrons with confined acoustic phonons in a free-standing quantum well. *Phys. Rev. B* **51**, 9930–9942 (1995).

22. Kamineni, V. K. & Diebold, A. C. Electron-phonon interaction effects on the direct gap transitions of nanoscale Si films. *Appl. Phys. Lett.* **99**, 151903 (2011).

23. Popovic, Z. V., Dohcevic-Mitrovic, Z., Scepanovic, M., Grujic-Brojcin, M. & Askrabic, S. Raman scattering on nanomaterials and nanostructures. *Ann. Phys.* **523**, 62–74 (2011).

24. Donetti, L., Gámiz, F., Roldán, J. B. & Godoy, A. Acoustic phonon confinement in silicon nanolayers: Effect on electron mobility. *J. Appl. Phys.* **100**, 013701 (2006).

25. Donetti, L., Gamiz, F., Rodriguez, N., Jimenez, F. & Sampedro, C. Influence of acoustic phonon confinement on electron mobility in ultrathin silicon on insulator layers. *Appl. Phys. Lett.* **88**, 122108 (2006).

26. Bannov, N., Mitin, V. & Stroscio, M. Confined acoustic phonons in a free-standing quantum well and their interaction with electrons. *Phys. Status Solidi B* **183**, 131–142 (1994).

27. Lamb, H. On Waves in an elastic plate. *Proc. R. Soc. Lond. Ser. A* **93**, 114–128 (1917).

28. Sadeghian, H., Goosen, J. F. L., Bossche, A., Thijsse, B. J. & van Keulen, F. Effects of size and surface on the elasticity of silicon nanoplates: Molecular dynamics and semi-continuum approaches. *Thin Solid Films* **520**, 391–399 (2011).

29. Cuffe, J. *et al.* Phonons in slow motion: Dispersion relations in ultrathin Si membranes. *Nano Lett.* **12**, 3569–3573 (2012).

30. Murphy-Armando, F., Fagas, G. & Greer, J. C. Deformation potentials and electron−phonon coupling in silicon nanowires. *Nano Lett.* **10**, 869–873 (2010).

31. Pop, E., Dutton, R. W. & Goodson, K. E. Analytic band Monte Carlo model for electron transport in Si including acoustic and optical phonon dispersion. *J. Appl. Phys.* **96**, 4998–5005 (2004).

32. Nilsson, G. & Nelin, G. Study of the homology between silicon and germanium by thermal-neutron spectrometry. *Phys. Rev. B* **6**, 3777–3786 (1972).

33. Torres, C. M. S. *et al.* Observations of confined acoustic phonons in silicon membranes. *Phys. Status Solidi C* **1**, 2609–2612 (2004).

34. Chavez, E. *et al.* Flexural mode dispersion in ultra-thin Ge membranes. *14th International Conference on Ultimate Integration on Silicon (ULIS)* 185–188 (2013).

35. Cuffe, J. *et al.* Reconstructing phonon mean-free-path contributions to thermal conductivity using nanoscale membranes. *Phys. Rev. B* **91**, 245423 (2015).

36. Cuffe, J. *et al.* Lifetimes of Confined Acoustic Phonons in Ultrathin Silicon Membranes. *Phys. Rev. Lett.* **110**, 095503 (2013).

37. Groenen, J. *et al.* Inelastic light scattering by longitudinal acoustic phonons in thin silicon layers: From membranes to silicon-on-insulator structures. *Phys. Rev. B* **77**, 045420 (2008).

38. Gopalakrishnan, G. *et al.* Thermal diffuse scattering as a probe of large-wave-vector phonons in silicon nanostructures. *Phys. Rev. Lett.* **110**, 205503 (2013).

39. Gopalakrishnan, G., Holt, M. V., McElhinny, K. M., Czaplewski, D. A. & Evans, P. G. Probing large wavevector phonons at the nanoscale via x-ray thermal diffuse scattering. *Adv. X-Ray Anal.* **56**, 82 (2013).

40. Gopalakrishnan, G. *et al.* Edge-induced flattening in the fabrication of ultrathin freestanding crystalline silicon sheets. *Appl. Phys. Lett.* **102**, 033113 (2013).

41. McElhinny, K. M. *et al.* Fabrication of flat SiGe heterostructure nanomembrane windows via strain-relief patterning. *J. Phys. Appl. Phys.* **48**, 015306 (2015).

42. McElhinny, K. M. *et al.* Synchrotron x-ray thermal diffuse scattering probes for phonons in Si/SiGe/Si trilayer nanomembranes. *MRS Adv.*, 1–6 (2016).

43. Paoprasert, P. *et al.* Bridge-dependent interfacial electron transfer from rhenium−bipyridine complexes to TiO_2 nanocrystalline thin films. *J. Phys. Chem. C* **114**, 9898–9907 (2010).

44. Xiong, W. *et al.* Transient 2D IR spectroscopy of charge injection in dye-sensitized nanocrystalline thin films. *J. Am. Chem. Soc.* **131**, 18040–18041 (2009).

45. Asbury, J. B., Hao, E., Wang, Y. & Lian, T. Bridge length-dependent ultrafast electron transfer from Re polypyridyl complexes to nanocrystalline TiO_2 thin films studied by femtosecond infrared spectroscopy. *J. Phys. Chem. B* **104**, 11957–11964 (2000).

46. Asbury, J. B., Hao, E., Wang, Y., Ghosh, H. N. & Lian, T. Ultrafast electron transfer dynamics from molecular adsorbates to semiconductor nanocrystalline thin films. *J. Phys. Chem. B* **105**, 4545–4557 (2001).

47. Christianson, J. R. & Schmidt, J. R. Structural heterogeneity and dynamics of dyes on TiO_2: implications for charge transfer across organic–inorganic interfaces. *Phys. Chem. Chem. Phys.* **17**, 3731–3740 (2015).

48. Zhang, L. & Cole, J. M. Anchoring groups for dye-sensitized solar cells. *ACS Appl. Mater. Interfaces* **7**, 3427–3455 (2015).

49. Joo, Y. *et al.* Structured Layer of Rhenium Dye on SiO_2 and TiO_2 Surfaces by Langmuir–Blodgett Technique. *Langmuir* **30**, 6104–6113 (2014).

50. Laaser, J. E. *et al.* Dye self-association identified by intermolecular couplings between vibrational modes as revealed by infrared spectroscopy, and implications for electron injection. *J. Phys. Chem. C* **118**, 5854–5861 (2014).

51. Griffith, M. J. *et al.* Determining the orientation and molecular packing of organic dyes on a TiO_2 surface using x-ray reflectometry. *Langmuir* **27**, 12944–12950 (2011).

52. Anderson, N. A. & Lian, T. Ultrafast electron transfer at the molecule-semiconductor nanoparticle interface. *Annu. Rev. Phys. Chem.* **56**, 491–519 (2005).

53. Grätzel, M. Dye-sensitized solar cells. *J. Photochem. Photobiol. C Photochem. Rev.* **4**, 145–153 (2003).

54. O'Regan, B. & Grätzel, M. A low-cost, high-efficiency solar cell based on dye-sensitized colloidal TiO_2 films. *Nature* **353**, 737–740 (1991).

55. Hagfeldt, A., Boschloo, G., Sun, L., Kloo, L. & Pettersson, H. Dye-sensitized solar cells. *Chem. Rev.* **110**, 6595–6663 (2010).

56. Anfuso, C. L. *et al.* Covalent Attachment of a Rhenium bipyridyl CO_2 reduction catalyst to rutile TiO_2. *J. Am. Chem. Soc.* **133**, 6922–6925 (2011).

57. Ashford, D. L. *et al.* Photoinduced electron transfer in a chromophore–catalyst assembly anchored to TiO_2. *J. Am. Chem. Soc.* **134**, 19189–19198 (2012).

58. Albert, K. J. *et al.* Cross-reactive chemical sensor arrays. *Chem. Rev.* **100**, 2595–2626 (2000).

59. Heller, A. Electrical connection of enzyme redox centers to electrodes. *J. Phys. Chem.* **96**, 3579–3587 (1992).

60. Zheng, Y. B. *et al.* Photoresponsive molecules in well-defined nanoscale environments. *Adv. Mater.* **25**, 302–312 (2013).

61. Valley, D. T., Onstott, M., Malyk, S. & Benderskii, A. V. Steric hindrance of photoswitching in self-assembled monolayers of azobenzene and alkane thiols. *Langmuir* **29**, 11623–11631 (2013).

62. Wagner, S. *et al.* Reversible photoisomerization of an azobenzene-functionalized self-assembled monolayer probed by sum-frequency generation vibrational spectroscopy. *Phys. Chem. Chem. Phys.* **11**, 6242–6248 (2009).

63. Krekiehn, N. R. *et al.* UV/Vis spectroscopy studies of the photoisomerization kinetics in self-assembled azobenzene-containing adlayers. *Langmuir* **31**, 8362–8370 (2015).

64. Delorme, N., Bardeau, J.-F., Bulou, A. & Poncin-Epaillard, F. Azobenzene-containing monolayer with photoswitchable wettability. *Langmuir* **21**, 12278–12282 (2005).

65. Wang, S., Song, Y. & Jiang, L. Photoresponsive surfaces with controllable wettability. *J. Photochem. Photobiol. C Photochem. Rev.* **8**, 18–29 (2007).

66. Zong, Y., Rühe, J. & Knoll, W. Novel azobenzene-containing polyamic acids as Langmuir–Blodgett–Kuhn multilayer films and for liquid crystal alignment switching. *Thin Solid Films* **477**, 203–206 (2005).

67. Kolpak, A. M. & Grossman, J. C. Azobenzene-functionalized carbon nanotubes as high-energy density solar thermal fuels. *Nano Lett.* **11**, 3156–3162 (2011).

68. Zhitomirsky, D., Cho, E. & Grossman, J. C. Solid-state solar thermal fuels for heat release applications. *Adv. Energy Mater.* **6**, 1502006 (2016).

69. Luo, W. *et al.* A high energy density azobenzene/graphene hybrid: a nano-templated platform for solar thermal storage. *J. Mater. Chem. A* **3**, 11787–11795 (2015).

70. Feng, W., Luo, W. & Feng, Y. Photo-responsive carbon nanomaterials functionalized by azobenzene moieties: structures, properties and application. *Nanoscale* **4**, 6118–6134 (2012).

71. Castellanos, S., Kapteijn, F. & Gascon, J. Photoswitchable metal organic frameworks: turn on the lights and close the windows. *CrystEngComm* **18**, 4006–4012 (2016).

72. Qin, C. *et al.* A supramolecular assembly of cross-linked azobenzene/polymers for a high-performance light-driven actuator. *J. Mater. Chem. A* **3**, 16453–16460 (2015).

73. Mahimwalla, Z. *et al.* Azobenzene photomechanics: prospects and potential applications. *Polym. Bull.* **69**, 967–1006 (2012).

74. Ferri, V. *et al.* Light-powered electrical switch based on cargo-lifting azobenzene monolayers. *Angew. Chem. Int. Ed.* **47**, 3407–3409 (2008).

75. McElhinny, K. M. *et al.* Optically reconfigurable monolayer of azobenzene donor molecules on oxide surfaces. *Langmuir* **33,** 2157-2168 (2017).

76. McElhinny, K. M., Jacobberger, R. M., Zaug, A. J., Arnold, M. S. & Evans, P. G. Graphene-induced Ge (001) surface faceting. *Surf. Sci.* **647**, 90-95 (2016).

77. Jacobberger, R. M. *et al.* Direct oriented growth of armchair graphene nanoribbons on germanium. *Nat. Commun.* **6**, 8006 (2015).

78. Warren, B. E. *X-Ray Diffraction*. (Dover, 1990).

79. Jens Als-Nielsen & Des McMorrow. *Elements of Modern X-ray Physics*. (John Wiley & Sons, Ltd, 2011).

80. Schwartz, L. H. & Cohen, J. B. *Diffraction from Materials*. (Springer, 1977).

81. Gibaud, A. & Hazra, S. X-ray reflectivity and diffuse scattering. *Curr. Sci.* **78**, 1467–1477 (2000).

82. Uysal, A. *et al.* What x-rays can tell us about the interfacial profile of water near hydrophobic surfaces. *Phys. Rev. B* **88**, 035431 (2013).

83. Björck, M. & Andersson, G. GenX : an extensible x-ray reflectivity refinement program utilizing differential evolution. *J. Appl. Crystallogr.* **40**, 1174–1178 (2007).

84. Wilson, A. J. C. Statistical bias in least-squares refinement. *Acta Crystallogr. Sect. A* **32**, 994–996 (1976).

85. Young, R. A. & Wiles, D. B. Profile shape functions in Rietveld refinements. *J. Appl. Crystallogr.* **15**, 430–438 (1982).

Chapter 2: Fabrication of flat semiconducting nanomembranes

2.1 Introduction

Freestanding nanomembranes provide an ideal system for studying the physics of nanoscale crystalline materials as well as a unique way to create new functionalities. Among inorganic membrane materials, silicon nanomembranes display a range of unusual properties not seen in the bulk, including reduced thermal conductivity and giant persistent photoconduction.[1–3] Silicon nanomembranes are suspended single-crystal sheets of silicon, tens of nanometers thick, with areas in the thousands of square micrometers. Freestanding silicon membranes have applications in novel electronic and photonic materials,[4–7] micromechanical devices,[8–12] x-ray optics,[13–15] macromolecular filters,[16] lithographic templates,[13,15] as sensors,[17,18] and as low-absorption supports in transmission electron microscopy.

Further utility can be incorporated into semiconducting nanomembranes through the creation of alloyed and multilayer structures. Silicon-germanium (SiGe) nanostructures provide the opportunity to control electronic and thermal properties via nanoscale engineering while working within the versatile Si materials platform. With respect to thermoelectric technologies, for example, SiGe quantum wells and superlattices exhibit reduced thermal conductivity,[19–22] which forms the basis for devices with improved thermoelectric figures of merit.[23–25] Extremely thin crystals, in the form of released windows or sheets, combine the functionality and versatility afforded by nanoscale dimensions with the excellent crystal quality and precise control of composition afforded by epitaxial growth.[1,26] SiGe epitaxial heterostructure membranes have

been fabricated in geometries that include completely released and transferred nanosheets,[27] and rolls in which curvature is driven by the lattice mismatch between Si and SiGe.[1, 26]

Challenges in fabrication arise from buckling due to strains of over 10^{-3} in the silicon-on-insulator starting material. In equilibrium, the distortion is distributed across the entire membrane, minimizing the elastic energy with a large radius of curvature. Membranes that are flat, exhibiting a minimal curvature of the lattice planes, can be used in studies of phonon confinement via diffuse x-ray scattering and in other experiments that require crystallographically uniform volumes.[28, 29] In such measurements, flat crystalline nanomembranes with large lateral extents are needed in order to resolve weak scattering signals.

Fabrication of such membranes has been successful in metallic systems,[30,31] but has proven challenging in semiconductors like silicon. In particular, ultra-thin freestanding membranes with nanometer-scale flatness, however, have not been realized. Instead, a buckling pattern is commonly observed.[1, 10,11,32,33] The buckling instability limits the application of fundamental studies and application development, which would benefit from flat crystalline structures with low lateral inhomogeneity. The mechanical problem is further complicated in the creation of very flat Si/SiGe membrane windows. In these multilayer and alloyed materials the mechanical distortion arises from a combination of the Si/SiGe epitaxial mismatch and residual stress arising from membrane fabrication.

Flat nanomembranes are created using an elastically metastable configuration driven by the silicon-water surface energy. Using this edge-induced flattening technique, membranes as thin as 6 nm are fabricated with vertical deviations below 10 nm in a central 100 μm × 100 μm area. In more complex Si/SiGe/Si trilayer membranes, large areas in which the curvature and curvature-induced strain are reduced by an order of magnitude can be produced by patterning the

windows to concentrate buckling in narrow arms with low flexural rigidity supporting a flat central region. The suitability of the membranes for fundamental studies is demonstrated by x-ray studies in which the static diffuse scattering from the flattened membrane structures is reduced in comparison to buckled structures.

2.2 Buckling in semiconductor nanomembranes

Portions of this section were adapted with permission from Gopalakrishnan et. al., Applied Physics Letters, **3, 033113 (2013). Copyright (2013) by American Institute of Physics.*

The compressive strain responsible for buckling results from distortion introduced during the manufacture of the SOI structure and during subsequent processing. Until it is released, the SOI device layer is constrained by the BOX layer, making elastic relaxation of the strain impossible. In a released unsupported structure in which only the edges of the membrane are fixed, the minimum elastic energy of the initially strained silicon layer is achieved when the compressive strain is relieved through buckling across the entire membrane.[34] Forming a flat area within the membrane requires that the elastic energy be concentrated into narrow regions away from the flat area. The process of fabricating a flat membrane must reach the relatively high-energy flat state by a series of steps in which the total energy of the system is successively lowered, but in which the transformation to the uniformly buckled state remains unfavorable.

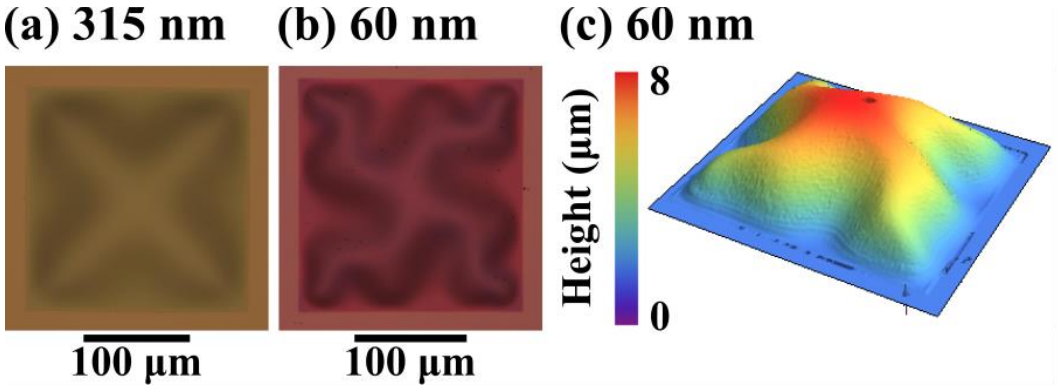

Figure 2-1: Optical micrographs of buckled Si membranes with thicknesses of (a) 315 nm and (b) 60 nm. (c) Height map of the 60 nm membrane obtained by white light interferometry.

Buckling patterns for membranes fabricated using a conventional release process are shown in Figure 2-1 (a) and (b), for membranes with thicknesses of 315 nm and 60 nm, respectively. A map of the vertical displacement of the surface of the 60 nm-thick buckled membrane is shown in Figure 2-1 (c). The maximum vertical distortion is 7.8 μm, corresponding to a curvature of 1.5×10^{-3} μm^{-1}. The magnitude of the initial compressive strain in the device layer can be estimated by measuring the increase in the length of a line across the membrane due to elastic relaxation. For the 60 nm membrane shown in Figure 2-1, the excess length along a line passing through the midpoint of the buckled membrane is 0.74 μm, which corresponds to a compressive strain of 0.37% before release. This number is comparable to an estimate for the primary buckling amplitude, *A*, based on a classical elastic continuum calculation, namely $A \approx 0.5L\varepsilon^{1/2}$, where L is the edge length and ε is the device layer strain.[35] Effects consistent with the development of large compressive strains during thinning have also been observed in scanning probe microscopy studies of the roughening of SOI surfaces at high temperatures.[36]

2.3 Edge-induced flattening of silicon nanomembranes

Portions of this section were adapted with permission from Gopalakrishnan et. al., Applied Physics Letters, **3, 033113 (2013). Copyright (2013) by American Institute of Physics.*

Flat Si nanomembranes can be created by using a fabrication process that limits the buckling to a region near the edges of the window supporting the membrane. The membranes are placed under sufficient tension to overcome the buckling instability resulting from fabrication-induced residual strains. By introducing the edge-induced tension, membranes can be produced with thicknesses as small as 6 nm that exhibit less than 10 nm of vertical distortion over lateral dimensions of 100 μm or more. The process begins with a silicon-on-insulator (SOI) substrate and uses an anisotropic wet etching procedure starting from a photolithographic pattern

on the back of the handle wafer, similar to previous reports.[12, 13,17,18,37] Edge-supported membranes are released by removing the buried oxide (BOX) layer from beneath a region of the device layer. Si membranes with a large range of thicknesses from tens of μm[14,37] to tens of nm have been fabricated using this approach.[10, 12, 13, 15–18, 33, 38, 39] Buckling often occurs in these structures as a result of compressive stresses in the silicon device layer. Previous attempts to create flat semiconductor membranes have used either strain relief structures[10,11,28] or the deposition of a tensile-stressor overlayer.[15, 17]

Figure 2-2 (a) shows the modified membrane fabrication process creating Si-Si interfaces at the edges of the window, and thus allowing a metastable flat state to be reached. Silicon nanomembranes with thicknesses ranging from 315 nm to 6 nm were fabricated beginning with [100]-oriented SOI wafers consisting of a device layer, a BOX layer with a thickness of less than

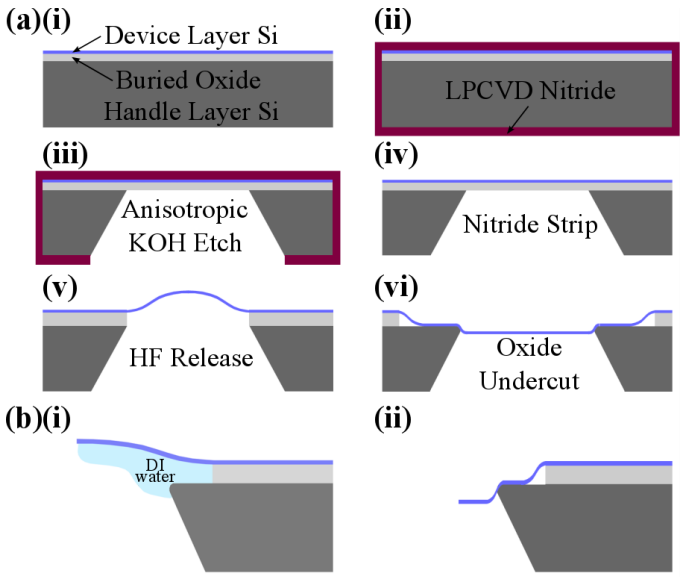

Figure 2-2: (a) Fabrication of Si membranes: (i) Starting SOI structure. (ii) Protection of the device layer by SiN. (iii) Formation of windows via anisotropic etching in KOH. (iv) Removal of the SiN. (v) Release of the membrane from the buried oxide layer of SOI. (vi) Undercutting the buried oxide below the edges of the windows. (b) Flattening process during the drying of the membrane: (i) Buckled membrane at the beginning of the drying process. The trailing edge of the water film progresses outwards (to the right) from the center of the membrane as the water evaporates. (ii) Membrane profile after drying, with sharply bent regions along the inner and outer edges of the Si handle wafer surface exposed by the undercut.

1 μm, and a 625 μm-thick Si (100) handle wafer. The device layer was thinned by wet thermal oxidation followed by etching in hydrofluoric acid (HF). A 200-nm-thick layer of non-stoichiometric low-stress silicon nitride (SiN) was deposited over all surfaces of the sample using low-pressure chemical vapor deposition (LPCVD) at a temperature of 850 °C. The SiN layer provides a patternable mask for the subsequent etch from the back side of the wafer and also protects the device layer during further processing. Windows were patterned on the back of the SOI wafer using photolithography, and the SiN inside the patterned windows was removed by a reactive ion etch (RIE) in CF_4 + 10% O_2 at 60 mTorr. A selective anisotropic etch in KOH was performed in steps, first at 94 °C, then at 84 °C, removing the handle layer silicon from within the exposed regions. The BOX layer acted as an etch-stop for the KOH step, resulting in the formation of SiN/Si/SiO_2 windows with lateral dimensions of 200 μm. The SiN layer was then removed using H_3PO_4 at 160 °C.

The final step in the fabrication process is the removal of the BOX layer beneath the membrane using a 49% HF solution. This step releases membranes with thickness equal to the previously thinned SOI device layer. Flat membranes can be produced when the HF release step is conducted in a way that removes not just the BOX below the 200 μm-wide Si membrane, but also in an additional undercut region extending approximately 30 μm past the edges. The resulting configuration of the device layer, BOX, and handle wafer is shown in Figure 2-2 (a)(vi). After etching in HF to release the membrane and create the undercut region, the sample was cleaned in water. The risk of rupturing the membrane with forces resulting from surface tension was minimized by passing the sample through the surface of the water at an oblique angle during immersion and extraction. The undercutting and subsequent rinsing are especially valuable because these steps can be performed after the standard procedure for fabricating

buckled membranes. It is therefore possible to apply this technique to flatten buckled nanomembranes.

This procedure generates reproducible results for membranes fabricated at two different facilities, starting from different parent SOI wafers. While a small fraction of membranes fail to flatten at the first de-wetting step following the undercut etch, a greater limitation on the yield is imposed by membrane rupture when passing the sample across a liquid surface. This failure mode reduces yield to approximately 50% in membranes thinner than 50 nm, but close to 100% for membranes thicker than 100 nm.

Optical microscopy observations immediately following removal of the membrane from water show that the flattening of the released membrane occurs while the film of water on the backside of the membrane dries. The drying proceeds outwards from the center of the membrane window, as shown in schematically Figure 2-2 (b)(i). The creation of a flat area is favored due to the relative energies of the water-Si, air-Si, and Si-Si interfaces. The surface energy at the water-Si interface is the greatest, with a magnitude of 10^{-13} J/μm^2,[40] and its contribution is particularly large because the water-Si interface covers an area of over 10^3 μm^2 along the edges of the membrane. The receding liquid film maximizes the area of the water-Si interface and stretches the central dry portion of the membrane. The excess length in the Si membrane is thus redistributed to the wet regions near the edge (Figure 2-2 (b)(ii)). These wet regions are sharply curved to follow the vertical edges of the undercut area. The elastic energy stored in curved regions at the edge of the membrane is estimated by treating the membrane edge as a beam of width w and thickness t. The beam is bent with a mean radius of curvature r, which is sensitive to surface conditions. Therefore, values of r measured by optical interferometry are used instead of a calculation from force balance. The strain energy from bending is proportional to $Elwt^3/r^2$,

where E is the elastic modulus in flexure, and l is the length of the beam. For a 30 nm thick membrane and the experimentally observed membrane shape, the total strain energy in the edge regions is 10^{-12} J. Larger radii of curvature are observed with thicker membranes, causing the curvature and thickness dependence to partially offset each other, resulting in a weak dependence of the strain energy on the thickness of the released membranes. The energy cost for concentrating the buckling strain into a narrow region along the membrane edges is therefore approximately two orders of magnitude smaller than the surface energy due to wetting, of 10^{-10} J or more. The flattened state is thus favored over the uniformly buckled configuration while the membrane edges are still in contact with water.

The membrane remains in the metastable flat state after drying because the edges are constrained by the adhesive forces between the bottom of the Si membrane and the exposed surface of the Si handle wafer below the undercut region. The surface energy between the membrane and handle wafer depends on the smoothness of the contact surfaces, and thus can only be estimated. This consideration of the energy is based on a Si-Si interface energy of 10^{-13} J/μm^2.[40] With this value, the energy released by creating the Si-Si interface is 10^{-9} J for a contact region occupying 25 μm out of a total of 30 μm length of the undercut region. The magnitude of the Si-Si interface energy is larger than the strain energy stored in the buckled Si near the edges of the membrane. An undercut of 30 μm of BOX, achieved with a half-hour etch in HF (Figure 2-2 (a)(vi)), provides surface energies large enough to ensure repeatability over a number of samples. This undercut length is observed to increase approximately linearly with etch time, in the range of 20 μm – 40 μm.

Changes to the Si-Si contact energy (e.g. due to interfacial oxidation or from drying of the Si-Si contact) can lower the energy difference between the flat and uniformly buckled state.

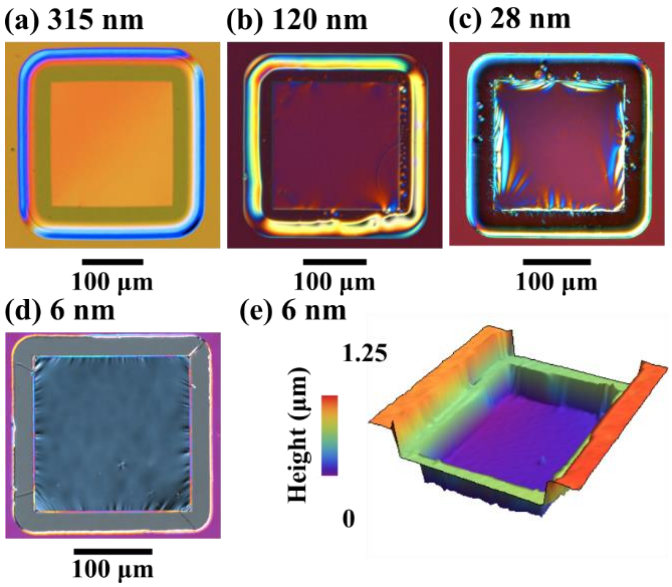

Figure 2-3: (a-d) Optical micrographs of flat membranes fabricated via the undercut etch procedure, with thicknesses as indicated. (e) Height map of the 6 nm-thick membrane surface obtained by white light interferometry.

For example, thicker membranes relax slightly towards a buckled state over the course of one month. Such rebuckling among thin membranes, with thicknesses near 10 nm, has not been observed. The relaxation is faster when membranes are vibrated during handling and measurements. However, membranes that have buckled over time may be re-flattened by repeating the final steps, with an HF dip to remove native oxide, followed by wetting in DI water and drying.

Optical images of membranes formed using the edge-induced flattening process are shown in Figure 2-3 (a) to (d). Optical profilometry of the undercut membranes reveals flat central regions over 100 µm across with height variations smaller than 10 nm. Figure 2-3 (e) shows a height map of the 6 nm membrane acquired using white light interferometry (NewView, Zygo, Inc.), revealing narrow regions along the undercut edges where the buckling is concentrated. Figure 2-4 (a) shows a profile of the membrane height along a line through the center of the 6 nm-thick membrane. The overall reduction in buckling can be quantified using

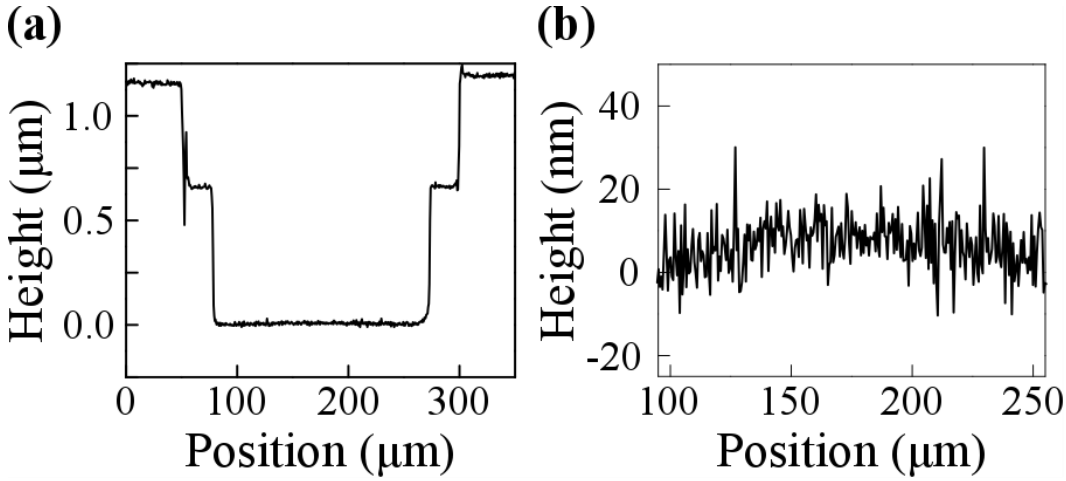

Figure 2-4: (a) Height profile of the 6 nm-thick membrane along a line passing through the center of the membrane area, horizontal with respect to the micrograph in Figure 2-3 (d). (b) Magnified line profile along the center of the suspended membrane, showing the short- and large-scale variations in the membrane height.

the short- and large-scale variations in the height of the membrane within the flat region, as shown in Figure 2-4 (b). The curvature in a central 100 μm region of the membrane is reduced by nearly three orders of magnitude in comparison with the buckled membranes.

The crucial difference between flat and buckled membranes is apparent in x-ray diffuse scattering measurements. Synchrotron x-ray thermal diffuse scattering (TDS) studies were conducted at station 26-ID of the Advanced Photon Source (Argonne National Laboratory) using 10 keV photons focused to a spot size of 30 μm on the sample. Figure 2-5 (a) shows the scattering pattern acquired using a flat 44 nm-thick membrane, in which the Si truncation rod from the (-3 -1 1) reflection, as well as the TDS arising from the thermal population of phonons are visible. The details of the acquisition of the diffuse scattering patterns and the analysis of the TDS are described in Chapter 3. In comparison, Figure 2-5 (b) shows the diffuse scattering acquired with a buckled 60 nm membrane. The dominant contribution to the distribution of the intensity of x-rays scattered from the buckled membrane arises from the strain gradient and

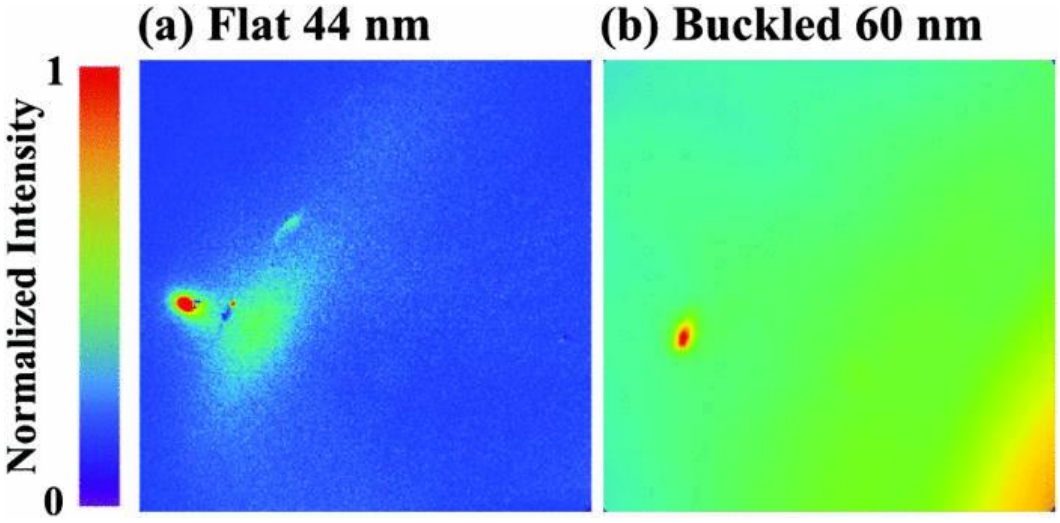

Figure 2-5: X-ray diffuse scattering patterns acquired from (a) a flat 44 nm-thick membrane, and (b) a 60 nm-thick buckled membrane. The TDS signal observed with the flat membrane in (a) is small in comparison with the total intensity in (b) due to the buckling.

crystalline misorientations due to buckling. The TDS signal from the buckled membrane is far smaller than these static contributions to the intensity.

2.4 Strain-relief patterning in Si/SiGe/Si trilayer membranes

Portions of this section were adapted with permission from McElhinny et. al., Journal of Physics D: Applied Physics, **48, 015306 (2015). Copyright (2015) by IOP Publishing LTD.*

Insight into the processes through which flattened SiGe membranes can be fabricated is possible through careful consideration of the strategies used to create flat large-area Si nanomembranes. Si membrane windows are compositionally identical to the surrounding materials, but can be distorted after release because residual stress is imparted into the Si nanomembranes during the thinning or release processes.[1,10,11,26,33,41,42] The magnitude of the residual stress is sufficient to lead to lateral expansion of on the order of 0.1% when the Si membranes are released.[43] The edge-induced flattening methods applicable to Si membranes are ineffective in creating flat Si/SiGe/Si trilayer membranes because (i) the thicknesses of the silicon layers of the membrane are not perfectly matched during epitaxy, which can lead to a preferred direction of curvature in the released membrane, and (ii) the lattice constant reached by

force equilibrium between the Si and SiGe layers is significantly larger than that of unstrained Si. The large strain in the Si/SiGe system requires a flattening strategy based on a structure that can accommodate a larger maximum in-plane expansion than is available through edge-induced flattening. One possibility for overcoming these limitations is through the fabrication of engineered support structures which have previously been used to flatten single layer membranes with micron-scale thicknesses and lateral extents of tens to hundreds of μm.[10, 11, 42]

In an unconstrained Si/SiGe/Si heteroepitaxial membrane the mismatch in lattice constant between SiGe and Si would produce biaxial compression of the SiGe layer and biaxial expansion in the Si layers.[44] Epitaxial growth of a Si/SiGe/Si trilayer on a rigid Si substrate, however, results in the compression of the SiGe layer with respect to its equilibrium lattice constant before release, which leads to an overall biaxial expansion after release. The fabrication of flat membrane windows from stressed layers is challenging because windows are fixed to the original substrate at their edges, and thus cannot relax by expanding laterally, making the flat configuration of the membrane unstable with respect to buckling out of the plane of the surface.[34, 45]

Buckling occurs due to a minimization of the elastic energy by an out of plane distortion of the initially planar structure. The elastic energy is reduced by buckling when the lateral extent of the window is larger than the critical length of the buckling instability. This critical buckling length can be approximated using $l_c \approx \pi h \sqrt{\frac{1}{3\varepsilon}}$, where ε is the residual compressive strain and h is the thickness of the membrane.[10] The study presented here employs $Si/Si_{0.74}Ge_{0.26}/Si$ trilayer membranes with a total thickness of 60 nm and an average compressive strain of 0.3% before release. The critical buckling length for these structures is less than 2 μm, which would yield

windows that are impractically small for many fundamental studies and applications of released membranes.

The process shown in Figure 2-6 can be used to create structures with sufficient mechanical compliance to yield Si/SiGe/Si trilayer membranes with minimum mechanical distortion. The SOI starting material had a 400 nm-thick buried oxide (BOX) layer (Figure 2-6(a)) and a 100 nm-thick device layer that was subsequently thinned to 20 nm via wet thermal oxidation and hydrofluoric acid (HF) etching. Epitaxial SiGe and top Si layers were grown on the SOI device layer using chemical vapor deposition (CVD) (Figure 2-6 (b)). The fabrication then proceeded as the procedure described for the edge-induced flattening process. A 200 nm-thick non-stoichiometric low-stress silicon nitride (SiN) layer was grown on all surfaces of the sample by low-pressure CVD at 850 ºC to serve as a protective coating and as a patternable

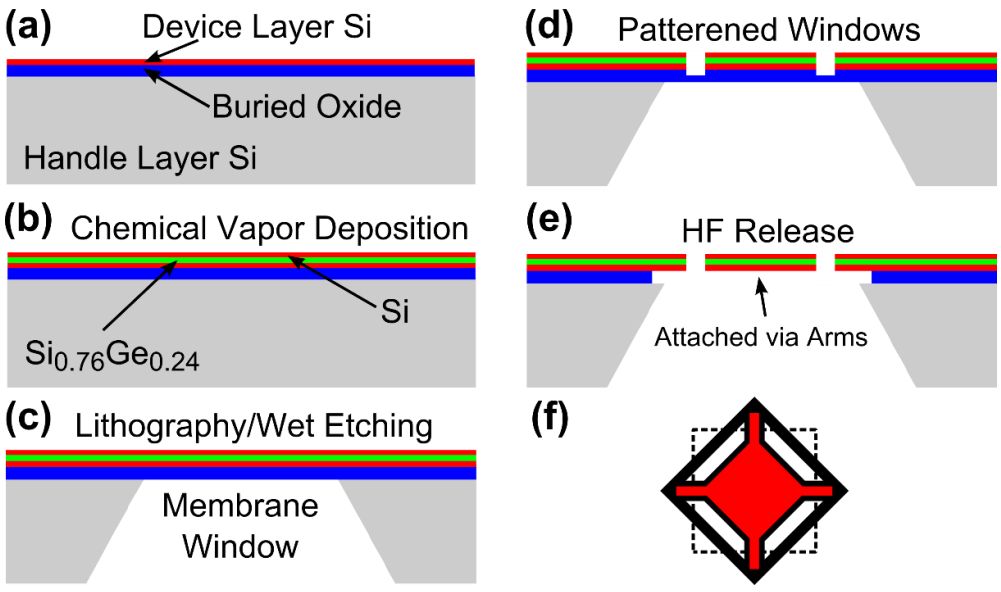

Figure 2-6: Fabrication of Si/SiGe/Si trilayer membranes. (a) Starting SOI. (b) Deposition of the $Si_{0.76}Ge_{0.24}$ and Si layers by CVD. (c) Fabrication of membrane windows via photolithography and anisotropic etching in KOH. (d) Creation of strain-relief pattern by photolithography and reactive ion etching. (e) Release of membrane from BOX layer in hydrofluoric acid (HF). (f) Plan view of the strain-relief pattern. Dashed lines indicate the edges of the membrane window opened in step (c).

etch mask. The back of the handle wafer was patterned by photolithography and reactive ion etching (RIE) of the SiN_x. Windows consisting of BOX, Si/SiGe/Si, and SiN_x were created by removing the handle wafer in the exposed areas using an anisotropic etch in KOH. The SiN_x layer was then removed in phosphoric acid at 170ºC (Figure 2-6 (c)).

To release the constraint imposed by the edges, narrow arms supporting a large central region were patterned into the SiGe membranes before the final removal of the BOX. The arms were created using optical lithography and RIE to remove the trilayer in selected areas, leaving a pattern of 20 μm-wide arms connected to a central 100 μm × 100 μm square area (Figure 2-6 (d)). The trilayer membrane was then released and undercut in concentrated HF, as shown in Figure 2-6 (e). A plan-view schematic diagram of the arm pattern is shown in Figure 2-6 (f). The pattern is oriented so that the edges of the square membrane are at an angle of 45° with respect to the edges of the window in the handle wafer. Four strain relieving arms are aligned along the Si <110> directions, and the edges of the supported central region are parallel to <100>. An alternative arrangement of the supporting arms is based on a large number of narrower strain relieving bars.[10,42] This alternative allows strain to be relieved by in-plane deflection with independent control over the in-plane and out-of-plane stiffness and often includes a buckling of the supporting arms in the plane of the membrane.[10, 42] The single narrow arm structure was selected here, however, in order to eliminate the possibility that instabilities in the etching and drying of the multiple bar structure would complicate their fabrication, including the adhering of several bars together resulting in fracture.

The buckling resulting from the release of a 200 μm × 200 μm edge-supported square Si/SiGe/Si membrane window is apparent in the white-light interferometry height map shown in Figure 2-7 (a). The maximum vertical displacement along a horizontal line through the center of

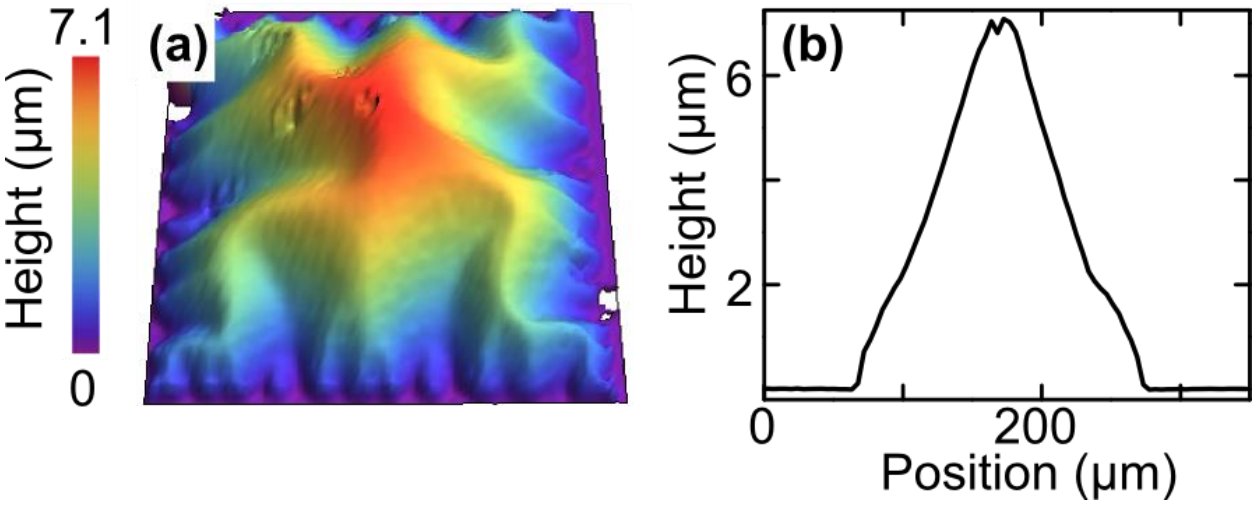

Figure 2-7: (a) White-light interferometry height map of a buckled 60 nm-thick Si/$Si_{0.76}Ge_{0.24}$/Si trilayer window. The lateral extent of the released window is 200 μm. (b) Height profile along a line through the center of membrane, parallel to the bottom edge of the map.

the membrane window is 7.1 μm, as in Figure 2-7 (b). The central region of the unpatterned SiGe membrane has a radius of curvature of 235 μm. With the simplifying approximation that the buckling completely relieves the elastic stress, the excess length of the buckled membrane in Figure 2-7 (b) corresponds to a compressive strain before release of 0.35%. The strain arising from the force balance between the Si and SiGe layers in a linear elastic model for a completely relaxed membrane with the same thickness and composition is 0.29%.[44] The excellent agreement between the experimentally observed magnitude of the released strain and the contribution from the Si/SiGe mismatch indicates that the strain in the Si/SiGe/Si trilayer before release arises from the Si/SiGe lattice mismatch. Residual strain in the device layer of the parent SOI would also lead to buckling, as it does in Si membranes fabricated from SOI.[43] However, it is suspected that in this case the residual stress in the SOI is small compared to stress from the lattice mismatch, and that it has a minimal contribution to the buckling instability in Si/SiGe/Si trilayers.

A map of the vertical displacements in a strain-relieved SiGe membrane is shown in Figure 2-8 (a). Regions of high curvature are confined to 10 μm-wide regions near the both ends of each supporting arm, as shown in the plot of the vertical height as a function of position in Figure 2-8 (b). The curvature where the supporting arms connect to the substrate is five times greater than the curvature where the supporting arms connect to the central region of the membrane. This concentration of the curvature at the substrate end of the arms occurs as a result of the greater rigidity of the substrate compared to the membrane. The radius of curvature across the central region of the membrane supported by narrow arms is 2350 μm. In comparison, the radius of curvature of the same region of the unpatterned membrane is 235 μm. Hence, the introduction of the narrow arms results in an increase of the radius of curvature by a factor of 10, and a corresponding decrease in the curvature-induced strain and strain gradient.

The confinement of the curvature to the arms is consistent with the expectation that the larger flexural rigidity of the central region, arising from its comparatively large area, forces the

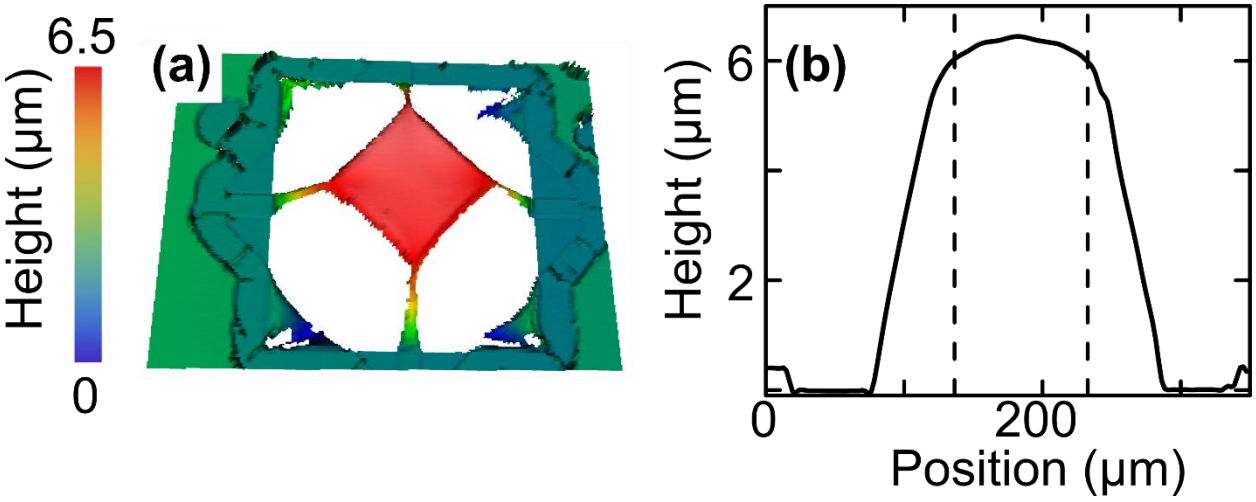

Figure 2-8: (a) White-light interferometry height map of the strain-relief patterned 60 nm-thick trilayer. (b) Height of the patterned trilayer membrane along a line passing horizontally through the center of the membrane and along two of the arms connecting the central region of the membrane to the substrate. Dashed vertical lines indicate the locations of the ends of the supporting arms.

curvature to be concentrated in the arms to reduce the total elastic energy. In the dimension *x* along the length of an arm the elastic strain energy per unit length due to bending is $\frac{1}{2} D \frac{w(x)}{R(x)^2}$.[46] Here $w(x)$ and $R_c(x)$ are the width and radius of curvature, respectively, as a function of the position *x* along the structure. The flexural rigidity per unit width is given by $D = \frac{Eh^3}{12(1-\nu^2)}$, where *E* is Young's modulus and ν is Poisson's ratio. Fabricating structures in which *w*(x) is locally reduced allows the total elastic energy to be minimized by decreasing the radius of curvature in the narrow regions. The further localization of the curvature to the ends of the narrow arms is consistent with the expectation that the arm/membrane geometry closely approximates a clamped-guided beam, which in turn can be approximated as two back-to-back end-loaded beams.[47] In elastic calculations for a geometry corresponding to Figure 2-8, the curvature is concentrated over approximately 1/3 of the length of the arm.[46]

The flatness of membranes supported by narrow arms permits more sophisticated fundamental studies to be performed than would be possible with buckled windows. In order to evaluate the suitability of the flattened membranes for studies of their vibrational properties, synchrotron x-ray TDS measurements were performed at station 26-ID of the Advanced Photon Source at Argonne National Laboratory using an experimental arrangement described in Chapter 3. Incident x-rays with a photon energy of 10 keV were focused to a spot size of 30 μm on the center of the membrane using a capillary condenser x-ray optic. The membrane was oriented in a transmission geometry in which scattered x-rays were collected by a charge-coupled device (CCD) detector, as shown in Figure 2-9 (a). The experiment was performed in vacuum and employed extensive shielding to minimize contributions to the detected intensity caused by scattering from beamline optical components.

Figure 2-9 (b) and (c) shows the TDS signals from a 60 nm-thick Si/$Si_{0.76}Ge_{0.24}$/Si trilayer and a 21 nm-thick Si membrane, respectively. The 60 nm-thick Si/$Si_{0.76}Ge_{0.24}$/Si trilayer was flattened by the strain-relief patterning described here while the 21 nm-thick Si membrane was flattened by edge-induced flattening, which has previously been shown to produce membranes of sufficient flatness for use in TDS studies.[28, 29, 43] The orientations of the membrane surfaces and crystallographic axes with respect to the incident beam and detector are nearly identical for both samples. The truncation rod of the (-3 -1 1) reflection of the membrane lattice produces an intense sharp feature at the right side of the scattering patterns of both samples. The orange line overlaid on the detector image represents the intersection of the Ewald sphere with the zone boundary between the first Brillouin zones of the (-3 -1 1) and (2 2 0) reflections.

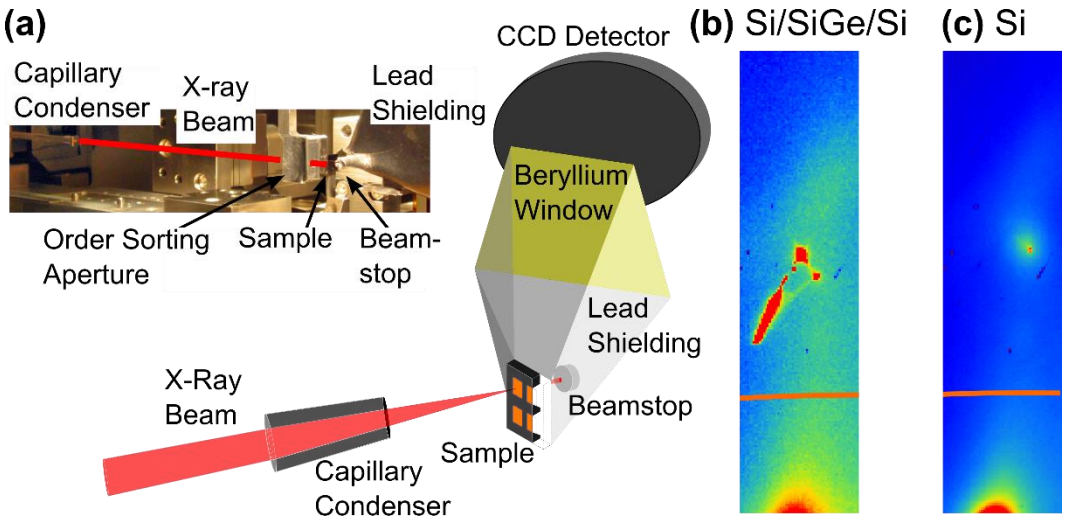

Figure 2-9: (a) Experimental arrangement for x-ray thermal diffuse scattering measurements. The x-ray beam is focused to a 30 μm spot size by a capillary condenser. The focused beam passes through an order-sorting aperture before illuminating the sample in a transmission geometry. The direct beam is stopped by a lead beamstop and the scattered x-rays are collected by a CCD detector. X-ray diffuse scattering patterns acquired from (b) a strain-relief patterned 60 nm-thick trilayer membrane, and (c) a 21 nm-thick flat silicon membrane fabricated using edge-induced flattening. The sharp intense features near the center of the TDS intensity distribution in (b) are an artifact arising from powder x-ray diffraction from material outside the membrane illuminated by a small fraction of the incident beam.

Bright features at the bottoms of the images in Figure 2-9 (b) and (c) are the TDS from near the center of the neighboring zone centered on the (2 2 0) reflection. The diffuse streak of intensity extending upwards through the center of the image towards a second area of higher intensity is TDS resulting from high populations in the lower-frequency phonon modes along the high-symmetry <1 1 1> directions in Si and SiGe. A complete interpretation of the TDS data from Si/SiGe/SI trilayer membranes can be found in Chapter 3. For the moment, it is important to note that the TDS from the Si/SiGe/Si trilayer can be resolved with comparable clarity to the TDS from the silicon nanomembrane, which would not be possible if the Si/SiGe/Si trilayer nanomembrane was buckled as in Figure 2-7 (a). The saturated streak of intensity in the SiGe scattering pattern in Figure 2-9 (b) arises from x-ray diffraction from material outside the membrane illuminated by a small fraction of the incident beam that was not completely suppressed by the shielding of the detector.

2.5 Conclusions

The fabrication strategies described here provide simple approaches for eliminating the buckling distortion of edge-supported semiconductor nanomembranes. The key insight is to create structures and procedures which can overcome the excess elastic strain energy arising from residual stress imparted during SOI fabrication or from the lattice mismatch in heterogeneous materials. This is accomplished through methods which confine the excess length associated with strain to areas away from a central region. The height variation over a 100 μm region of a 6 nm membrane flattened using the edge-induced flattening procedure, for example, is smaller than the height variation over a 25 μm region of a 55 nm-thick membrane fabricated by using a technique aimed instead at minimizing strains in the device layer during fabrication.[22] Techniques like edge-induced flattening, which use differential etching will allow similar

edge-flattening mechanisms to be developed, based on the scheme presented here, to create flat membranes from a number of scientifically and technologically important materials beyond Si in which similar buckling patterns have been observed, including oxides[32] and compound semiconductors. The strain-relief patterning methods offer a non-chemically dependent option for flattening membranes and thus can be generalized to any number of materials systems.

Silicon membranes have found wide and important application as pressure sensors, particularly in cell phones. The sensitivity of these devices can be increased through either reducing the thickness or increasing the surface area. The development of membrane flattening techniques like these, which work in thickness regimes previously dominated by the buckling instability, offer the opportunity to use nm thick membranes in pressure sensing applications. In addition, within the SiGe/Si nanomembrane system flattened structures can find applications in freestanding chemical and gas sensors,[48,49] micro- and nano-electro-mechanical devices,[50–52] thermal waveguides and thermal diodes,[53] and flexible thin film transistors with high-current drive capacity and high electron mobility.[27]

2.6 References

1. Rogers, J. A., Lagally, M. G. & Nuzzo, R. G. Synthesis, assembly and applications of semiconductor nanomembranes. *Nature* **477,** 45–53 (2011).
2. Huang, G. & Mei, Y. Thinning and shaping solid films into functional and integrative nanomembranes. *Adv. Mater.* **24,** 2517–2546 (2012).
3. Cuffe, J. *et al.* Phonons in slow motion: Dispersion relations in ultrathin Si membranes. *Nano Lett.* **12,** 3569–3573 (2012).
4. Roberts, M. M. *et al.* Elastically relaxed free-standing strained-silicon nanomembranes. *Nat. Mater.* **5,** 388–393 (2006).
5. Choi, W. M. *et al.* Biaxially stretchable 'wavy' silicon nanomembranes. *Nano Lett.* **7,** 1655–1663 (2007).
6. Fairchild, B. A. *et al.* Fabrication of ultrathin single-crystal diamond membranes. *Adv. Mater.* **20,** 4793–4798 (2008).
7. Tomljenovic-Hanic, S., Greentree, A. D., de Sterke, C. M. & Prawer, S. Flexible design of ultrahigh-Q microcavities in diamond-based photonic crystal slabs. *Opt. Express* **17,** 6465–6475 (2009).
8. Bercu, B., Xu, X., Montes, L. & Morfouli, P. Characterization of mechanical stress on nanostructures for NEMS applications by ultra-thin membrane and self-suspension techniques. *Microelectron. Eng.* **86,** 1303-1306 (2009).
9. Bercu, B. *et al.* Electron mobility increase in submicronic transistors integrated on ultrathin silicon membranes subjected to high mechanical stress. *Appl. Phys. Lett.* **96,** 092107 (2010).
10. Iwase, E. *et al.* Control of buckling in large micromembranes using engineered support structures. *J. Micromechanics Microengineering* **22,** 065028 (2012).

11. Graff, J. & Schubert, E. Flat free-standing silicon diaphragms using silicon-on-insulator wafers. *Sens. Actuators Phys.* **84,** 276–279 (2000).

12. Juodkazis, S. *et al.* Optical transmission and laser structuring of silicon membranes. *Opt. Express* **17,** 15308-15317 (2009).

13. Utteridge, S. *et al.* Preparation of a 10 nm thick single-crystal silicon membrane self-supporting over a diameter of 1 mm. *Appl. Surf. Sci.* **162–163,** 359–367 (2000).

14. Ahn, M., Heilmann, R. K. & Schattenburg, M. L. Fabrication of ultrahigh aspect ratio freestanding gratings on silicon-on-insulator wafers. *J. Vac. Sci. Technol. B* **25,** 2593–2597 (2007).

15. Constancias, C., Dalzotto, B., Michallon, P., Wallace, J. & Saib, M. Fabrication of large area ultrathin silicon membrane: Application for high efficiency extreme ultraviolet diffraction gratings. *J. Vac. Sci. Technol. B* **28,** 194–197 (2010).

16. Striemer, C. C., Gaborski, T. R., McGrath, J. L. & Fauchet, P. M. Charge- and size-based separation of macromolecules using ultrathin silicon membranes. *Nature* **445,** 749 (2007).

17. Lee, S. H. *et al.* Thin transparent single-crystal silicon membranes made using a silicon-on-nitride wafer. *J. Korean Phys. Soc.* **53,** 579–583 (2008).

18. Dang, Z. Y. *et al.* Fabrication of large-area ultra-thin single crystal silicon membranes. *Appl. Phys. Lett.* **99,** 223105 (2011).

19. Singh, D., Murthy, J. Y. & Fisher, T. S. Effect of phonon dispersion on thermal conduction across Si/Ge interfaces. *J. Heat Transf.* **133,** 122401–122401 (2011).

20. Huxtable, S. T. *et al.* Thermal conductivity of Si/SiGe and SiGe/SiGe superlattices. *Appl. Phys. Lett.* **80,** 1737 (2002).

21. Liu, C.-K. *et al.* Thermal conductivity of Si/SiGe superlattice films. *J. Appl. Phys.* **104,** 114301 (2008).

22. Lee, S.-M., Cahill, D. G. & Venkatasubramanian, R. Thermal conductivity of Si–Ge superlattices. *Appl. Phys. Lett.* **70,** 2957 (1997).

23. Yang, B., Liu, W. L., Liu, J. L., Wang, K. L. & Chen, G. Measurements of anisotropic thermoelectric properties in superlattices. *Appl. Phys. Lett.* **81,** 3588–3590 (2002).

24. Koga, T., Cronin, S. B., Dresselhaus, M. S., Liu, J. L. & Wang, K. L. Experimental proof-of-principle investigation of enhanced Z[sub 3D]T in (001) oriented Si/Ge superlattices. *Appl. Phys. Lett.* **77,** 1490 (2000).

25. Tripathi, M. N. & Bhandari, C. M. Thermal and thermoelectric behavior of silicon-germanium quantum well structures. *Eur. Phys. J. B -- Condens. Matter* **59,** 503–508 (2007).

26. Scott, S. A. & Lagally, M. G. Elastically strain-sharing nanomembranes: flexible and transferable strained silicon and silicon–germanium alloys. *J. Phys. Appl. Phys.* **40,** R75 (2007).

27. Yuan, H.-C. *et al.* Flexible thin-film transistors on biaxial- and uniaxial-strained Si and SiGe membranes. *Semicond. Sci. Technol.* **22,** S72 (2007).

28. Gopalakrishnan, G., Holt, M. V., McElhinny, K. M., Czaplewski, D. A. & Evans, P. G. Probing large wavevector phonons at the nanoscale via x-ray thermal diffuse scattering. *Adv. X-Ray Anal.* **56,** 82 (2013).

29. Gopalakrishnan, G. *et al.* Thermal Diffuse Scattering as a Probe of Large-Wave-Vector Phonons in Silicon Nanostructures. *Phys. Rev. Lett.* **110,** 205503 (2013).

30. Jakšić, Z. & Matovic, J. Functionalization of artificial freestanding composite nanomembranes. *Materials* **3,** 165–200 (2010).

31. Matović, J. & Jakšić, Z. Simple and reliable technology for manufacturing metal-composite nanomembranes with giant aspect ratio. *Microelectron. Eng.* **86,** 906–909 (2009).

32. Lee, K. C. The fabrication of thin, freestanding, single-Crystal, semiconductor membranes. *J. Electrochem. Soc.* **137,** 2556–2574 (1990).

33. Torres, C. M. S. *et al.* Observations of confined acoustic phonons in silicon membranes. *Phys. Status Solidi C* **1,** 2609–2612 (2004).

34. Ziebart, V., Paul, O. & Baltes, H. Strongly buckled square micromachined membranes. *J. Microelectromechanical Syst.* **8,** 423–432 (1999).

35. Stephen P. Timoshenko & James M. Gere. *Theory of elastic stability*. (Dover Publications, 2009).

36. Seo, S., Euaruksakul, C., Savage, D. E., Lagally, M. G. & Evans, P. G. Nanostructure formation in the initial roughening of a thin silicon sheet. *Phys. Rev. B* **81,** 041302 (2010).

37. Iosub, R., Moldovan, C. & Modreanu, M. Silicon membranes fabrication by wet anisotropic etching. *Sens. Actuators Phys.* **99,** 104–111 (2002).

38. Vanhuffelen, W. M., Deboer, M. J. & Klapwijk, T. M. Ultrathin silicon membranes to study supercurrent transport in crystalline semiconductors. Appl. Phys. Lett. 58, 2438–2440 (1991).

39. Groenen, J. *et al.* Inelastic light scattering by longitudinal acoustic phonons in thin silicon layers: From membranes to silicon-on-insulator structures. *Phys. Rev. B* **77,** 045420 (2008).

40. Tong, Q.-Y., Gafiteanu, R. & Gösele, U. Water-enhanced debonding of room-temperature bonded silicon wafers for surface protection applications. *Jpn. J. Appl. Phys.* **31,** 3483–3488 (1992).

41. Lee, K. C. The fabrication of thin, freestanding, single-crystal, semiconductor membranes. *J. Electrochem. Soc.* **137,** 2556–2574 (1990).

42. Hijab, R. S. & Muller, R. S. Residual strain effects on large aspect ratio micro-diaphragms (capacitance transducer). IEEE Micro Electro Mechanical Systems, 1989, Proceedings, An Investigation of Micro Structures, Sensors, Actuators, Machines and Robots 133–138 (1989).

43. Gopalakrishnan, G. *et al.* Edge-induced flattening in the fabrication of ultrathin freestanding crystalline silicon sheets. *Appl. Phys. Lett.* **102,** 033113 (2013).

44. Mooney, P. M., Cohen, G. M., Chu, J. O. & Murray, C. E. Elastic strain relaxation in free-standing SiGe/Si structures. *Appl. Phys. Lett.* **84,** 1093–1095 (2004).

45. Ziebart, V., Paul, O., Munch, U., Schwizer, J. & Baltes, H. Mechanical properties of thin films from the load deflection of long clamped plates. *J. Microelectromechanical Syst.* **7,** 320–328 (1998).

46. Landau, L. D. & Lifshitz, E. M. *Theory of Elasticity*. (Pergamon Press, 1986).

47. Legtenberg, R., Groeneveld, A. W. & Elwenspoek, M. Comb-drive actuators for large displacements. *J. Micromechanics Microengineering* **6,** 320 (1996).

48. Houlet, L. F. *et al.* Fabrication and performance of free-standing hydrogen gas sensors. *Sens. Actuators B Chem.* **129,** 1–9 (2008).

49. Yu, M., Huang, M., Savage, D. E., Lagally, M. G. & Blick, R. H. Local-wetting-induced deformation of rolled-up Si/Si-Ge nanomembranes: A potential route for remote chemical sensing. *IEEE Trans. Nanotechnol.* **10,** 21–25 (2011).

50. Schmidt, O. G., Deneke, C., Manz, Y. M. & Müller, C. Semiconductor tubes, rods and rings of nanometer and micrometer dimension. *Phys. E Low-Dimens. Syst. Nanostructures* **13,** 969–973 (2002).

51. Schmidt, O. G., Deneke, C., Schmarje, N., Muller, C. & Jin-Phillipp, N. Y. Free-standing semiconductor micro- and nano-objects. *Mater. Sci. Eng. C-Biomim. Supramol. Syst.* **19,** 393–396 (2002).

52. Prinz, V. Y., Seleznev, V. A., Prinz, A. V. & Kopylov, A. V. 3D heterostructures and systems for novel MEMS/NEMS. *Sci. Technol. Adv. Mater.* **10,** 034502 (2009).

53. Maldovan, M. Narrow low-frequency spectrum and heat management by thermocrystals. *Phys. Rev. Lett.* **110,** 025902 (2013).

Chapter 3: Probing phonons in spatially-confined semiconducting nanomembranes

3.1 Introduction

Vibrational phenomena play an important role in determining the electric, acoustic, elastic, and infrared properties of solid materials. Solids are ideally described by a crystal structure in which each atomic site is occupied by an immobile atom. In real crystalline materials the atoms are not fixed in a static lattice instead they vibrate as a result of the thermal energy in the system. However, a favorable minimization of the elastic potential energy results in a restoring force which limits the magnitude of the atomic displacements. In silicon, the root-mean-square displacement of a thermally excited atom at room temperature is 0.077 Å, corresponding to 1.4% of the silicon lattice parameter.[1]

Phonons are the fundamental quanta of lattice vibration in solid materials. The states populated by phonons are the elastic normal modes of the crystalline lattice. Each mode is characterized by its wavevector and frequency. Any arbitrary lattice vibration can then be viewed as a superposition of a population of phonons in these normal modes. The relationship between the frequencies of the normal modes populated by phonons as a function of their wavevector is called the phonon dispersion.

The set of normal modes which make up the phonon dispersion are computed from the crystal structure and the elastic constants. The following brief summary is based on a complete discussion in Solid State Physics by Ashcroft and Mermin[2] and Dr. Martin Holt's PhD thesis from the University of Illinois.[3] Classical theory treats the lattice vibrations of crystals in the harmonic approximation where the displacements of the atoms during vibration are small in comparison to the distance between atoms. Under this approximation the potential energy U

about its equilibrium value for a single atom basis can be expressed using a three-dimensional form of Taylor's theorem.

$$U(r_1, r_2, r_3, \dots, r_N) = E(R_1, R_2, R_3, \dots R_N) + \sum_i \left.\frac{\partial U}{\partial r_i}\right|_{R_i} \cdot u_i + \frac{1}{2}\sum_{i,j} \left.\frac{\partial^2 U}{\partial r_i \partial r_j}\right|_{R_i,R_j} \cdot u_i u_j + \cdots$$

Equation 3-1

In Equation 3-1, R_i and R_j are the Bravais lattice vectors of atoms *i* and *j*, r_i and r_j are the instantaneous positions of atoms *i* and *j*, and u_i and u_j are the instantaneous displacements of the atoms from their Bravais lattice vectors such that $u_n = r_n - R_n$.

At equilibrium, the first correction term is zero since there is no net force on any atom in equilibrium. The second correction term is the harmonic correction term and is non zero. Terms beyond the second correction term are anharmonic contributions to the energy. While these terms do play an important role in understanding many physical phenomena, they are treated as small perturbations on the dominant harmonic term. Thus, in the harmonic approximation the potential energy is expressed only a function of the equilibrium potential energy and the harmonic term. For many dynamic problems, like those discussed in this thesis, the equilibrium contribution is a constant and can be ignored.

Within the harmonic term in Equation 3-1, the interatomic force constants are expressed as:

$$D_{\alpha,\beta,i,j} \equiv \left.\frac{\partial^2 U}{\partial r_{\alpha,i} \partial r_{\beta,j}}\right|_{equilibrium}$$

Equation 3-2

which represents the force on ion *i* in the Cartesian direction α resulting from the displacement of atom *j* in direction β. In the harmonic approximation, these force constants dictate the phonon dynamics and are key in the derivation of the phonon dispersion.

In order to derive the phonon dynamics from the interactions of atoms using the harmonic model, all the atoms (*N)* with mass *M*, must obey the *3N* equations of motion:

$$M\ddot{u}_i = D_{i,j}u_j$$

Equation 3-3

Solutions for u_i should have a plane wave solution of the form:

$$u_i(t) = \hat{\varepsilon}e^{i(k\cdot R_i - \omega t)}$$

Equation 3-4

Where $\hat{\varepsilon}$ is the polarization vector, *k* is the wavevector, ω is the vibrational frequency, and *t* is time.

The dynamical matrix D(k) is defined as the Fourier transform of $D_{i,j}$.

$$D(k) = \sum_i D_{i,0} \cdot e^{-ik\cdot(R_i - R_0)}$$

Equation 3-5

Using these two definitions, the following eigenvalue problem can be solved to provide solutions for all harmonic phonon states.

$$D(k) \cdot \hat{\varepsilon} = M\omega^2\hat{\varepsilon}$$

Equation 3-6

By defining the inter-atomic force constants $D_{\alpha,\beta,i,j}$, typically accounting for only the nearest neighbors, calculating the eigenvalues and eigenvectors of Equation 3-6 yields both the

dispersion relation $\omega(k,\lambda)$ and the polarization vector $\hat{\varepsilon}(k,\lambda)$ for a phonon of wavevector k and mode λ.

It is illustrative to look at the resulting phonon dispersion for a 1-D chain of atoms with both a monoatomic and a diatomic basis. For a 1-D chain with N atoms and a lattice constant of a, the periodic boundary condition imposes that:

$$e^{ikNa} = 1$$

Equation 3-7

This requires k to have the form:

$$k = \frac{2\pi}{a}\frac{n}{N}$$

Equation 3-8

Where n is an integer between 0 and N.

For a 1-D chain of atoms, with mass M and in which $D_{i,j}$ is expressed as a simple spring constant K, the phonon dispersion is:

$$\omega(k) = 2\sqrt{\frac{K}{M}\left|\sin\left(\frac{1}{2}ka\right)\right|}$$

Equation 3-9

When the model is expanded to a 1-D chain with a two atom basis, the model leads to two sets of solutions:

$$\omega^2 = \frac{K+G}{M} \pm \frac{1}{M}\sqrt{K^2 + G^2 + 2KG\cos ka}$$

Equation 3-10

where G and K are the spring constants between the atoms with different bond strengths.

These two ω vs. k curves are referred to branches of the phonon dispersion. The lower frequency branch, which has ω=0 at k=0 is the acoustic branch, while the higher frequency branch, which has ω≠0 at k=0 is the optical branch. This same construction can be applied to 3-D lattices.

For a material with a single atom basis, the lattice has three branches of its normal modes: two transverse branches and one longitudinal branch. Atoms in a transverse mode have vibrational displacements that are perpendicular to the direction of the wavevector. In a longitudinal mode vibrational displacements are in the same direction as the wavevector. For a material with a two-atom basis, like silicon, there are a total of six branches: three optical modes and three acoustic modes. The three acoustic modes consist of two branches with transverse polarization and one branch with longitudinal polarization. Similarly there are two transverse optical modes and one longitudinal optical mode. The two transverse branches and one longitudinal branch within a given mode (acoustic or optical) may be degenerate along certain directions depending on the symmetry of the crystal. Acoustic phonon modes have zero frequency at zero wavevector and move the atoms in the primitive unit cell in-phase with each

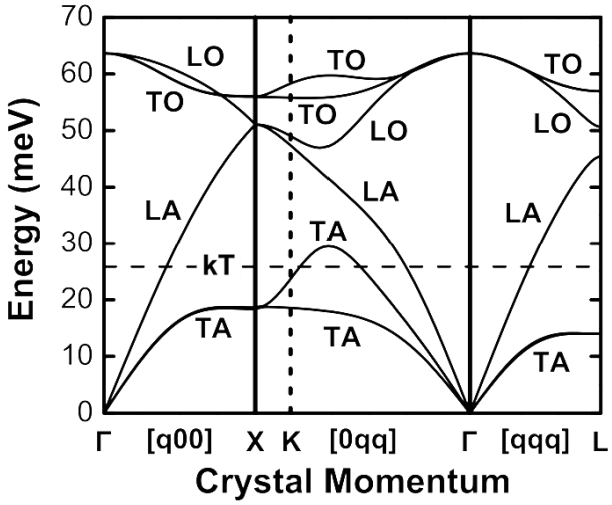

Figure 3-1: Bulk silicon phonon dispersion

other. The bulk phonon dispersion for silicon is shown in Figure 3-1. Acoustic phonons in silicon have energies from 0-50 meV.[4] Optical phonon modes have non-zero frequency at the zero wavevector and move the atoms in the primitive unit cell out-of-phase with each other. Optical phonons in silicon have energies from 50-70 meV.[4] For reference, the thermal energy K_bT at 300 K is 25 meV.

The phonon dispersion, $w_s(q)$, can be measured from experiments in which an external probe exchanges energy and momentum with lattice vibrations. Such probes include neutrons or electromagnetic radiation such as x-rays or visible light. Neutrons and photons probe the phonon dispersion in different ways due to the differing natures of their energy-momentum relationships. This work uses x-ray thermal diffuse scattering (TDS) to probe the phonon dispersion and population in nanoscale materials. A complete discussion of the fundamentals of TDS can be found in Chapter 1.

Recent advances in nanofabrication, theory and computation, and characterization provide a dramatically increased scope for the control of vibrational properties of nanomaterials.[5–7] These advances have inspired the drive to take the management of phonons, which are responsible for the transmission of both sound and heat in semiconducting or insulating solids, to the level of control achieved with electrons and photons.[7] Phonon scattering and dispersion in nanomaterials differ significantly from bulk materials[8–10], and nanostructures with periodicities ranging from centimeters to nanometers can thus manipulate phonons at frequencies relevant to sound, ultrasound, GHz acoustics, and heat transfer.[7,11,12] In bulk materials, vibrational properties have been well resolved for several decades, largely thanks to inelastic spectroscopy techniques in neutron and x-ray scattering.[13,14] Nanomaterials, however, pose a significant and ongoing challenge due to their small volume and, as a result, the

characterization of phonons in nanomaterials has been largely accomplished using optical techniques. Nanostructures formed from Si and Si-alloy semiconductors illustrate the limitations of the optical approach and have widespread thermal, electronic, and optical applications. The momenta of the THz-frequency phonons relevant to thermal transport in Si are far larger than can be probed optically, reaching wavevectors on the order of 1 $Å^{-1}$.[15–20] Large-wavevector acoustic phonons are particularly important in electronic processes in Si because electron-phonon coupling involves phonons with wavevectors connecting widely separated conduction band minima (at $2\pi/a_{Si}$ [0 0 0.85], with lattice parameter a_{Si}=5.43 Å).[21]

The magnitude of the characterization challenge can be made conceptually clear by dividing the Brillouin zone characterizing the momentum space of Si into two volumes: a small-wavevector region near the origin of reciprocal space and a region spanning a far larger volume of reciprocal space characterized by wavevectors with magnitudes near the inverse of the lattice parameter. The small-wavevector regime of the phonon dispersion in nanomaterials, in which wavevectors are on the order of 5×10^{-4} $Å^{-1}$, is strongly modified in comparison with the bulk and has been extensively probed by optical Raman and Brillouin scattering.[22–29] The region probed by optical scattering with visible or UV photons, however, spans just a small fraction, approximately $(5 \times 10^{-4}\ Å^{-1}/1\ Å^{-1})^3 \approx 10^{-12}$, of the relevant volume of reciprocal space. The vast majority of phonon modes in nanomaterials are thus uninvestigated by optical techniques.

The dimensional confinement induced by nanostructuring alters phonon modes and the properties they influence. Reducing the size of the crystal leads to confinement-induced modifications of the dispersion of acoustic phonons.[30–32] Confinement-induced changes are also partially responsible for the significant decrease in the thermal conductivity observed in thin films. Decreased thermal conductivity is of particular importance for thermal management of

both nanoscale electronic devices, where thermal management is a growing problem, and for thermoelectric materials, where the reduced thermal conductivity serves to increase the thermoelectric figure of merit, ZT.[30,31] Other phenomena, related to acoustic phonons are modified in nanoscale crystals, including the phonon group velocity, the pattern of displacements associated with each mode, and the total density of states.[32] The decreased phonon group velocity in nanowires and thin films results in increased acoustic phonon relaxation near point defects (vacancies and impurities), dislocations, and phonon-phonon processes.[32, 33]

An additional degree of freedom in the design of Si-based group-IV nanomaterials is obtained by including SiGe alloys in the structure. First, the increased mass of Ge leads to a reduction in phonon frequencies. Lattice dynamics calculations for an $Si_{1-x}Ge_x$ alloy with x=12.5% predict, for example, that phonon energies are reduced by 0.4 meV at the boundary of the Brillouin zone, in comparison with Si[34]. In addition, the randomness of Ge substitution into the diamond structure leads to mass-disorder scattering and causes SiGe to have different vibrational properties that pure Si or Ge[35].

X-ray TDS can be used to probe large-wavevector phonons in silicon nanomembranes with thicknesses between 315 nm and 6 nm and Si/SiGe/Si trilayer nanomembranes. Obtaining large-wavevector insight into the phonon dispersion and populations is particularly important in understanding thermal conductivity in Si and SiGe. In both of these materials, significant contributions to thermal conductivity arise from phonons with energies above approximately 1 meV, particularly at elevated temperatures relevant to thermoelectric applications.[35] Acoustic phonons with energies in this range are far from the zone center, with wavevectors on the order of 10% or more of the zone boundary momentum, making a large-wavevector probe particularly important.

The work in this thesis investigates the thickness and spatial dependence of the modifications of the phonon populations. An excess in TDS intensity in thinner membranes is observed and attributed to a modification of the phonon dispersion through softening of elastic constants and the development of new quantized phonon modes of vibration not present in bulk systems. Some of these new modes have lower energy than the bulk modes they replace.

The vibrational properties of thin elastic membranes can be described by using elasticity theory in a continuum approximation.[36] The solutions resulting from this description have been used to obtain the atomic displacement and phonon frequencies for phonons in the small wavevector regime in semiconductor nanostructures.[2, 18] In the case of thin sheets, the periodic boundary conditions found in bulk systems are replaced by vanishing normal components at the free surfaces of the sheet. This modification of the boundary condition results in the creation of three modes not found in bulk systems: a shear mode, a flexural or antisymmetric mode, and a dilatational or symmetric mode.[37] The flexural and dilatational modes have mixed transverse and longitudinal character. In the case where the membrane thickness is much larger than the characteristic coherence length of the phonons, these modes become a pair of Rayleigh waves localized on the surfaces of the membrane. These flexural and dilatational modes are particularly interesting as their lowest lying modes have phonon frequencies below the lowest lying mode (TA) mode of bulk silicon. A comparison between the bulk Si phonon dispersion and the dispersion of the lowest-lying flexural and dilatational modes can be seen in Figure 3-2 (a-b). Figure 3-2 (c) shows the relative magnitudes and direction of the atomic displacements of atoms near the surface of a thin semiconductor sheet for the case of the lowest lying dilatational

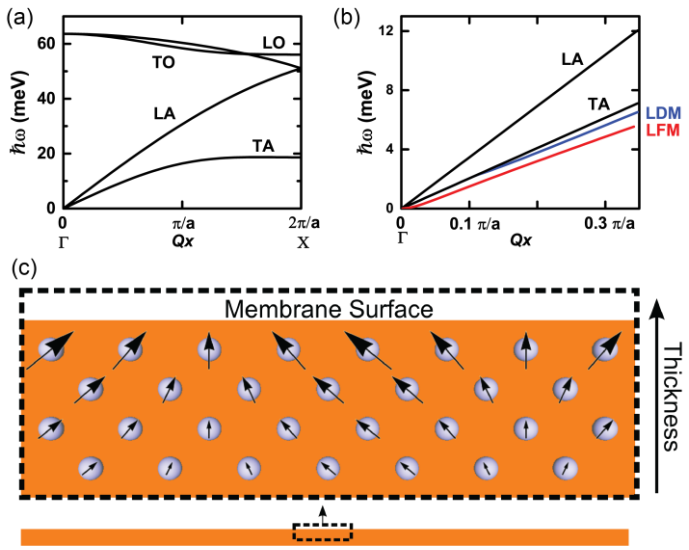

Figure 3-2: (a) Bulk phonon dispersion for Si along the [1 0 0] direction, with transverse acoustic (TA), longitudinal acoustic (LA), transverse optical (TO) and longitudinal optical (LO) branches. (b) Dispersions of the lowest flexural (LFM) and dilatational (LDM) modes of a 10-nm-thick silicon membrane, after Ref. 40, compared with bulk acoustic modes. The energy-wave-vector regime of the comparison is indicated by the red rectangle in the bulk dispersion. (c) Directions and relative magnitudes of near-surface atomic displacements in a Si nanomembrane for an example of the lowest-frequency dilatational mode.

mode. These low-lying modes contribute over 90% of the TDS intensity, making silicon and silicon-germanium nanomembranes an interesting system to study.

3.2 Probing phonons in silicon nanomembranes by TDS

Portions of this section were adapted with permission from Gopalakrishnan et al., Physical Review Letters, **20, 205503, (2013) Copyright (2013) by the American Physical Society and Gopalakrishnan et al., Advances in X-ray Analysis, **56**, 82, (2013). Copyright (2013) by the International Center for Diffraction Data.*

To probe phonons in silicon nanomembranes, x-ray TDS was used. Synchrotron x-ray TDS measurements were carried out at station 26-ID-C of the Advanced Photon Source (APS) at Argonne National Lab. A schematic representation of the experimental setup is shown in Figure 3-3. This experimental setup is the same as the setup shown in Chapter 2 repeated for clarity in the discussion of the TDS measurements. The measurement was performed in a transmission geometry, with the plane occupied by the silicon nanomembrane normal to the incident beam.

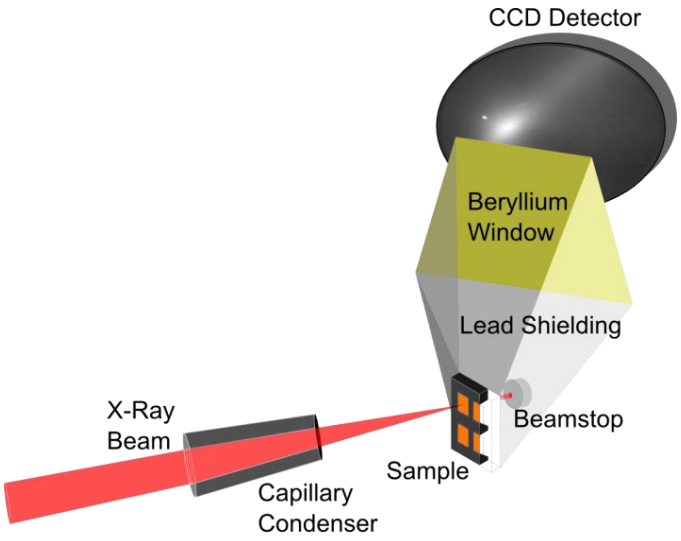

Figure 3-3: Schematic representation of the experimental setup for nanomembrane TDS measurements at 26-ID-C of the Advanced Photon Source (APS). All components except the CCD Detector reside within an evacuated vacuum chamber during the measurement to reduce scattering from air.

The samples were mounted in a vacuum chamber in order to minimize the contribution of air scattering to the scattered intensity. A 10-keV x-ray beam was focused on the membrane with a 30 μm spot size using a capillary condenser. Contributions from unfocused or secondary x-rays were minimized by utilizing a 150 μm order sorting aperture placed along the beam path between the condenser optic and the sample. A lead (Pb) beamstop was positioned downstream of the sample to absorb the portion of the direct beam which passed through the sample. Lead shielding was shaped into a truncated pyramid extending from the beryllium exit window of the evacuated chamber to the sample. The shielding was positioned in the chamber to eliminate the contributions of scattered x-rays which did not originate from the sample, such as scattering from optics and other surfaces inside the chamber. X-rays scattered by the sample were detected using a charge-coupled device (CCD) (Mar Inc.) with a pixel size of 80 μm and a total diameter of 165 mm. The detector subtended a conical angle of approximately 15°. The sample orientation was chosen to avoid exciting Bragg reflections and to capture the TDS signal from wavevectors

ranging from about $0.1(2\pi/a_{Si})$, representing points near the zone center, to $2\pi/a_{Si}$, corresponding to points on the zone edges, where a_{si} is the Si lattice parameter, 5.43 Å.

TDS intensity distributions were collected from a series of membrane samples with thicknesses between 315 nm and 6 nm. Intensity distributions from the surrounding bulk support structure were also acquired for comparison and to aid in determining the sample orientation. Background measurements were performed by mechanically removing the membrane from a window of a sample and passing the incident x-ray beam through the open window. These background images allowed non-sample sources of scattering to be subtracted from the sample data to obtain an accurate measurement of the TDS intensity without contamination from static scattering sources. Exposure time varied, depending on sample thickness. The exposures were double correlated to eliminate zingers, random events from cosmic rays or from the decay of radioactive isotopes with the detector. Sets of two to three scans, with a cumulative exposure time of approximately one hour were required to resolve the weak TDS signature from phonons near the zone boundaries. These scans were averaged and an average of background scans from a mechanically removed window of the same orientation was subtracted to show only the x-rays scattered by the sample.

The scattering signature of the TDS from a 315 nm-thick membrane is shown in Figure 3-4. The isolated, sharp, bright, oval spot on the left of the detector is the intersection of the reciprocal space sheet corresponding to the detector plane with Si crystal truncation rod, which replaces the Bragg peak when diffracting from two-dimensional systems. To the right of the crystal truncation rod is the region of maximum TDS intensity. It corresponds to the point on the

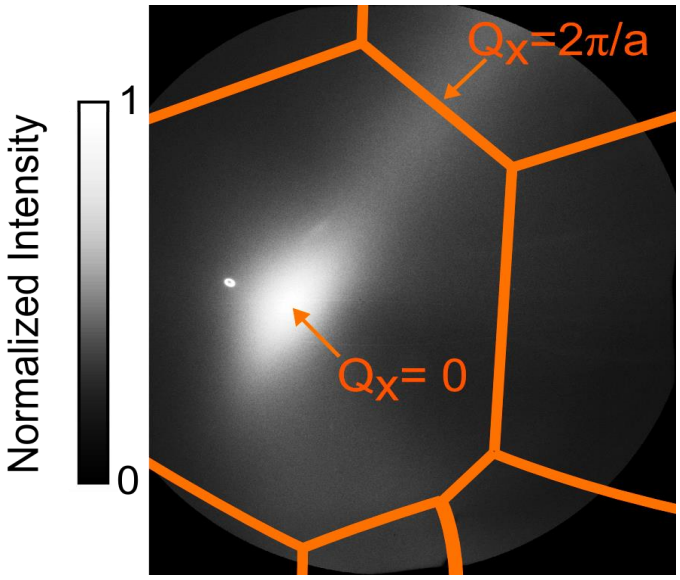

Figure 3-4: TDS intensity distribution from a 315 nm-thick silicon nanomembrane. The intersections of the Brillouin zone edges with section of the Ewald sphere caught by the detector plane are shown as orange lines.

detector which lies closest in reciprocal space to the center of the Brillouin zone. Since TDS is sensitive to the population of thermally populated phonons, and the phonon population is highest near the zone center, the TDS intensity will be greater when the Ewald sphere passes closer to the zone center. The orange lines shown on the image are the intersections of the edges of the Brillouin zone centered on the (-3 -1 1) reciprocal lattice point, with the section of the Ewald sphere caught by the detector plane. Additionally, a diagonal streak of intensity extends from the region of maximum TDS intensity diagonally toward the upper right region of the image. This corresponds to a path which roughly follows the path from the gamma point in the center of the Brillouin zone to the X point on the zone boundary. TDS intensity is expected to be higher along this path due to the elastic anisotropy of Si. The quantity called *Qx* is the projection of the phonon wavevector, Q, onto the x axis, [100], of reciprocal space. Values of *Qy* and *Qz* along the streak vary from 0.18 to 0.35 $2\pi/a_{Si}$ in *Qy* and 0.18 to 0.4 $2\pi/a_{Si}$ in *Qz*.

The TDS intensity distribution expected from using the bulk Si phonon dispersion was computed using a Mathematica notebook. The bulk Si phonon dispersion was computed by utilizing the dynamical matrix for Si, which is Fourier transform of the force constant matrix as discussed in section 3.1.

The region of reciprocal space being probed by the beam is computed using the beam energy and geometric considerations. The sample θ, φ, and ψ are accounted for as well as the location of the detector. The q-value for each pixel is then computed. Due to slight misorientation in sample θ, φ, and ψ during mounting onto a sample stick as well as inaccuracy in the sample adjustment setup, the exact orientation of the sample in the beam is not known. Additionally, in initial experiments, the exact location of the detector was not known. In later experiments, the detector position was fit experimentally by matching the powder diffraction patter of Si from a sample mounted in the same location as the membrane sample. In order to determine the sample orientation and detector locations, simulated detector images, generated by changing the sample θ, φ, and ψ and detector height above the beam and angle from the beam, were compared to experimentally measured bulk and membrane samples.

The x and y pixel locations of the truncation rod and the maximum in TDS intensity were used as indicators of agreement between the simulated image and the experimental image. Changing the detector angle resulted in only a horizontal change in pixel number, corresponding to the x pixel value. Changing the detector height resulted in an only vertical change in pixel number, corresponding to the y pixel value. For determining sample θ, φ, and ψ, three new parameters were used, the distance and the angle between the location of the truncation rod and maximum in TDS intensity, and the angle at which the high streak of intensity which goes from the maximum in the TDS is at. When these three parameters were satisfied, the image could be

translated using the detector location to generate a matching image. The approximate values of sample θ, φ, and ψ are known initially from the experimental setup.

TDS profiles were extracted along a path which passes through the maximum in the TDS intensity and extends along the streak of high intensity. Profiles were extracted using a Mathematica notebook. The profiles were calculated by extracting a rectangle of pixels 51 pixels wide and 2048 pixels long. Columns of 51 pixels were averaged into a single value. The 2048 pixels were then averaged via a boxcar average with a boxcar width of 71 pixels to create the profiles shown later in this chapter.

The experimental setup was tested by collecting x-rays scattered from a bulk region near the membrane sample. The collected pattern was compared to the pattern expected from TDS theory using the bulk Si phonon dispersion. The comparison is shown in Figure 3-5. Figure 3-5 (a) shows the experimentally observed bulk TDS pattern while (b) shows the predicted pattern. Figure 3-5 (c) shows an intensity profile extracted along the paths indicated in (a) and (b), which

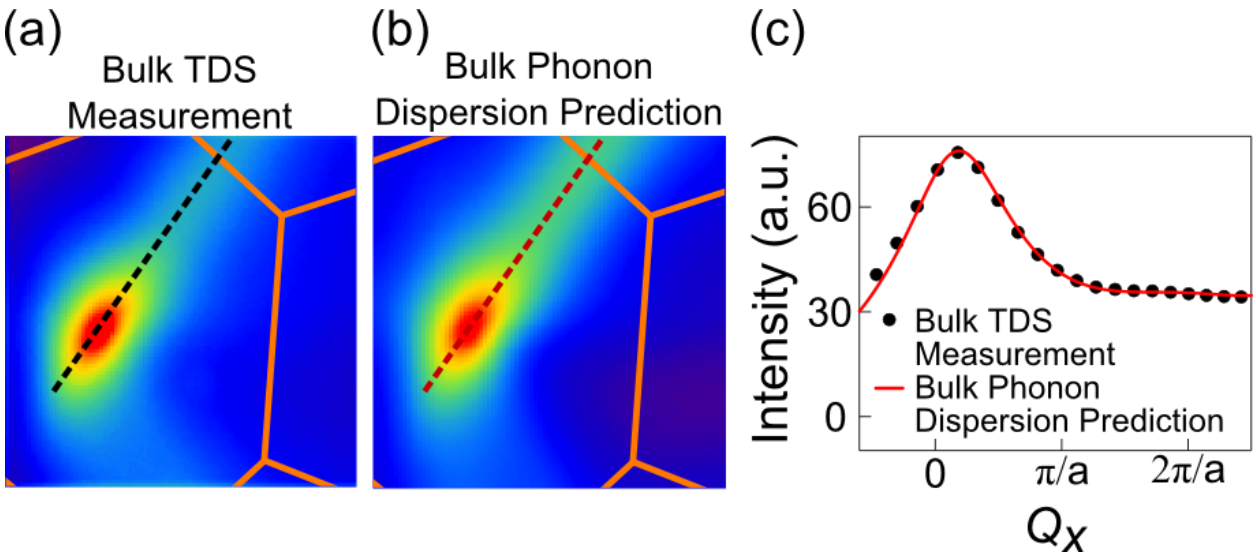

Figure 3-5: (a) experimentally observed TDS intensity for a bulk-like thickness of the SOI handle wafer. (b) Predicted first order TDS intensity based on the bulk phonon dispersion (c) Intensity profile of the measured TDS intensity (points) and TDS predicted from the bulk Si phonon dispersion (line) along the paths indicated in (a) and (b).

traverse from near the zone center to near the zone edge. The profiles are scaled using a single multiplicative scaling factor to match the observed and predicted TDS profiles. The images and extracted profile show good agreement between the observed and predicted TDS. TDS scattering patterns from Si nanomembranes with thicknesses of 315, 44, 28 and 6 nm are shown in Figure 3-6 (a)-(d). The intensity in the image is normalized to the highest value, which is the truncation rod. Membranes with reduced thicknesses show a lower TDS intensity and what appears to be a relative increase in the intensity of the truncation rod.

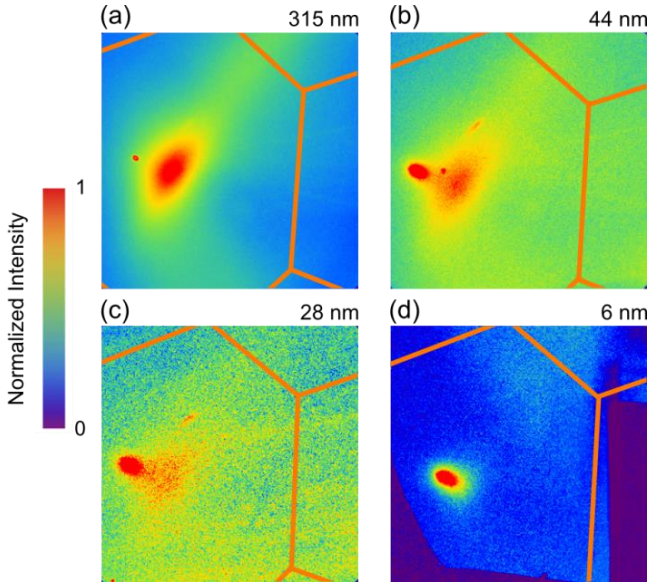

Figure 3-6: (a)-(d) Nanomembrane TDS intensity distributions for membranes with thicknesses of 315, 44, 28, and 6 nm, normalized to the TDS intensity maximum in each image. The bright spot to the left of the maximum in the diffuse scattering arises from the crystal truncation rod. Orange lines represent zone boundaries.

The first result is that the TDS intensity varies linearly with thickness in the nanometer regime. Figure 3-7 (a) shows the expected scaling of TDS of silicon up to a thickness of a few hundred microns. The maximum in intensity occurs at the x-ray attenuation length of silicon. The plot indicates the expected linearity of TDS intensity with thicknesses in the sub-micron thickness regime. Figure 3-7 (b) and (c) show the variation in TDS intensity as a function of thickness in the Si nanomembrane samples. The variation is shown at two different,

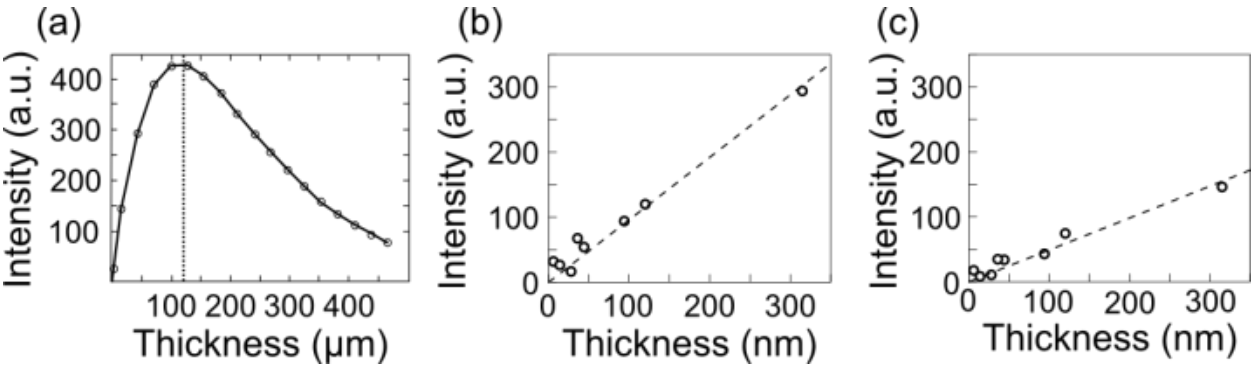

Figure 3-7: (a) Expected thickness scaling of x-rays TDS for samples in the few hundreds of microns region. The maximum in TDS intensity occurs at the attenuation length of Si.

representative points in reciprocal space, one from near the zone center (b) and one from near the zone boundary (c), with $Qx = 2\pi/a$. Sample-to-sample intensity variations in the small thickness regime arise partially due to the small deviations in sample orientation generated by the sample mounting procedure. This causes the path sampled in reciprocal space to be slightly different, passing either closer or farther from the zone center resulting and intensity dependence on sample orientation as well as thickness.

For thicker membranes, such as the 315 nm-thick membrane, the TDS intensity distribution closely matches the bulk intensity distribution with a slight deviation observed near the zone edge. The deviation near the zone edge becomes more apparent and pronounced with decreasing membrane thickness, such as the 44 and 28 nm-thick samples. In the thinnest membranes, such as the 6 nm-thick sample, the TDS signal at large wavevectors coincides with a large scattering contribution from the residual, unsubtracted background and static scattering from the oxide layer.

The deviation in the TDS intensity observed from silicon nanomembranes samples is apparent in the dependence of the TDS intensity on the wavevector component *Qx*. Figure 3-8 (a)-(d) (black dots) shows the dependence of TDS intensity on *Qx*. The profiles are extracted

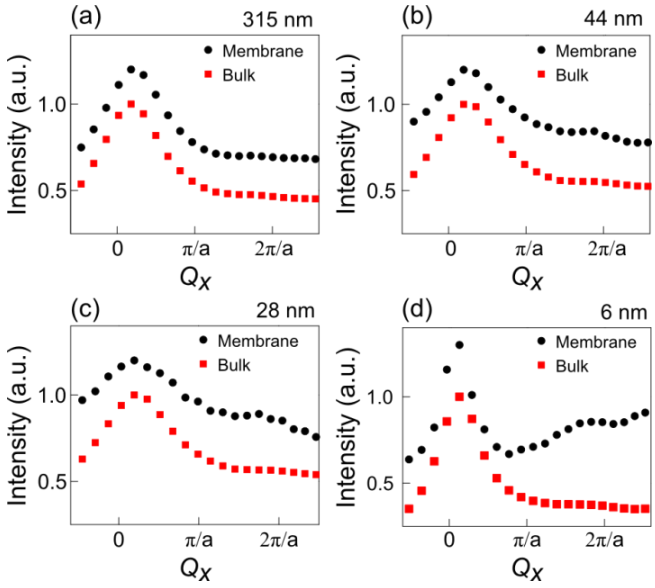

Figure 3-8: Dependence of the TDS intensity on the wave vector Qx for (a) 315, (b) 44, (c) 28, and (d) 6 nm membranes (black circles) and for bulk-like regions of the SOI handle wafer for each sample (red squares). The intensity profiles are normalized to unity at their maxima and offset vertically for clarity. The central maximum in (d) is sharper than in thicker samples due to a small difference in the sample orientation.

along the high intensity streak extending from the maximum in the TDS intensity towards the right corner, along the path shown in Figure 3-5. This corresponds to a reciprocal space path which starts near the zone center and extends along the high symmetry Γ to X direction. The red squares correspond to a profile taken from a bulk region near the membrane sample to which they are being compared. The membrane and bulk profiles are normalized to unity at their peak intensity of one, and offset for clarity. A broad excess in the TDS intensity is easily observed in these profiles between Qx = 3/2 π/a and 2π/a.

The observed excess at large wavevectors could be accounted for by modifying the phonon energy at those wavevectors. A confinement-induced reduction in the phonon energy by as little as 1-2 meV would be sufficient to yield an increase of 10% in TDS intensity at large-wavevectors. This would be consistent with previous results where confinement energies on the order of 0.5 meV in 30-nm-thick membranes have been established in the

small-wavevector regime.[23] While these deviations are consistent with the energy scale of these previous results, they occur at larger wavevectors at which different modes of vibration are relevant.

The predicted phonon dispersions of nanomembranes available in the literature are based on elasticity theory, as discussed in the previous section. The continuum elastic approximation limits these calculations to long wavelength modes for which the length scale imposed by atomic bonding is irrelevant. A more detailed comparison of the experimental results with theory will require the computation of phonon dispersions based on atomistic rather than continuum theories. Such predictions yield similar large-surface-displacement vibrational modes with very low frequencies in Si nanowires[38], but are not yet available for Si membranes with thicknesses of many nanometers.

3.3 Development of 3-D phonon anisotropy from spatial confinement in silicon nanomembranes

The next step is to extend the range of phonon wavevectors that can be studied by scattering techniques at the nanoscale by probing the population of phonons in a three-dimensional momentum-space volume over an extremely wide range of wavevectors, extending from near the zone center to the Brillouin zone boundary. These synchrotron x-ray TDS measurements probe phonon populations across the entire three-dimensional Brillouin zone of a silicon nanomembrane and expose a significant anisotropy in the phonon population.

The vibrational properties of nanoscale crystals involve effects arising both from the atomic-scale crystal structure and from the overall shape of the crystal. The frequencies and displacements associated with the vibrational modes of nanomaterials have a complex

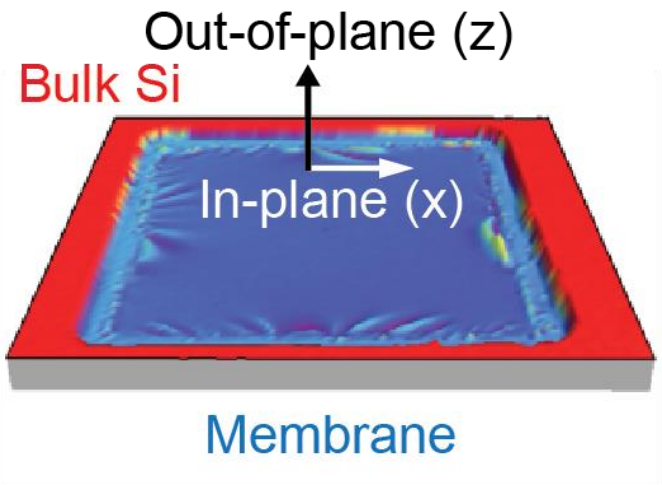

Figure 3-9: Suspended 21-nm-thick silicon membrane. The thin dimension of the membrane is termed the out-of-plane z direction.

dependence on spatial frequency because spatial confinement lifts the requirement that modes be periodic. Crystallographic directions that are equivalent in the bulk (e.g. [001], [100], and [010]) can exhibit anisotropy in low-dimensional nanostructures. The resulting vibrational modes of nanomaterials involve atomic displacements for which the bulk description in terms of longitudinal and transverse polarizations is not strictly correct.[36,37,39] The in-plane and out-of-plane directions in a nanoscale sheet like the one shown in Figure 3-9, for example, have distinct features in the phonon dispersion.[37, 39]

The 3D contour plot shown in Figure 3-10 (a) shows phonon-energy isosurfaces for the transverse acoustic (TA) mode of bulk Si calculated by diagonalizing the dynamical matrix for silicon using bulk elastic constants.[40] The TA mode is the lowest energy mode in silicon and provides the dominant contribution to the TDS intensity, due to the consequent high thermal population of phonons. Isosurfaces of different phonon energies are shown in different colors, with a cutout being provided in the foreground to reveal the lower energy phonons near the zone center. Figure 3-10 (a) demonstrates the complex but symmetric nature of the bulk phonon dispersion. This complex phonon structure demonstrates the necessity for a three-dimensional

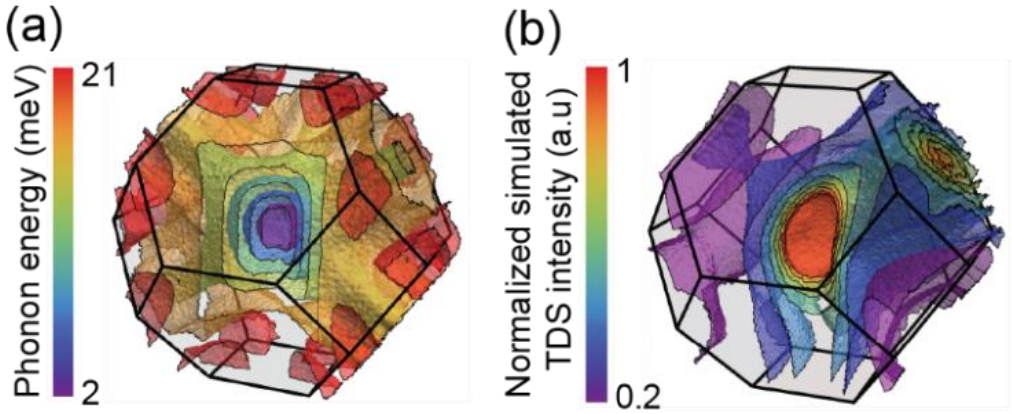

Figure 3-10: (a) Bulk phonon dispersion of Si, with a sector of the plot removed to expose low-phonon-energy contours. (b) Simulated distribution of x-ray TDS (TDS) intensity inside the (-3 -1 1) zone using the bulk Si phonon dispersion. A sector of the prediction has been removed to expose regions of high intensity. High intensity streaks occur along <111> and <001> directions, as was apparent in the phonon dispersion

phonon probe, particularly in nanomaterials where the bulk symmetry can be broken. A quantitative prediction of the three-dimensional TDS intensity map from a bulk silicon crystal is shown in Figure 3-10 (b), simulated using the approximation that the scattering is dominated by the first-order TDS process. Again, isosurfaces of different colors show different levels of predicted TDS intensity throughout the Brillouin zone, with a cut out being provided to show the high intensity regions near the zone center. The zone depicted is the (-3, -1, 1) zone measured in this experiment, as the intensity and shape of the TDS distribution changes with the particular reciprocal lattice vector it is centered around. Figure 3-10 (b) demonstrates the motivation for moving TDS scattering techniques from the arbitrary paths sampled in section 3.2 to a more systematic sampling methodology presented here.[41,42]

In order to sample the population of phonons in a three-dimensional momentum-space volume, the experimental arrangement shown in Figure 3-3 is further developed to allow TDS to be probed in a three-dimensional volume of reciprocal space spanning the entire Brillouin zone. X-ray scattering patterns were collected in a transmission geometry in which the incident beam

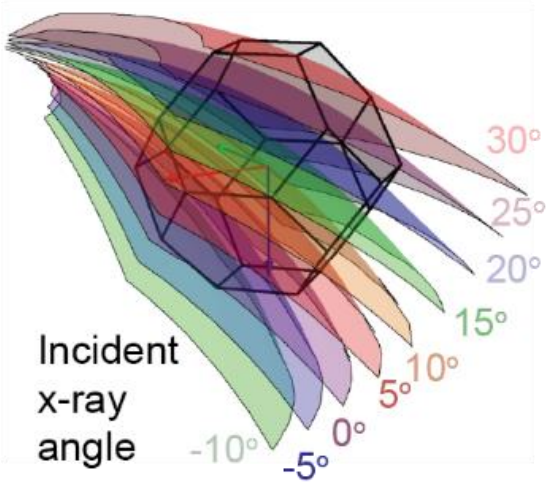

Figure 3-11: X-ray TDS collects information about the phonon population along the two-dimensional surface of the Ewald sphere, which is swept through the Brillouin zone by rotating the sample through a series of values of the incident angle of the x-ray beam.

passed through the nanomembrane, at an angle respect to the surface normal. Varying the x-ray incident angle relative to the membrane normal causes the condition for the quasi-elastic x-ray scattering occurring during TDS and visualized using the Ewald sphere construction, to sweep through reciprocal space. This is equivalent to collecting a series of closely separated slices, each providing a two-dimensional map of TDS intensities, sampling a set of cross-sections spanning the Brillouin zone, as shown in Figure 3-11.

Orientations spanning an angular range of 40° in 5° increments is sufficient to probe regions spanning the Brillouin zone centered on the (-3 -1 1) reciprocal lattice point. TDS intensity distributions were collected from membranes with thicknesses of 97 and 21 nm and, for comparison, bulk-like micrometer-thick regions of the silicon frame near the edges of the membranes. The background contribution to the detected intensity arising from scattering from the x-ray optics was measured by directing the incident beam through a frame in which the membrane had been mechanically removed and was subtracted from the TDS data.

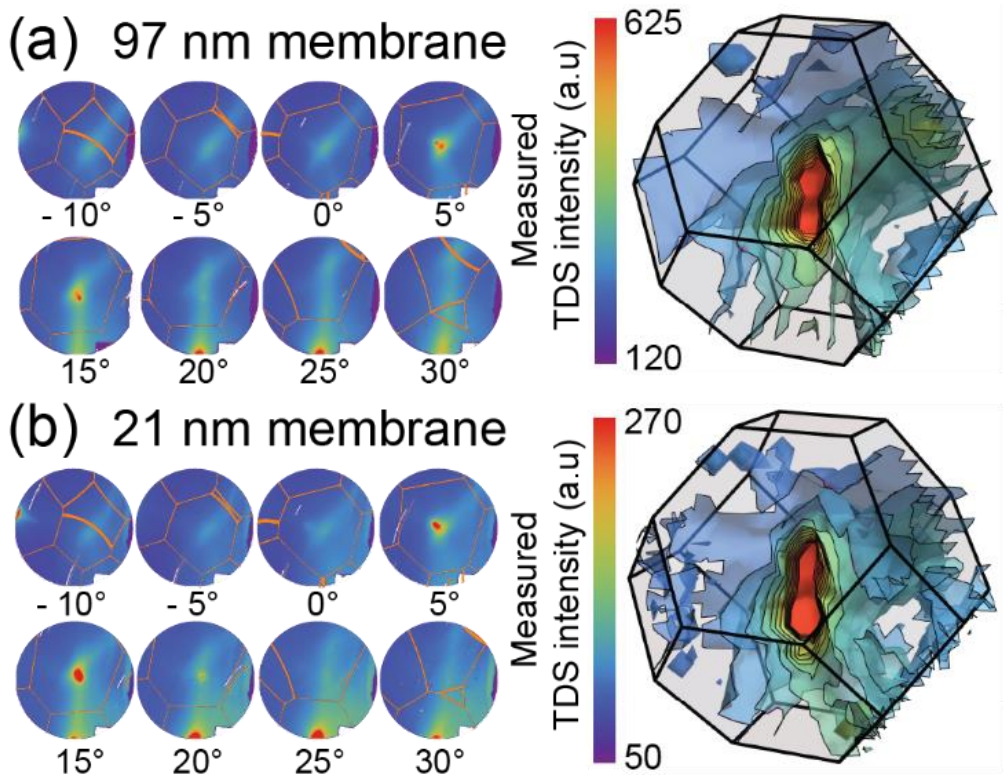

Figure 3-12: Scattering patterns with thicknesses of (a) 97 nm (b) 21 nm, acquired with incident angles from -10° to 30° in 5° steps. The image acquired at an incident angle of 10° excites the highly intense (-3 -1 1) Bragg reflection of the nanomembrane, saturating the detector, and is thus not shown. The crystal truncation rod of the Si sheet appears as an intense highly localized feature in several images. The three-dimensional representation of the experimental TDS intensity constructed from the detector images appears in the right panels of (a) and (b). The data has been removed from a sector of the Brillouin zone in order to show the high-intensity contours.

Figure 3-12 shows TDS intensity distributions for the nanomembranes with thicknesses of 97 nm (Figure 3-12 (a)) and 21 nm (Figure 3-12 (b)). Each intensity distribution in (a) and (b) represents the TDS intensity at different incident angles captured by the cross sections shown in Figure 3-11. Boundaries of the Brillouin zones are show are orange lines. A three-dimensional representation of the TDS scattering constructed from the detector images is also shown. The recorded intensities at each angular setting are multiplied by an angle-dependent factor to account for the slight difference in volume of the sample probed in each geometry. Intense scattering is observed (i) near the zone center, due to the large population of small-wavevector

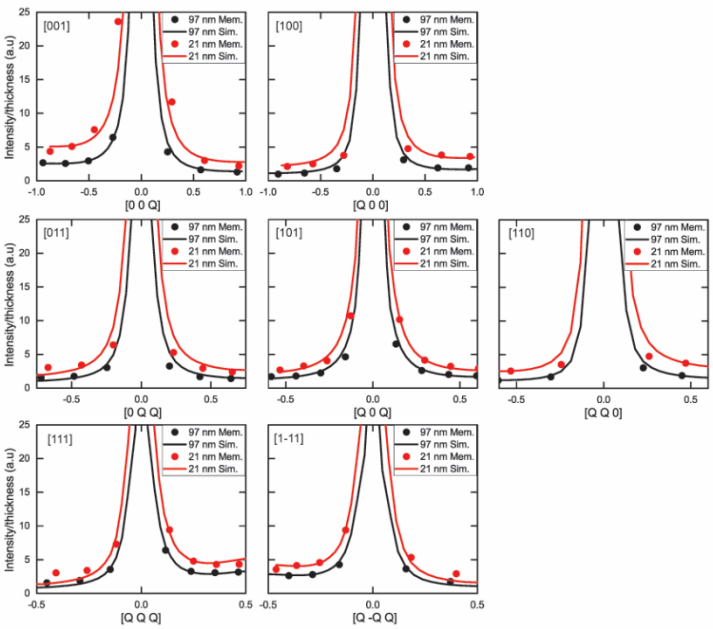

Figure 3-13: High-symmetry-direction profiles of the TDS intensity. The intensity is normalized by x-ray data acquisition time and membrane thickness. Black and red dots represent measured intensities from nanomembranes with thicknesses of 97 nm and 21 nm, respectively. Black and red lines are first-order TDS simulated using the bulk phonon dispersion fit to the corresponding data by a single overall scaling parameter, and provide a guide to the eye for comparing the measured intensities with those expected from bulk-like samples.

phonons and (ii) along diffuse streaks close to high-symmetry directions where phonon modes have low frequencies. The three-dimensional representation extracted from the detector images qualitatively reproduces the predicted shape of the TDS intensity shown in Figure 3-10.

The straightforward relationship between the wavevector of scattered x-rays and crystal momentum within the Si membrane allows the intensity distribution to be readily interpreted in terms of the phonon wavevector. The TDS intensity along arbitrary crystallographic directions was extracted by numerically resampling the intensity onto a three-dimensional grid spanning the Brillouin zone and plotted as a function of the reciprocal space vector connecting each point to the (-3 -1 1) zone center. The experimental and analytical techniques presented here represent an advancement over previous TDS measurements in that it allows the extraction of intensity profiles along the high symmetry crystallographic directions. Intensity distributions along

<100>, <110>, and <111> high-symmetry directions, are shown in Figure 3-13 for the 97 nm-thick and 21 nm-thick membranes. The [010], [-1 1 1], and [1 1 -1] directions are not shown in Figure 3-13 because there is low density of points sampling the intensity along those directions as a result of the small number of Ewald sphere slices intersecting those paths. The intensity axis in Figure 3-13 is normalized by the membrane thickness to allow the profiles for the different crystallographic directions to be compared. The predicted TDS intensity based on the bulk silicon phonon dispersion is scaled by a single fitting parameter to fit the experimental data. These fits show that the shape of the TDS scattering is qualitatively similar to the observed experimental data and are used to guide the eye.

The variation of TDS intensity with membrane thickness can be explored precisely by plotting the TDS intensity along directions separated by fine angular steps, shown in Figure 3-14 (a) and (b). Figure 3-14 shows the ratio of the TDS intensity acquired from the 21 nm membrane to the intensity from the bulk-like 97 nm membrane along these directions. Previous study has shown that the intensity of scattering from membranes at approximately 100-nm thicknesses follows the scaling proportional to thickness expected for bulk dispersions.[41,42] If the intensity of scattering from the 21 nm membrane was proportional only to nanomembrane thickness, the intensity ratios in Figure 3-14 (a) would exhibit no dependence on direction and have a constant value of 0.22, as indicated by the horizontal dashed line in Figure 3-14 (a) and (b). Instead, the dependence of the TDS intensity on reciprocal space direction is dramatically different for the two nanomembrane samples, as seen from the anisotropy in the intensity ratio, especially for wavevectors shorter than half the zone radius (or wavelengths of a few nanometers).

Figure 3-14 shows that the phonon population of the previously equivalent in-plane and out-of-plane directions is anisotropic for the smaller nanomembrane thickness. As *Qz* increases,

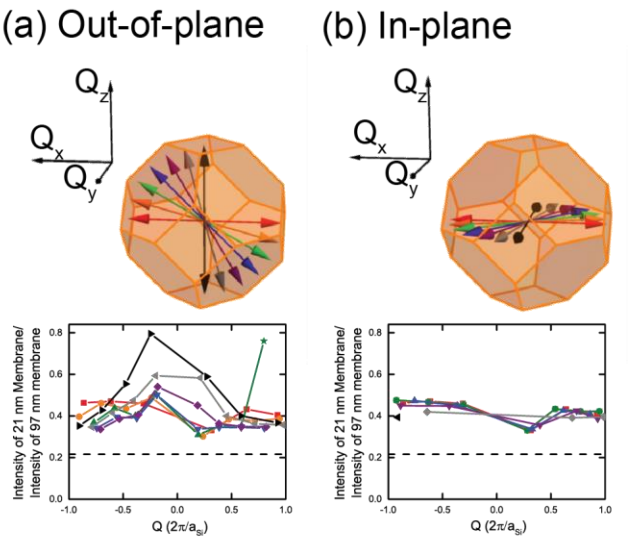

Figure 3-14: Anisotropy of nanomembrane TDS. Ratios of intensities from 21 nm-thick and 97 nm-thick silicon nanomembranes along (a) out-of-plane and (b) in-plane directions. The directions of the profiles are shown in the corresponding color in the inset schematic of the Brillouin zone. The anomalously intense point plotted with a star includes an artifact due to powder diffraction from the x-ray optics and thus does not fit the overall trend. The horizontal dashed line indicates the expected ratio in intensity between the 21 nm-thick and 97 nm-thick membranes assuming linear scaling of the TDS intensity with thickness.

the ratio of scattered intensity increases near the zone center. At its maximum, the ratio of the TDS intensities for the 21 nm and 97 nm thicknesses is 400% larger than the value expected from the linear scaling observed in thicker samples and 200% larger than the in-plane ratio.[41] This result indicates that there is an anisotropy in the TDS intensity from the 21 nm-thick membrane that does not occur in the bulk or in the 97 nm-thick membrane. The in-plane series of directions, Figure 3-14 (b), does not exhibit a dependence on the profile direction, and the intensity distribution in the in-plane directions is the same in both 21 nm-thick and 97 nm-thick membranes. TDS ratio plots from the two bulk-like membrane frames (see supplemental material) show that bulk Si does not exhibit the directional anisotropy observed in nanomembranes.

Figure 3-15 shows the ratio of intensity between the bulk frame of the 21 nm membrane and the frame of the 97 nm membrane. The in-plane and out-of-plane directions are plotted as

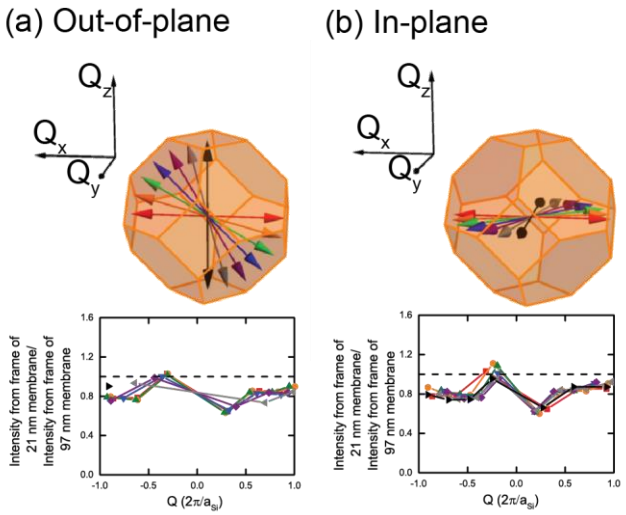

Figure 3-15: Absence of anisotropy in bulk Si. The ratio of intensity between the bulk frame of the 21 nm membrane and the frame of the 97 nm membrane. The (a) out-of-plane and (b) in-plane directions are plotted as was done for the membranes in Figure 3-14. Neither the in-plane or out-of-plane direction profiles show evidence of the anisotropy observed in the membrane

was done for the membranes in Figure 3-14. Neither the in-plane or out-of-plane direction profiles show evidence of the anisotropy observed in the membrane. The in-plane and out-of-plane ratios are slightly below one due to artifacts arising from differences in the total thickness sampled for the bulk measurement and from small differences in the sample orientation that lead to slightly different regions being sampled in reciprocal space with slightly different phonon populations. The feature at Q=0 in the bulk ratios in Figure 3-15 results from differences in the sample geometry, leading to a small error in the sample wavevector being compared.

It is also apparent in Figure 3-13 and Figure 3-14 that the 21 nm-thick membrane produces a higher TDS intensity per unit thickness than the 97 nm-thick membrane across the entire Brillouin zone. There are several possible causes for increased intensity including contributions from a relative increase in the static background scattering or a relative increase in the importance of scattering from the membrane surface, which would contribute a larger fraction of the total scattering observed from the 21 nm-thick membrane sample.

Existing experimental and theoretical results provide some insight into modes with in-plane wavevectors. Brillouin light scattering measurements, while sensitive to out-of-plane atomic displacements, are limited to the measurement of in-plane phonon wavevectors.[9,24,25,27,28] These measurements show evidence of the conversion of bulk TA and longitudinal acoustic modes into flexural and dilatational modes as predicted by elastic continuum theory, evidenced by the creation of a quadratic dispersion near the zone center and higher order quantized modes.[24,28,36,37,39,43,44] The in-plane dispersions of the flexural and dilatational modes of the lowest energy out-of-plane mode number *n* have lower energies than the bulk transverse and longitudinal modes in Si.[41,42] The low-energy vibrational modes of thin Si sheets change the total phonon density of states and thus modify total phonon population probed in TDS experiments.[37,39] The introduction of lower-energy phonon modes would contribute to the overall rise in TDS intensity observed in the scattering from the 21 nm-thick membrane sample through an increase in low-frequency phonon population with a correspondingly high x-ray scattering cross-section.[41, 42]

There is far less insight available into the out-of-plane phonon mode energies, for which $Qx=0$. Elastic calculations predict a quantization of modes in the out-of-plane direction due to the finite thickness in that direction. The quantized modes in the out-of-plane direction have wavevectors given by $Qz=n\pi/d$, where d is thickness of the membrane. Accordingly, the out-of- plane phonon modes can no longer be thought of as a continuous dispersion.[37] The in-plane wavevector remains continuous as in the bulk dispersion.[37,39] However the dispersion of out-of-plane acoustic phonons predicted by elastic continuum theory is linear with a slope dependent on the elastic constants, which take on their bulk values in elastic calculations.[37, 39] These elastic theory predictions do not predict the development of new out-of-plane modes.

A possible explanation for the higher phonon population in out-of-plane modes is a softening of the elastic constants of the membrane in comparison to the bulk. Softening would lead to a decrease in the frequencies of out-of-plane vibrational modes, with a larger reduction of the elastic constants in the out-of-plane direction than in the in-plane direction. Mechanical studies of ultrathin silicon suggest that the elastic properties are also affected by the reduced dimensionality of the membrane.[45,46] In nanoscale silicon free-standing beams, the Young's Modulus was observed to decrease from 160 GPa to 108 GPa when the thickness was reduced from 200 nm to 50 nm.[47] This reduction in the effective elastic modulus is attributed to surface effects the presence of the native oxide, and fabrication-induced defects.[48] This effect is not captured in the elastic continuum calculations discussed above because elastic predictions rely on the bulk elastic constants.

However, continuum theories have limited validity in the large-wavevector regime and a full comparison will require a more complete atomistic picture. A limited number of molecular dynamics calculations have been performed for membranes as thick as 20 nm.[9,10] The phonon dispersion calculated by molecular dynamics extends into the large-wavevector regime and are consistent with elastic continuum theory, but has only been presented for the in-plane directions.[9,10] However the molecular dynamics calculations show evidence of an average softening of the elastic moduli, especially for modes that create out-of-plane atomic displacements, which would be consistent with anisotropy in the softening of the elastic constants.[10]

3.4 Modification of phonon spectrum in Si/SiGe/Si trilayer membranes

Portions of this section were adapted with permission from McElhinny et al., MRS Advances, **1, 3263-3268, (2016). Copyright (2016) by the Materials Research Society.*

Additional modifications to the phonon dispersion may occur through the alloying of Si nanomaterials with Ge. The structure of the Si/SiGe/Si trilayer and of uniform-composition Si nanomembranes considered in this study are shown in Figure 3-16. The details of the processing steps involved in membrane fabrication processes are outlined in Chapter 2. The Si/SiGe/Si nanomembrane, shown in Figure 3-16, has a total thickness of 60 nm. The SiGe layer has a composition of $Si_{0.76}Ge_{0.24}$, and each Si and SiGe layer has a nominally equal 20 nm thicknesses in order to minimize bending stresses. Optical profilometry images illustrating the flatness of Si/SiGe/Si and Si nanomembranes with thickness of 60 nm, 97 nm, and 21 nm are shown in Figure 3-16 (c), (d) and (e), respectively.

The experimentally measured distributions of x-ray TDS intensities for three nanomembrane samples are shown in Figure 3-17. These scattering patterns were collected with the same experimental setup as described in the previous sections. The scattering patterns were collected from the trilayer Si/SiGe/Si nanomembrane with a total thickness of 60 nm, and Si membranes with thicknesses of 21 nm and 97 nm, respectively. These scattering patterns are

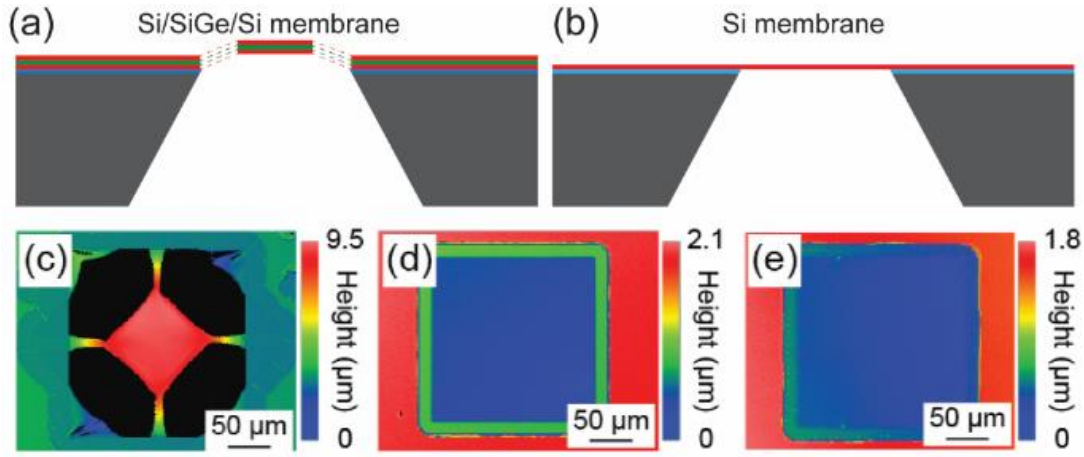

Figure 3-16: Schematics of (a) Si/SiGe/Si trilayer nanomembrane and (b) Si nanomembrane. Optical profilometry images of (c) the Si/SiGe/Si trilayer connected to the substrate by narrow arms, and Si nanomembranes with thicknesses of (d) 97 nm and (e) 21 nm.

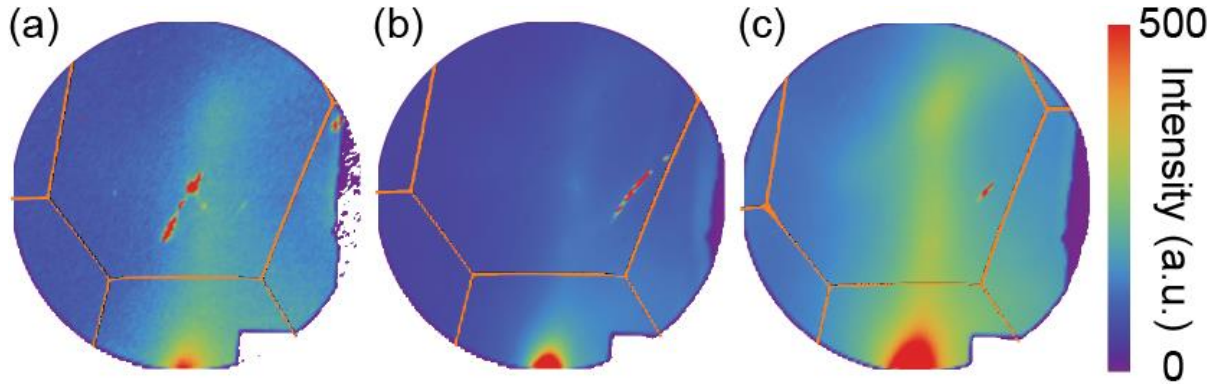

Figure 3-17: X-ray TDS patterns acquired from (a) a 60 nm-thick, Si/SiGe/Si trilayer nanomembrane, (b) a 21 nm-thick Si nanomembrane, and (c) a 97 nm-thick Si nanomembrane. Orange lines are overlaid on the detector image to indicate the intersection of the Ewald sphere with the Brillouin zone boundaries.

two-dimensional slices of the three-dimensional reciprocal space of the nanomembranes. The intersection of the two-dimensional scattering pattern with the three-dimensional boundaries of Brillouin zones centered at the diamond cubic reciprocal lattice points are drawn as orange lines superimposed on the scattering patterns in Figure 3-17. The zone with the largest area at the tops of the images in Figure 3-17 is centered on the (-3 -1 1) reciprocal lattice point.

Each scattering pattern in Figure 3-17 exhibits a broad distribution across the entire detector as well as streaks of locally higher TDS intensity. These streaks of intensity extend approximately vertically in the image as well as along a line from the center to the upper right corner. The loci of wavevectors along these streaks correspond to directions in reciprocal space close to the high symmetry directions, [111] and [100], respectively, of Si and Ge. Phonon modes along these directions have lower frequency and hence exhibit a larger TDS intensity. Two additional sets of features are also apparent in Figure 3-17. An intense region at the bottom of the detector arises from the high population of low-frequency modes near the Brillouin zone center. Sharp highly localized high-intensity artifacts in the scattering pattern arise from diffraction from optical elements that was not completely obscured by the Pb shielding.

The observed intensities can be systematically compared with the TDS scattering pattern expected for bulk Si by plotting the simulated and observed intensities along specific directions of the TDS data. Figure 3-18 (a)-(c) show the observed and simulated intensity along a direction of the images in Figure 3-17 that lies approximately along [010]. Each profile is normalized by the thickness to illustrate any regions of unexpectedly high intensity. Figure 3-18 (d)-(f) show profiles extracted along [111] directions. For each sample the simulated intensity is scaled by a single overall parameter to fit both profiles. The 21 nm Si nanomembrane exhibits excess intensity along both crystallographic directions, consistent with the work Section 3.3. The Si/SiGe/Si trilayer yields an intensity distribution that is qualitatively similar to the Si simulation.

There is excellent agreement between the observed and simulated intensity for the thickest, 97 nm, Si nanomembrane. As is apparent in Figure 3-17, the thinner Si nanomembrane and the Si/SiGe/Si trilayer nanomembrane exhibit qualitatively similar distributions of scattered intensity. A comparison with the 21 nm nanomembrane intensity with the simulation shows that the experimentally observed intensity follows approximately the expected distribution in

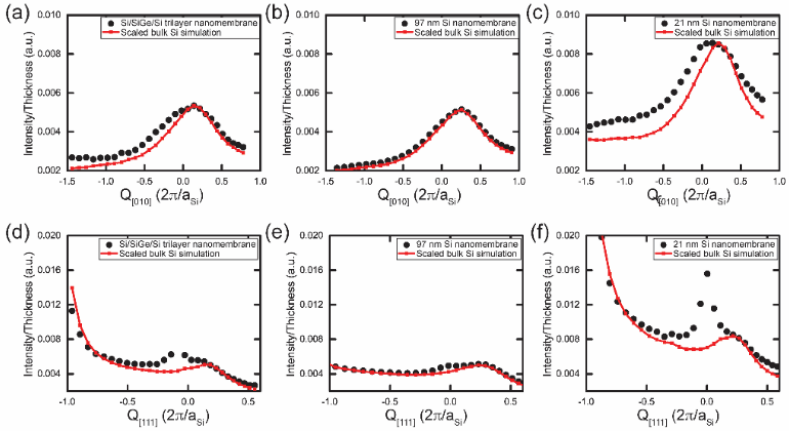

Figure 3-18: TDS intensity profiles extracted along the intense streaks of intensity observed in Figure 3-17(a), (b), and (c) Observed (points) and simulated (red line) intensity profiles approximately along [010]. (d), (e), and (f) Observed (points) and simulated (red line) intensity profiles approximately along [111]. Sharp features in (d) and (f) and the weaker feature in (e) at Q[111] ≈ 0 correspond to the intensity from the crystal truncation rod of the membrane and do not arise from TDS.

reciprocal space, but with a higher-than-expected intensity. This excess in intensity can arise from the modification of phonon frequencies due to the free surface mechanical boundaries.[41] The mechanical discontinuities in the Si/SiGe/Si system are not sufficiently large to introduce spatial confinement of the phonon modes and consequently the intensity of the scattering is quantitatively very similar to what would be expected from a bulk Si membrane of the same thickness. There is, however, an excess of intensity of 3.75% along [010] in the Si/SiGe/Si trilayer membrane and a broadening of the TDS profile, pointing to vibrational differences between Si/SiGe/Si and the thicker Si membrane. Possible origins of the enhancement in scattering from SiGe in comparison with Si include the larger atomic scattering factor of Ge atoms with the SiGe layer or reduced phonon frequencies due to alloying.

3.5 Conclusions

To study the impact of spatial confinement on the vibration frequencies of nanoscale semiconductors, flat single crystal Si and Si/SiGe/Si nanomembranes were fabricated with dimensions of 200 μm × 200 μm with thicknesses from 300 nm to as small as 6 nm. Synchrotron x-ray TDS studies of phonon populations throughout the entire Brillouin zone in Si nanomembranes show an increased population, with phonons with out-of-plane phonon wavevectors showing an additional excess in population.

A comparison of the intensities of different thicknesses of silicon nanomembranes shows that the intensity deviates from the expected thickness scaling and that an anisotropy in the TDS intensity has been created with the same symmetry as the sample geometry. These deviations from bulk results could be explained by the development of new lower energy modes across the entire Brillouin zone and a modification of the elastic constants resulting in a higher phonon

population. However, the acoustic mismatch between Si and SiGe layers is insufficient to modify the vibration properties through spatial confinement and instead shows evidence of small changes due to alloying. X-ray TDS measurements allow the phonon population in nanoscale materials to be probed across the entire range of relevant wavevectors and exposes systematic trends in phonon population as a function of thickness and composition.

Future time-resolved diffuse scattering experiments offer a possible extension of this technique, providing additional insight into both the effects of alloying and spatial confinement on phonon lifetimes as well as populations.[49, 50] Potential extensions of this work include extending it probing 1-D structures like nanowires or ribbons or providing additional surface treatments to modify the acoustic boundary conditions. Additionally, demonstration of modifications of the phonon dispersion out to large wavevectors should encourage the simulation of the reasons for these changes and subsequent incorporation of the new dispersion into future predictions of the thermal properties of nanomaterials. This work will also help to isolate the contributions of the phonon dispersion to the thermal properties of nanomaterials, helping to decouple clumped parameters like thermal conductivity.

3.6 References

1. Flensburg, C. & Stewart, R. F. Lattice dynamical Debye-Waller factor for silicon. *Phys. Rev. B* **60,** 284–291 (1999).
2. Ashcroft, N. W. *Solid state physics*. (Saunders College Publishing, 1976).
3. Holt, M. V. S-ray studies of lattice dynamics.
4. Wei, S. & Chou, M. Y. Phonon dispersions of silicon and germanium from first-principles calculations. *Phys. Rev. B* **50,** 2221–2226 (1994).
5. Cahill, D. G. *et al.* Nanoscale thermal transport. II. 2003-2012. *Appl. Phys. Rev.* **1,** 011305 (2014).
6. Balandin, A. A. & Nika, D. L. Phononics in low-dimensional materials. *Mater. Today* **15,** 266–275 (2012).
7. Maldovan, M. Sound and heat revolutions in phononics. *Nature* **503,** 209–217 (2013).
8. Johnson, J. A. *et al.* Direct measurement of room-temperature nondiffusive thermal transport over micron distances in a silicon membrane. *Phys. Rev. Lett.* **110,** 025901 (2013).
9. Neogi, S. *et al.* Tuning thermal transport in ultrathin silicon membranes by surface nanoscale engineering. *ACS Nano* **9,** 3820–3828 (2015).
10. Neogi, S. & Donadio, D. Thermal transport in free-standing silicon membranes: influence of dimensional reduction and surface nanostructures. *Eur. Phys. J. B* **88,** 1–9 (2015).
11. Maldovan, M. Narrow low-frequency spectrum and heat management by thermocrystals. *Phys. Rev. Lett.* **110,** 025902 (2013).
12. Maldovan, M. Phonon wave interference and thermal bandgap materials. *Nat. Mater.* **14,** 667–674 (2015).

13. Svensson, E. C., Brockhouse, B. N. & Rowe, J. M. Crystal dynamics of copper. *Phys. Rev.* **155,** 619–632 (1967).

14. Schwoerer-Böhning, M., Macrander, A. T. & Arms, D. A. Phonon dispersion of diamond measured by inelastic x-ray scattering. *Phys. Rev. Lett.* **80,** 5572–5575 (1998).

15. Cahill, D. G. *et al.* Nanoscale thermal transport. *J. Appl. Phys.* **93,** 793 (2003).

16. Chen, G. Phonon heat conduction in nanostructures. *Int. J. Therm. Sci.* **39,** 471–480 (2000).

17. Ju, Y. S. & Goodson, K. E. Phonon scattering in silicon films with thickness of order 100 nm. *Appl. Phys. Lett.* **74,** 3005–3007 (1999).

18. Liu, W. & Asheghi, M. Thermal conductivity measurements of ultra-thin single crystal silicon layers. *J. Heat Transf.* **128,** 75–83 (2006).

19. Jacoboni, C. & Reggiani, L. The Monte Carlo method for the solution of charge transport in semiconductors with applications to covalent materials. *Rev. Mod. Phys.* **55,** 645–705 (1983).

20. Pop, E., Dutton, R. W. & Goodson, K. E. Analytic band Monte Carlo model for electron transport in Si including acoustic and optical phonon dispersion. *J. Appl. Phys.* **96,** 4998–5005 (2004).

21. Asche, M. & Sarbei, O. G. Electron–phonon interaction in n-Si. *Phys. Status Solidi B* **103,** 11–50 (1981).

22. Torres, C. M. S. *et al.* Observations of confined acoustic phonons in silicon membranes. *Phys. Status Solidi C* **1,** 2609–2612 (2004).

23. Groenen, J. *et al.* Inelastic light scattering by longitudinal acoustic phonons in thin silicon layers: From membranes to silicon-on-insulator structures. *Phys. Rev. B* **77,** 045420 (2008).

24. Cuffe, J. *et al.* Phonons in slow motion: Dispersion relations in ultrathin Si membranes. *Nano Lett.* **12,** 3569–3573 (2012).

25. Cuffe, J. *et al.* Lifetimes of confined acoustic phonons in ultrathin silicon membranes. *Phys. Rev. Lett.* **110,** 095503 (2013).

26. Chávez, E., Cuffe, J., Alzina, F. & Torres, C. M. S. Calculation of the specific heat in ultra-thin free-standing silicon membranes. *J. Phys. Conf. Ser.* **395,** 012105 (2012).

27. Graczykowski, B. *et al.* Acoustic phonon propagation in ultra-thin Si membranes under biaxial stress field. *New J. Phys.* **16,** 073024 (2014).

28. Graczykowski, B. *et al.* Phonon dispersion in hypersonic two-dimensional phononic crystal membranes. *Phys. Rev. B* **91,** 075414 (2015).

29. Grimsditch, M., Bhadra, R. & Schuller, I. K. Lamb waves in unsupported thin-films - A Brillouin-scattering study. *Phys. Rev. Lett.* **58,** 1216–1219 (1987).

30. Balandin, A. & Wang, K. L. Effect of phonon confinement on the thermoelectric figure of merit of quantum wells. *J. Appl. Phys.* **84,** 6149–6153 (1998).

31. Balandin, A. & Wang, K. L. Significant decrease of the lattice thermal conductivity due to phonon confinement in a free-standing semiconductor quantum well. *Phys. Rev. B* **58,** 1544–1549 (1998).

32. Balandin, A. A. Nanophononics: phonon engineering in nanostructures and nanodevices. *J. Nanosci. Nanotechnol.* **5,** 1015–1022 (2005).

33. Zou, J. & Balandin, A. Phonon heat conduction in a semiconductor nanowire. *J. Appl. Phys.* **89,** 2932 (2001).

34. Hori, T., Shiga, T. & Shiomi, J. Phonon transport analysis of silicon germanium alloys using molecular dynamics simulations. *J. Appl. Phys.* **113,** 203514 (2013).

35. Garg, J., Bonini, N., Kozinsky, B. & Marzari, N. Role of Disorder and anharmonicity in the thermal conductivity of silicon-germanium alloys: A first-principles study. *Phys. Rev. Lett.* **106,** 045901 (2011).

36. Lamb, H. On waves in an elastic plate. *Proc. R. Soc. Lond. Ser. A* **93,** 114–128 (1917).

37. Bannov, N., Aristov, V., Mitin, V. & Stroscio, M. A. Electron relaxation times due to the deformation-potential interaction of electrons with confined acoustic phonons in a free-standing quantum well. *Phys. Rev. B* **51,** 9930–9942 (1995).

38. Thonhauser, T. & Mahan, G. D. Phonon modes in Si [111] nanowires. *Phys. Rev. B* **69,** 075213 (2004).

39. Bannov, N., Mitin, V. & Stroscio, M. Confined acoustic phonons in a free-standing quantum well and their interaction with electrons. *Phys. Status Solidi B* **183,** 131–142 (1994).

40. Holt, M. *et al.* Determination of phonon dispersions from x-ray transmission scattering: The example of silicon. *Phys. Rev. Lett.* **83,** 3317–3319 (1999).

41. Gopalakrishnan, G. *et al.* Thermal diffuse scattering as a probe of large-wave-vector phonons in silicon nanostructures. *Phys. Rev. Lett.* **110,** 205503 (2013).

42. Gopalakrishnan, G., Holt, M. V., McElhinny, K. M., Czaplewski, D. A. & Evans, P. G. Probing large wavevector phonons at the nanoscale via x-ray thermal diffuse scattering. *Adv. X-Ray Anal.* **56,** 82 (2013).

43. Solie, L. P. & Auld, B. A. Elastic waves in free anisotropic plates. *J. Acoust. Soc. Am.* **54,** 50–65 (1973).

44. Alizadeh, A., Rostami, A., Baghban, H. & Bahar, H. B. Tailoring electron–phonon interaction in nanostructures. *Photonics Nanostructures - Fundam. Appl.* **12,** 164–172 (2014).

45. Li, X. X., Ono, T., Wang, Y. L. & Esashi, M. Ultrathin single-crystalline-silicon cantilever resonators: Fabrication technology and significant specimen size effect on Young's modulus. *Appl. Phys. Lett.* **83,** 3081–3083 (2003).

46. Sadeghian, H. *et al.* Characterizing size-dependent effective elastic modulus of silicon nanocantilevers using electrostatic pull-in instability. *Appl. Phys. Lett.* **94,** 221903 (2009).

47. Bhaskar, U. *et al.* On-chip tensile testing of nanoscale silicon free-standing beams. *J. Mater. Res.* **27,** 571–579 (2012).

48. Sadeghian, H. *et al.* Effects of size and defects on the elasticity of silicon nanocantilevers. *J. Micromechanics Microengineering* **20,** 064012 (2010).

49. Trigo, M. *et al.* Imaging nonequilibrium atomic vibrations with x-ray diffuse scattering. *Phys. Rev. B* **82,** 235205 (2010).

50. Trigo, M. *et al.* Fourier-transform inelastic X-ray scattering from time- and momentum-dependent phonon-phonon correlations. *Nat. Phys.* **9,** 790–794 (2013).

Chapter 4: Structural dynamics of reconfigurable organic-inorganic interfaces

4.1 Introduction

The creation of materials incorporating optically reconfigurable interfaces between organic and inorganic components provides access to a wide range of new electronic and optical phenomena with both fundamental and practical importance. Dynamically reconfiguring the structure of an interfacial molecular monolayer through the use of external stimuli has the potential to provide precise control over charge transfer dynamics, energy offsets of interfacial electronic states, dipole moments or polarizations, and vibrational phenomena. In the past, various structural configurations have been created by varying the conditions under which the monolayers are assembled. Such studies indicate that changes in the structural state can include changes in the molecular height and conformation[1–4] and an increase or decrease in the dipole moment and net polarization.[5–7]

Photoresponsive materials are attractive because optical control is intrinsically clean, can induce fast responses, and can be delivered from a remote source.[2,8] These reconfigurable materials are being developed for a variety of exciting applications including molecular machines,[9,10] organic electronics,[11] solar energy harvesting,[12,13] high density information storage,[14] and smart surfaces with applications in switchable wetting,[15,16] directing liquid crystal alignment,[17] and catalysis.[18] For example, computational studies proposed that it could be possible to create high-energy-density solar fuels through a mechanism in which energy is stored in the metastable molecular configuration and released through isomerization into the stable *trans* isomeric state via optical absorption.[12,19,20] This technology was recently realized through the creation of a high energy density azobenzene/graphene hybrid as a solar fuel exhibiting a

high energy density of up to 112 W h kg^{-1} with a half-life of 33 days.[11] Additionally, a photoresponsive cross-linked azobenzene/polymer assembly has demonstrated its feasibility as a high performance light driven actuator.[21] Similarly, the structural cues provided by azobenzene monolayers can drive photoinduced alignment in liquid crystal films and create surfaces with photoswitchable wettability.[1,17,22,23]

One particular area where this reconfigurability presents exciting opportunities for innovation is the field of organic-inorganic charge transfer. Charge transfer across organic-inorganic interfaces is a crucial materials problem as the desire for added functionality and reduced cost pushes the field onward. These include applications in solar energy harvesting,[24–26] photo- and electro-catalysis,[27,28] and molecular electronics and sensing applications.[29, 30] Within the field of organic-inorganic interfacial charge transfer the rapid development and integration of electronically active small molecules has provided the opportunity for innovation at materials interfaces as well providing a model system for the study of interfacial charge transfer.

Molecular donors deposited on semiconducting oxides such as TiO_2,[31–33] ZnO,[34] and SnO_2,[35] can inject electrons into the oxide from their metal-to-ligand charge transfer excited state on the picosecond timescale.[31–34] Molecular monolayers and thin films exhibit variation in molecular orientation, conformation, and binding motif, as well as macroscopic parameters including thickness, roughness, packing density, and aggregation, all of which can affect the charge transfer rates. Charge transfer occurs through conjugated links or through-space tunneling and depends on factors such as the composition and structure of the chromophore and the anchoring group, the extent of conjugation of the molecular bridge group, and macroscopic structural factors such as the packing density and the aggregation state.[31,33,36,37] In this context,

Re-bipyridine complexes have been extensively studied as photoabsorbers and electron donors.[33, 38, 39]

Molecular level control of the structure offers exciting opportunities as a result of the strong dependence of interfacial charge transfer in donor-semiconductor systems on the structural parameters of the interface. These include structural factors such as the chemical structure of the donor molecules, the binding motif of the molecules on the surface, the aggregation state of the molecules, and in particular the conformation and orientation of molecules on the surface. In one example, as the distance between the charge transfer center of the molecule and the semiconducting substrate increased by increasing the length of the bridge group from 0 CH_2 spacers to 3 CH_2 spacers, the electron injection time increased from < 100 fs, to 240 ps.[31] This increase in electron injection time resulted from the reduction in electronic coupling between the donor and semiconductor.[31] Further investigation showed that depending on if the bridge group is conjugated or isolating, the charge transfer rate and mechanism is modified, with the latter showing that the charge injection rates decay exponentially with the distance between the donor center and the acceptor.[33] Even conformational fluctuations of a single molecule on the surface are predicted to change the electronic coupling resulting in a difference in the charge transfer rate by a factor of 14.[36]

This donor-surface distance can be manipulated through the incorporation of a reconfigurable group which changes the distance between donor and substrate in response to an external stimulus.[33,36,37] For example, pentacene FETs incorporating an azobenzene-containing monolayer at gate insulator/semiconductor interface exhibit a reversible variation of the threshold voltage with illumination.[40] The azobenzene-containing molecules change from trans-to-cis conformation upon illumination, shifting the threshold voltage of the FET due to

changes in the molecular dipole moment. It is possible to imagine systems where the structural state can be switched or reconfigured using an external stimulus such as optical stimulation, electric field modulation, or temperature changes. It would then be possible to drive the structural state through molecular height and conformation oscillations, through order-disorder transitions, to modify the aggregation state of the molecular systems, to have a built in, controllable electric field and polarization, or even to have long range, switchable molecular ordering. With this dynamic structural control, it would be possible to investigate the structural influence on interfacial phenomena such as the charge transfer dynamics, electronic and vibrational structure of the interface, dipole moments, and to correlate the timings of these transitions. The challenge has been to fabricate reconfigurable interfaces with a specific structure and to correlate the corresponding electronic kinetics systematically.

Reconfigurability can be introduced into organic/inorganic interfaces by assembling molecules containing azo-groups at interfaces.[1–3, 41] The azo group switches from *trans* to *cis* configuration following electronic excitation by a photon resonant with the π to π* transition at a wavelength of 320 to 350 nm. The *cis*-to-*trans* transformation can be induced by exciting the *n* to π* transition via the absorption of blue light at a wavelength of 400-450 nm.[4] In solution, the azobenzene molecule reconfigures on a 10 ps timescale.[42,43] Thermal isomerization back to the thermodynamically stable *trans* state occurs much more slowly, on the order of milliseconds to days depending on the stability and steric bulk of the other constituents of the azobenzene-containing molecule.[4] The timescale on which the *trans* to *cis* ratio in an ensemble changes is often much longer due to the different probabilities of the elementary isomerization processes. This change in the ensemble ratio of *trans* and *cis* isomers has commonly been observed to be on the timescale of seconds.[5,44] The photoisomerization leads to changes in the

molecular conformation, from the planar, elongated *trans* isomer to the compact three-dimensional *cis* isomer, which is accompanied by a change in the dipole moment, a decrease in the intensity of π to π* peak and an increase in the intensity of the n to π* peak in the absorption spectra.[4]

Photoisomerization in these monolayer systems is characterized by a variety of structural phenomena. Photoisomerization in azobenzene monolayers is often hindered by steric constraints. Steric hindrance and the restricted free volume available due to dense molecular packing limit the photoisomerization rates of azobenzene monolayers, prolonging the timescale of the initial reconfiguration to the order of seconds.[2,44–46] In self-assembled azobenzene monolayers with 100% coverage, vibrational sum-frequency generation measurements have observed no evidence for photoisomerization, despite the observation of photoisomerization at sub-monolayer coverages.[45] Additional insight into the role of mesoscopic effects is observed in scanning tunneling microscopy (STM) experiments, which show that chains with widths of a few molecules and lengths of 20 to 300 Å photoisomerize more slowly under UV radiation than their isolated counterparts and exhibit concerted switching.[2] The concerted switching phenomenon observed using STM was described as arising from intermolecular electronic coupling due to enhanced π-orbital overlap of the neighboring azobenzene groups.[2] These previous experimental results offer insight into the behavior of localized and isolated sets of molecules, but do not describe the behavior of complete monolayers.

In azobenzene monolayers, a dependence on the fraction of the monolayer composed of azobenzene molecules and hence the available free volume is commonly observed.[2,45,47] When the azobenzene group is given sufficient free volume and electronically decoupled from the surface, the switching behavior follows that of free molecules in solution.[46] When molecules are

deposited on spherical nanoparticles, the free volume is also increased leading to higher isomerized fractions.[47] Systematic STM studies show that the isomerization is reduced as the monolayer structure goes from individual molecules to 1-D and 2D chains.[2] In some cases, monolayers of 100% azobenzene molecules show no evidence of photoisomerization, but the photoisomerization rates increase with decreasing azobenzene fraction in the monolayer.[45]

Traditional techniques for probing the static structure of molecular monolayers include techniques such as Atomic Force Microscopy (AFM),[48,49] X-Ray Photoemission Spectroscopy (XPS),[48,50,51] or STM.[2] AFM provides information on the surface of the molecular monolayer in an area of 100s of square microns, providing limited information about the surface coverage, roughness and thickness of the molecular monolayer. Similarly, XPS provides information on the surface coverage on the monolayer. Dynamic measurements of the reconfiguration in these azobenzene system are carried out through measurements with electronic or vibrational spectroscopic indicators. These results reveal the impact of free volume in the photoisomerization as well as the timescale on which macroscopic restructuring of the monolayer occurs, which is on the order of 100s of seconds. However, these techniques are unable to address more subtle, but important structural questions such as the molecular conformation, orientation, and packing of the monolayer.

Additionally, dynamic measurements using spectroscopic indicators provide little clear information regarding the structural reconfiguration of the monolayer including the evolution of structure of isomerically mixed monolayers. In particular, direct structural observation of the change in conformation and height of the molecular monolayer has not been accomplished.[44, 46] This characterization challenge in evaluating the structure of monolayers fails to answer important structural questions about the structure evolves with optical exposure and how the

evolution rate and mechanism depend on the illumination conditions. Additionally, it is unable to provide clear insight into the timescale over which the reconfiguration occurs and the stability of the reconfigured states.

Inspired by these structure-property relationships, an initial work probes the connection between molecular design, the deposition technique, and the resulting interfacial structure. The interfacial structure and hence its properties can be controlled through the synthesis technique used to fabricate them, the molecular design of the organic component, and the resultant interfacial structure. A series of previous studies have demonstrated the importance of the static structural properties of interfaces in organic/inorganic electronic materials.[36, 37, 52] A degree of control can be obtained by using deposition techniques which offer greater control over the static structure than traditional solution deposition methods. One such approach is the Langmuir-Blodgett (LB) technique which organizes organic layers on the surface of liquid and compresses them into a tightly packed and semi-ordered film. Additionally, the design of the molecules themselves play a critical role in determining the final structure and degree of heterogeneity in the film. Molecules with molecular bridge groups of different rigidity are studied by X-ray reflectivity (XRR). The results showed that molecules pack more or less efficiently depending on the nature of the bridge group.

In an extension of the initial work, the synthesis of a novel photoisomerizable donor (ReAzoC) molecule (Figure 4-1) and a study of its assembly and reconfiguration on oxide surfaces was carried out. Structural characterization shows that LB assembly yields a monolayer structure with the rhenium bipyridine complex as the head group and with carboxylic acid anchor to the substrate, as in Figure 4-1(b). The molecules show spectroscopic evidence of photoisomerization in solution and as deposited in a monolayer. The structure is thus further

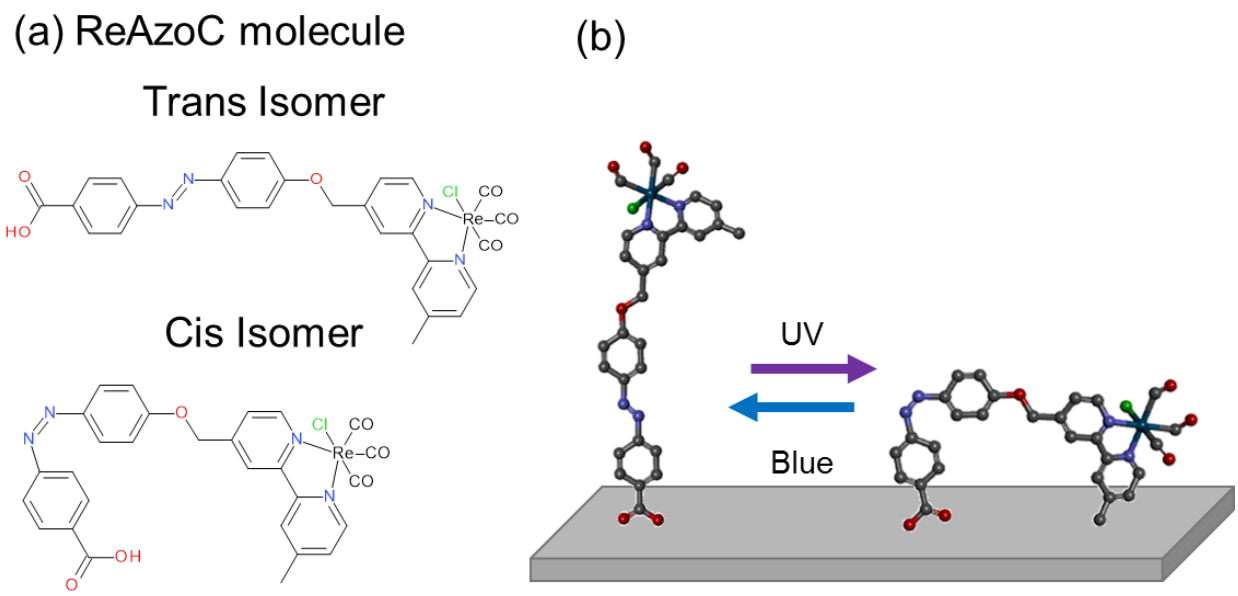

Figure 4-1: (a) Molecular structure of the ReAzoC molecule in trans and cis isomers. The ReAzoC molecule is composed of a 2,2' Re-bipyridine complex head group, an azobenzene bridge group, and a carboxylic acid attachment group. (b) Under UV and blue light the azobenzene group reversibly photoisomerizes from trans to cis (UV) and cis to trans (blue), respectively.

tunable using the *trans* to *cis* photoisomerization of the azobenzene group. Additionally, LB assembly can be reproducibly used to create monolayers with a series of different molecular coverage by varying surface pressure and an optimized single monolayer when deposited at the correct conditions.

The order resulting from this simple deposition process permits more precise structural characterization of the molecular reconfiguration than has been possible in the past. The incorporation of the Re metal complex in the monolayer increases the electron density contrast, enabling precise XRR studies of the mechanisms of structural reconfiguration. XRR quantitatively characterizes the structure and structural changes in large areas of complete monolayers with sensitivity to in-plane structural roughness at the 100 nm lateral length scale and the molecular configuration at the Angstrom scale. The XRR studies reported in this thesis

characterize the degree of order within the monolayer, the orientation of molecules on the surface, the isomerization state, and the evolution of the structure under optical exposure.

The combination of structural and spectroscopic characterization studies described in the remainder of the chapter show that ReAzoC can be organized into a closely-packed complete monolayer. Optical absorption measurements indicate that 13-15% of the molecules on the surface can be reversibly optically driven between structural states by illumination with alternating UV and blue illumination and that larger fractions of up to 47-52% can be irreversibly transformed at high optical power. X-ray and optical spectroscopy provide independent and consistent estimates of the fraction of isomerized molecules and the resulting monolayer structure. At low optical power, a small fraction of molecules isomerize in a spatially random distribution. At higher optical powers, where optical absorption indicates that UV light isomerizes approximately 50% of molecules there is an inhibition of the *cis*-to-*trans* reverse photoisomerization. XRR measurements show that the mean height of the donor groups within the monolayer is reproducibly changed as a result of the *trans*-to-*cis* isomerization.

When the reflected x-ray intensity of the sample is monitored during optical illumination, the fraction of the monolayer isomerized as a function of total photon dose and photon flux are monitored to complete the structural model for monolayer reconfiguration. These dynamic measurements show that the isomerized fraction of the monolayer depends on the total photon dose incident on the sample, rather than the photon rate. This suggests that monolayer structure evolves through the growth of large *cis* isomeric domains which grow through a nucleation and growth mode via cooperative switching.

4.2 Molecular monolayers on oxide surfaces

Portions of this section were adapted with permission from Joo et al., Langmuir **30, 6104-6113 (2014). Copyright (2014) by the American Chemical Society*

The molecular synthesis of the ReEC and Re2TC molecules were developed and carried out by Yongho Joo and Padma Gopalan. The use of Langmuir-Blodgett deposition to deposit monolayers, AFM, and XPS characterization and associated analysis were carried out by Yongho Joo and Padma Gopalan. The discussion of these results is included to frame and compare with the x-ray analysis.

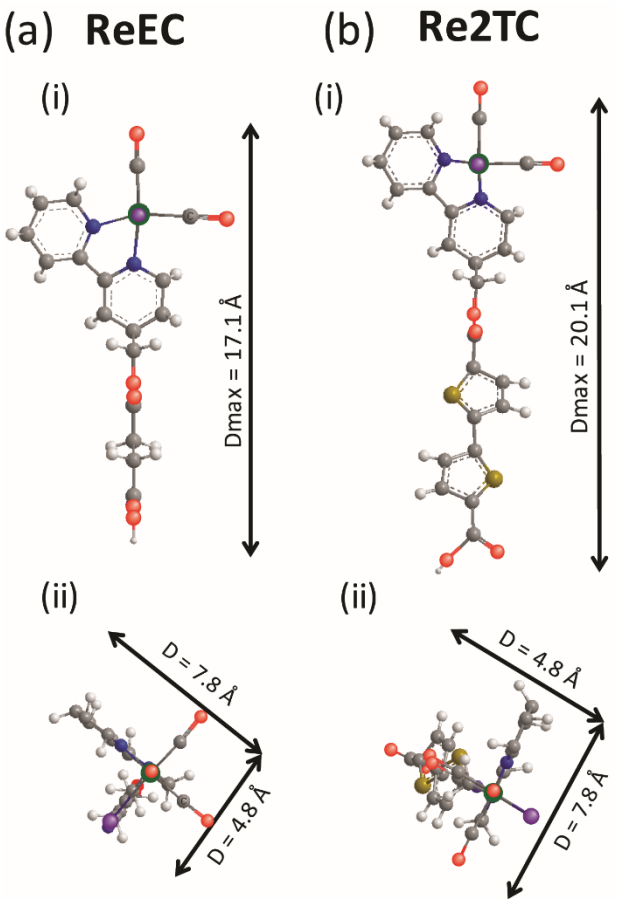

Figure 4-2: Molecular models for the (a ReEC and (b) Re2TC molecules. (carbon is gray, chlorine is purple, rhenium is green, hydrogen is white, oxygen is red, nitrogen is blue, and sulfur is yellow) (i) denotes the out-of-plane dimensions while (ii) denotes the in-plane dimensions for each molecule.

The creation of molecular monolayers with tunable heterogeneity offers many advantages over solution deposition techniques for fundamental studies and applications. Through the use of Langmuir-Blodgett (LB) technique the surface packing density of molecules at the interface can be controlled through the surface deposition pressure used to organize the monolayer. Langmuir-Blodgett technique works by assembling amphiphilic molecules at the water – air interface, with the hydrophilic end on the water side and the hydrophobic end on the air side. The molecules on the surface of the water are then compressed using an LB trough to a given surface pressure or mean molecular area. This allows tuning of the structure from sub-monolayer to single monolayer coverages.

Monolayers of metal-bipyridine complexes were deposited via Langmuir Blodgett technique on SiO_2 substrates, either the silicon native oxide or fused quartz slides. The molecules consist of a rhenium-bipyridine complex donor group, a molecular bridge group and a carboxylic acid anchoring group. The bridge group, which connects the donor/head group and the anchoring group, is either an aliphatic chain (ReEC) or a bithiophene (Re2TC), as shown in Figure 4-2. The molecules form stable LB films the air-water interface when dispersed in solution. It should be noted that these dyes don't fall into the truly amphiphilic class of molecules because the head group is polar with partial positive charge on the nitrogen atoms of the bipyridine complex and negative charges on the chloride ligand. However, the carboxylic acid group is relatively more hydrophilic, hence the bipyridine complex orients away from the water and carboxylic acid anchors the molecule in the water sub-phase. The key difference between the ReEC and Re2TC molecules is the change in the bridge structure from aliphatic to aromatic. This change modifies the driving force for packing by altering the cohesive and

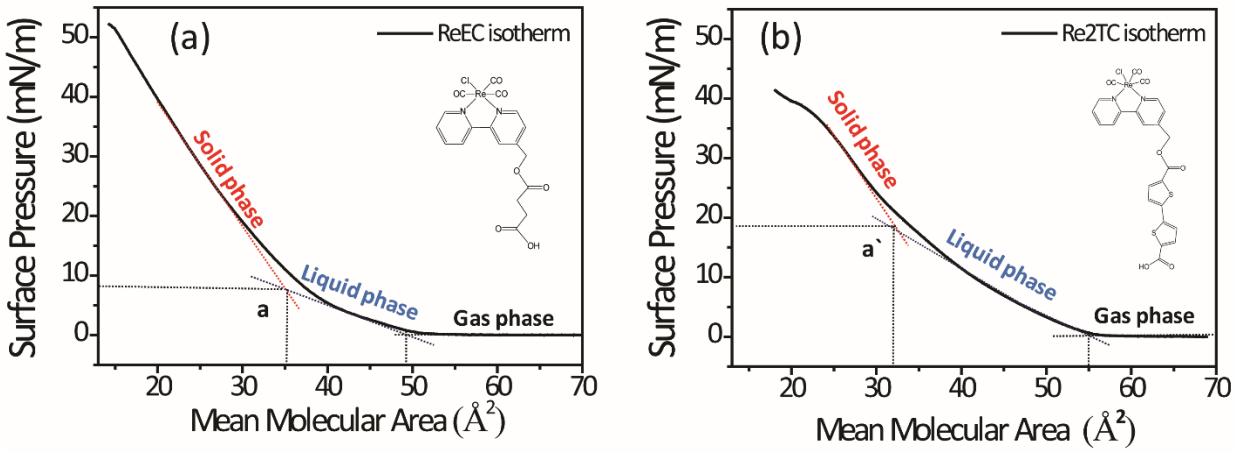

Figure 4-3: Surface pressure isotherms for (a) ReEC and (b) Re2TC spread from chloroform solution with a concentration of 1.0 mg/mL. A compression rate of 10 mm/min was used at a temperature of 23°C ± 1°C. These LB isotherms were collected by Yongho Joo.

repulsive forces between the donor molecules and the stiffness of the molecule, and hence the characteristics of the surface pressure isotherms.

The first step in depositing monolayers of ReEC and Re2TC was to determine the LB isotherms for each of the molecules, shown in Figure 4-3. The isotherms relate the measured mean molecular area occupied by each molecule to the deposition surface pressure used. By looking for inflection points in the isotherm, designated a and a' in Figure 4-3, the optimum conditions for depositing a single, closely packed monolayer were determined. The points (a) and (a') were defined as the points of intersection of the slopes of the liquid and solid phase region of the isotherm.

For ReEC, the surface pressure needed to deposit a single, closely packed monolayer was determined to be 10 mN/m, while the needed surface pressure for Re2TC was determined to be 20 mN/m. These correspond to a mean molecular area of 35 $Å^2$ for ReEC and 32.2 $Å^2$ for Re2TC, which are both in good agreement with the cross sectional areas shown in Figure 4-2. AFM and ellipsometry results confirm the presence of a single smooth monolayer for films of

ReEC and Re2TC deposited at these surface pressures. Upon further compression beyond the points (a) and (a`), the surface pressure increases sharply. Both ReEC and Re2TC molecules start to aggregate and form disordered multilayers, as shown by AFM, as the mean molecular area goes below the cross-sectional area of molecules. Films deposited with surface pressures below (a) and (a') show sub monolayer coverage, supported with AFM observations.

The surface coverage of the optimized monolayers was also characterized by XPS. Surface coverage is defined as the number of molecules per a unit area on the surface. From the XPS data the concentration of ReEC molecules in films transferred at 10 mN/m SP was 1.84 molecules/nm^2. This value is close complete single monolayer coverage. The estimated cross sectional area of the vertically oriented ReEC molecule on the substrate is ~ 0.4 nm^2. These estimated dimensions give a theoretical maximum coverage of ~2 molecules/nm^2 for a monolayer. For Re2TC, the surface coverage calculated from XPS was 2.27 molecules/nm^2 at 20 mN/m SP. The higher surface coverage for Re2TC compared to ReEC correlates with the observations in the isotherm curve where higher pressures were required due to the rigid nature of the thiophene bridge and the extended liquid phase regime.

XRR studies were conducted to obtain insight into the structural ordering of molecules on the interfaces. XRR measurements were performed with a Panalytical X'Pert MRD in a forward scattering geometry. XRR characterization was performed using monolayers deposited on silicon substrates. The ReEC and Re2TC films were deposited using surface pressures of 10 mN/m and 20 mN/m, respectively. The electron density profile of these monolayers were estimated using functional form of the electron density assuming a box model and the graded interface model for interface roughness (Figure 4-4). A schematic of the box structure for Re2TC is shown in Figure 4-4 (a). For the box model, the molecule was partitioned into two

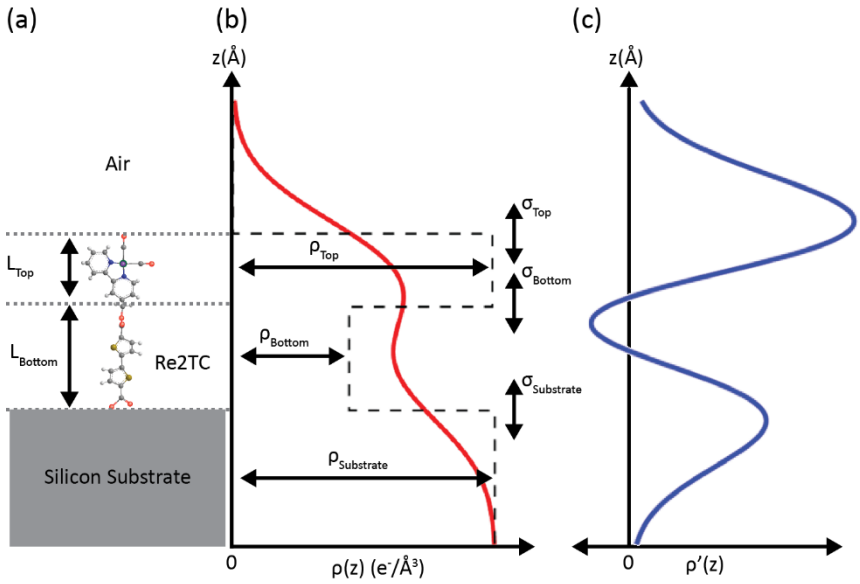

Figure 4-4: (a) Schematic of the box model of Re2TC used for fitting the experimental data. A Re2TC molecule is shown schematically on a silicon substrate. To partition the molecule into boxes, the molecule is split at the bond between the Re-complex and the bridge. (b) Example of the electron density as a function of position along the molecule, as approximated by the box model. The dashed black curve is a schematic of the electron density for the example case of perfect interfaces. The red curve is a schematic of the electron density for the example case of interfaces with a RMS roughness of 6 Å similar to the experimental results. (c) Gradient of the electron density as a function of position along the molecule for the case of RMS roughness at each interface of 6 Å.

boxes as shown in Figure 4-4 (b). The top box consists of the rhenium complex and the bottom box of the molecular bridge group. Each box is characterized by its thickness L and its electron density ρ.

The box thickness L (Å) was estimated by splitting the molecule at the bond between the Re-complex and the bridge group and taking the corresponding fraction of the calculated maximum length of the molecule. The electron density ρ ($e^-/Å^3$) was estimated by counting the number of electrons in each box and dividing it by the volume of each box with the calculated lateral dimensions and thicknesses. The molecular model parameters for ReEC are L_{Top} = 8.3 Å, L_{Bottom} = 8.8 Å, ρ_{Top} = 0.692 $e^-/Å^3$, ρ_{Bottom} = 0.203 $e^-/Å^3$, and $\rho_{Substrate}$ = 0.699 $e^-/Å^3$. The model parameters for Re2TC are L_{Top} = 8.3 Å, L_{Bottom} = 11.8 Å, ρ_{Top} = 0.692 $e^-/Å^3$, ρ_{Bottom} = 0.310 $e^-/Å^3$,

and $\rho_{Substrate}$ = 0.699 $e^-/Å^3$. The RMS roughness of each interface σ_j is determined during the fitting process. A schematic of this model for the electron density is shown in Figure 4-4 (b) for the example cases of perfect interfaces (dashed black lines) and for interfaces with 6 Å roughness (red curve). The corresponding gradient in electron density, $\frac{d\rho(z)}{dz}$, for the example case of 6 Å roughness is shown in blue in Figure 4-4 (c).

The simulation was fit to the experimental data by taking the common logarithm of the experimental and simulated intensity and minimizing the least squares fitting. The reflectivity data from ReEC and Re2TC samples deposited using surface pressures of 10 mN/m and 20 mN/m, respectively, are shown in Figure 4-5. The intensity is shown normalized to the incident beam intensity. The high intensity points at Q < 0.01 $Å^{-1}$ arise because a portion of the direct beam is incident on the detector at small angles. The local minimum and increase in intensity from 0.01 $Å^{-1}$ < Q < 0.03 $Å^{-1}$ (Q_c = 0.0314 $Å^{-1}$) results from changes in the beam footprint with increasing incident angle. As the incident angle increases, a larger fraction of the beam footprint is occupied by the sample, resulting in an increase in the reflected intensity. The broad feature observed at 0.2 $Å^{-1}$ for ReEC and Re2TC films, arises from reflection from the film. Using the

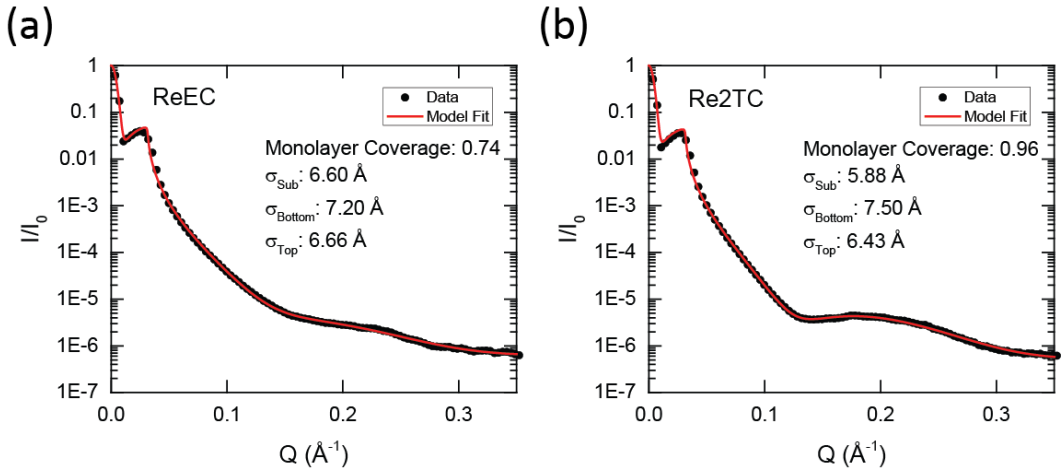

Figure 4-5: XRR data from ReEC (a) and Re2TC (b) samples. The data are fit assuming constant layer thickness and electron density values as derived from the box model. The data are fit by varying monolayer coverage and interface roughnesses.

model parameters described above, the data was fit using seven parameters: incident beam intensity I_0, the width of the direct beam set by the detector σ_{DB}, the percentage of the signal arising from the respective molecule x, the RMS roughness of each of the three interfaces σ_j, and the background intensity $I_{Background}$. The layer thicknesses and electron densities are not fit and assume the values determined from the box model. The best fit parameters for each data set are inset in the plot.

Figure 4-5 shows reflectivity data from a ReEC film (a) and a Re2TC film (b). The fit values for the percentage of signal arising from the monolayer covered substrate is 0.74 and 0.96, respectively. For the ReEC film, $\sigma_{Top} = 6.66$ Å, $\sigma_{Bottom} = 7.20$ Å, and $\sigma_{Sub} = 6.60$ Å. For the Re2TC film, $\sigma_{Top} = 6.43$ Å, $\sigma_{Bottom} = 7.50$ Å, and $\sigma_{Sub} = 5.88$ Å. For reference, $\sigma_{Sub} = 6.38$ Å for a bare silicon substrate.

The XRR data confirms the presence of a well-ordered monolayer on the surface. The ability to fit the data without adjusting the length and electron density parameters suggests that the molecules are extended close to their calculated maximum length and are oriented with the long axis of the molecule more or less normal to the substrate. The roughness values determined by the fitting process suggest that the roughness of the substrate is translated to the film. The higher percentage of signal arising from the monolayer for Re2TC agrees the higher surface coverage values extracted from the XPS results and indicates a better packing conformation for the Re2TC sample. The higher coverage observed using XPS and XRR for Re2TC support the hypothesis that the higher rigidity of the Re2TC molecular bridge allows Re2TC to form more stable and well-ordered monolayers.

4.3 Structurally reconfigurable organic-inorganic monolayer interfaces

Portions of this section were adapted with permission from McElhinny et al., Langmuir **39, 2157-2168 (2017). Copyright (2017) by the American Chemical Society.*

The molecular synthesis of the ReAzoC molecule was developed and carried out by Peishen Huang, Catherine Kanimozhi working in the research group of Padma Gopalan at the University of Wisconsin - Madison. The use of Langmuir-Blodgett deposition to deposit monolayers, AFM, and XPS characterization and associated analysis were carried out by Yongho Joo and Padma Gopalan. The discussion of these results is included to frame and complete the model developed in conjunction with the x-ray analysis.

4.3.1 ReAzoC synthesis and monolayer static structure

For this work, unique azo-based chromophore ReAzoC that contains three moieties relevant to the XRR studies was designed. The head group containing the bipyridine group can complex with transition metal ions to increase the electron density contrast and hence the x-ray scattering cross section. The middle unit of the molecule contains the photo-switchable azo group which is used to reconfigure the monolayer by photo-isomerization from *trans* to the *cis* form. The tail group of the molecule is a polar carboxylic acid group which anchors the molecule at the water sub-phase during assembly and subsequently to the oxide substrate.

The rhenium bipyridine group is chosen as it has a metal-to-ligand charge transfer state which is aligned with the conduction band of semiconducting oxides like TiO_2. Similar molecules containing Re-bipyridine groups have a singlet MLCT state with an energy of ~ 1 eV above the bottom of the TiO_2 conduction band.[33] In these donor-semiconductor systems the rate of electron injection increases with the increasing energy difference between adsorbate excited state and the conduction band edge.[53] The azobenzene group is incorporated to allow reconfiguration of the molecular conformation through optical exposure to uv (*trans* to *cis*) or blue (*cis* to *trans*) illumination. The reconfiguration from the *trans* to the *cis* state is expected to

change the distance between the Re-bipyridine group and the donor surface by ~ 1 nm. The carboxylic acid attachment chemistry to attach the molecules to the oxide substrate. Carboxylic acid chemistries have strong binding to oxide substrates and using a single carboxylic acid reduces the number of binding modes available in comparison to two mode systems, hence reducing the structural variation within the monolayer.

The LB method is typically used to assemble amphiphilic molecules such as lipids at the air-water interface and transferring the ordered monolayer on to a substrate. LB characterization and deposition experiments were performed using a LB trough (KSV KIMA Medium size KN2002, Helsinki, Finland). The surface pressure-area (π-A) isotherm of donor molecules molecule was measured with a Wilhelmy balance (Pt plate). The water subphase was treated to have a resistivity of 18.2 MΩ cm by a Milli-Q water filtration station (Millipore, Inc.). The molecular layers were transferred to the solid substrates using the LB dipping technique at a set surface pressure. A ReAzoC solution with a concentration of 200 μL of (1 mg/mL $CHCl_3$:THF=9:1) was used. The solvent was allowed to evaporate for 30 min before compression of the monolayer. A drop cast film was prepared for comparison by dropping ReAzoC solution (1mg/mL $CHCl_3$:THF=9:1) onto a Si substrate prepared via the piranha treatment and allowing it to evaporate for 24 h in vacuum.

Quartz substrates were obtained from Structure Probe, Inc. under the trade name SPI SuperSmooth Quartz Slides. The manufacturer's specification for RMS roughness of these quartz slides is less than 0.5 nm. Minimizing substrate roughness maximizes the quality of XRR data can be achieved through both improvements in the vertical alignment of electron rich

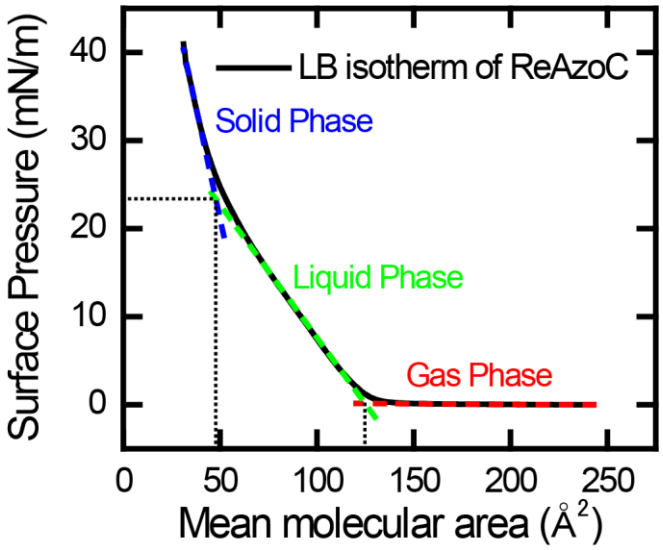

Figure 4-6: Surface pressure-mean molecular area isotherm of ReAzoC spread from chloroform and THF (9:1) with concentration 1.0 mg/mL. Regions of gas, liquid, and solid phase are defined by slope discontinuities at 125 Å^2 and 50 Å^2.

portion of molecule and a reduction in interfacial roughness. Si/SiO_2 substrates were purchased from Montco Silicon Technologies. The Si/SiO_2 and quartz substrates were cleaned by the piranha process (7:3 H_2SO_4:H_2O_2) at 90°C for 30 min and rinsed with DI water.

Although not truly amphiphilic, the ReAzoC molecule has a more polar carboxylic acid tail group which makes it a good candidate for stabilization at air/water interface and to preferentially interact with oxide substrates.[48] For LB monolayer deposition, ReAzoC was spread on the water subphase. After complete solvent evaporation, a surface pressure-mean molecular area isotherm was recorded at 20 °C with a compression speed of 10 mm/min (Figure 4-6). The isotherm in Figure 4-6 exhibits three distinct phases: gas, liquid, and solid, each separated by discontinuities in the slope of the pressure-area curve. For the isotherm of ReAzoC donor molecules, the transition from a two-dimensional gas to liquid phase and from liquid to solid phase occurs at a mean molecular area of 125 Å^2 and 50 Å^2, respectively, as shown in Figure 4-6. Based on bond angles and bond lengths given by Dominey *et al.*,[54] the *trans* state of

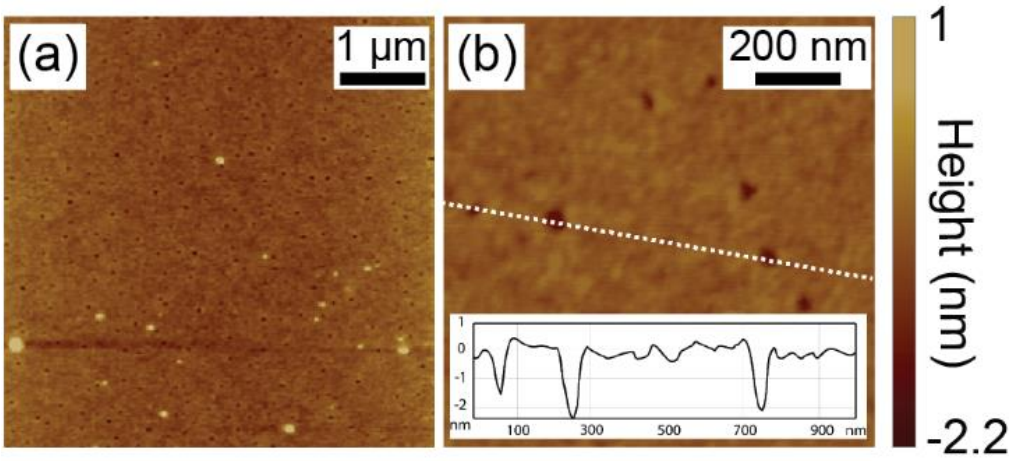

Figure 4-7: AFM characterization of a monolayer of ReAzoC donor molecules deposited at 25 mN/m surface pressure. (a) 5 µm x 5 µm and (b) 1 µm x 1 µm regions. The inset in (b) shows a height line profile taken along the dashed line. The height difference between the molecular layer and substrate in the line profile is 2.3 nm.

the molecule theoretically occupies an area of 37.44 $Å^2$. The 50 $Å^2$ mean molecular area observed at a surface pressure of 25 mN/m is thus close to the theoretical cross-sectional area of ReAzoC in the thermodynamically favored *trans* conformation. The pressure-area curve suggests that transferring a monolayer of ReAzoC to a solid substrate at the transition point between the solid and liquid phases in the isotherm produces the most densely packed single monolayer which can be deposited. This hypothesis is supported below by detailed XPS characterization.

AFM images of monolayers transferred from the LB trough to a substrate at a surface pressure of 25 mN/m are shown in Figure 4-7. The surface morphology of the monolayers of ReAzoC molecules was imaged using a Nanoscope III Multimode atomic force microscope (Digital Instruments). A non-contact imaging mode was used for the AFM measurement. A triangular cantilever with an integral pyramidal Si_3N_4 tip was used. The typical imaging force was on the order of 1 nN. The thickness of the monolayer was determined using line profiles through pinholes in the film. AFM images in Figure 4-7 (a) exhibit low RMS surface roughness

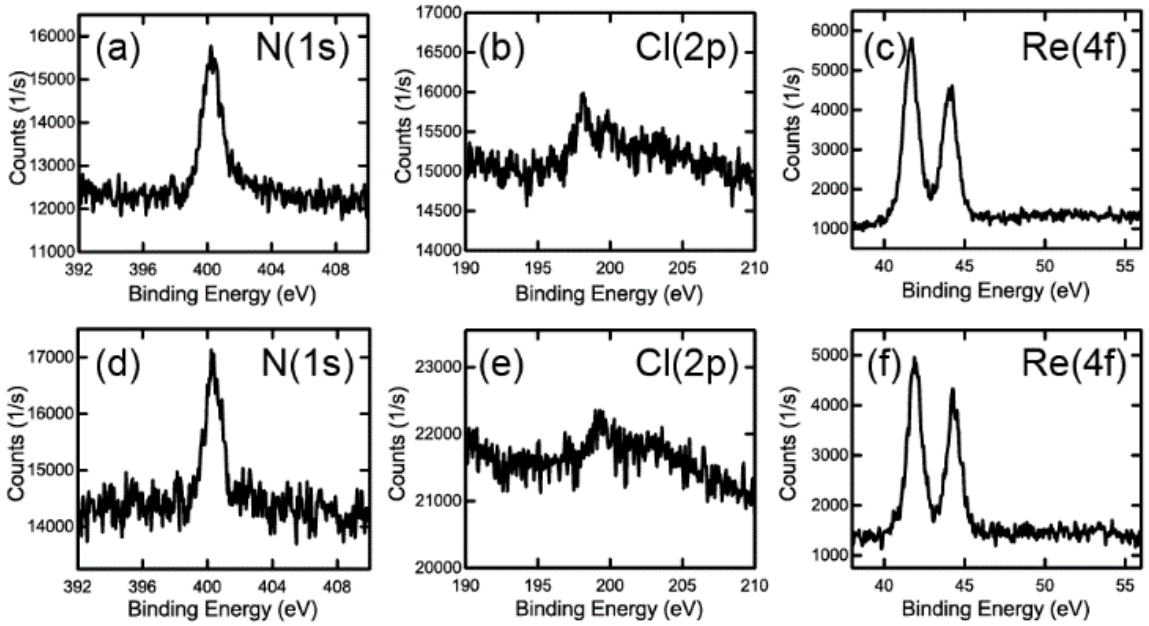

Figure 4-8: XPS spectra of ReAzoC (a)-(c) an LB film transferred at a surface pressure of 25 mN/m to Si and (d)-(f) a drop-cast film on Si.

of 0.218 nm, far less than the total thickness of the molecule. The holes evident in Figure 4-7(a) and (b) allow the thickness of the film to be measured. The height profile inset in Figure 4-7 (b) shows a height difference of 2.3 nm between the top and bottom of the monolayer, which corresponds to the height of the ReAzoC molecule. This height is predicted to be 2.4 nm based on the bonding configurations given in ref. 54.

The surface concentration of ReAzoC molecules within layers deposited at different surface pressures (5, 15, 25, and 40 mN/m) and via drop casting was measured by XPS. The drop cast film which is expected to be disordered was used as a comparison. A Thermo Scientific K-alpha XPS was used for compositional analysis of films deposited on Si/SiO_2 substrates. The XPS instrument used a microfocused monochromated Al Kα X-ray source with a spot size of 400 μm. A pass energy of 50 eV was used to collect survey spectra. Spectra were analyzed using the manufacturer's Avantage software and peak fitting with Gaussian/Lorentzian

peak shape and a Shirley/Smart baseline. The surface coverage, defined as the number of molecules per unit area on the substrate, was determined using:

$$N_x = \frac{A_x}{A_{Si}} \frac{S_{Si}}{S_x} \frac{\varphi_{Si,SiO_2} \lambda_{Si,SiO_2} Sin(\theta) e^{(t/\lambda_{x,organic} Sin\theta)}}{e^{(t/\lambda_{x,organic} Sin\theta)}}.$$

Equation 4-1

Here, N_x is number of atoms per unit area for element *x*, and A_x/A_M and S_m/S_x are the ratio of integrated peak areas for element *x*, and the ratio of the sensitivity factors of element *x* on the substrate Si, respectively. The factor φ_{Si,SiO_2} is the number of Si atoms per unit volume in SiO_2, and λ_{Si,SiO_2} is inelastic mean free path (IMFP) of Si photoelectrons in SiO_2. The layer thickness is *t*, and $\lambda_{x,organic}$ is the IMFP for the electrons emitted from element *x* in the molecular monolayer.

Table 4-1: Atomic coverage of ReAzoC on Si/SiO_2 substrate calculated from Cl(2p), N(1s), and Re(4f) peaks with Si(2p) peak as internal reference.

	Cl 2p (molecules/cm^2)	**N 1s (molecules/cm^2)**	**Re 4f (molecules/cm^2)**	**Average ReAzoC coverage[a] (molecules/nm^2)**
Drop cast film	Small S/N*	1.50×10^{14}	1.28×10^{14}	1.39
5 mN/m LB monolayer	Small S/N*	1.08×10^{14}	0.70×10^{14}	0.89
15 mN/m LB monolayer	Small S/N*	1.36×10^{14}	1.14×10^{14}	1.25
25 mN/m LB monolayer	1.46×10^{14}	2.58×10^{14}	1.85×10^{14}	1.84
40 mN/m LB monolayer	2.85×10^{14}	3.65×10^{14}	3.11×10^{14}	3.20

[a] Average of the atomic coverage of component elements.

* Signal to noise ratio obscures the Cl 2p peak, preventing surface coverage quantification.

The XPS data for N(1s), Cl(2p), and Re(4f) transitions for a monolayer transferred at 25 mN/m and a drop cast film are shown in Figure 4-8 (a) and (b), respectively. The N(1s) peak at

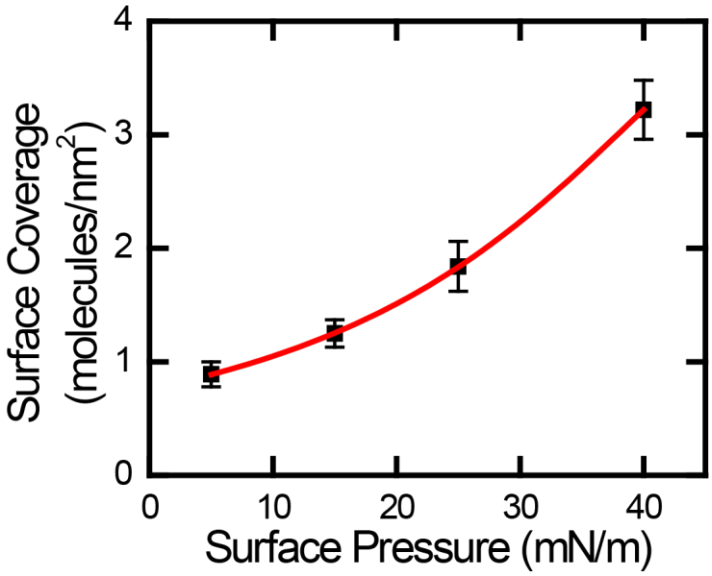

Figure 4-9: Surface coverage determined by XPS as a function of the surface pressure during LB deposition.

399-404 eV, Cl(2p) peak at 198-204 eV, and Re(4f) peaks at 41-49 eV together confirm that the ReAzoC molecules have been transferred to the substrate. The surface coverages calculated from the Cl(2p), Re(4f), and N(1s) peaks in the XPS spectrum are shown in Table 4-1**.**

The dependence of the molecular coverage on surface pressure is shown in Figure 4-9. The surface coverage of the ReAzoC molecules in LB films transferred at the optimum surface pressure of 25 mN/m was 1.84 molecules/nm^2. This is consistent with the estimate of 2 molecules/nm^2 from the LB isotherm (Figure 4-6). The theoretical maximum coverage of a single monolayer of ReAzoC is 2.7 molecules/nm^2, calculated from the molecular dimensions estimated based on Dominey *et al.*[54] When taken together the XPS spectra, AFM profile, and LB isotherm confirm the formation of an optimized ReAzoC monolayer at a surface pressure of 25 mN/m.

The *trans-cis* photoisomerization of ReAzoC thin films deposited on a transparent quartz substrate was monitored using UV-Vis transmission spectroscopy. UV-Vis absorption

measurements were performed in a transmission geometry in a wavelength range of 200 to 800 nm using a Shimadzu PC-2401 spectrometer. Two different light sources were used to photoisomerize the molecules. Prizmatix FC8-LEDs with wavelengths of 365 nm and 465 nm were used for the UV-Vis studies. Light emitting diode (LED) sources (Engin LZ1-00DB00 and LZ1-00UV00, with peak wavelengths of 460 nm and 365 nm, respectively) were employed for XRR studies and studies of sequential XRR measurements and optical exposures.

The absorption spectrum before irradiation (black curve, Figure 4-10 (a)) exhibits a strong peak at 360 nm arising from the π-π* electronic transition of *trans*-azobenzene. Absorption spectra for ReAzoC at a concentration of 2.74×10^{-6} M in a chloroform-THF (9:1) solution are shown in Figure 4-10 (b). Absorption spectra were acquired under ambient room light and the initial configuration thus consisted of a mixture of *trans* and *cis* states. The two absorption peaks at 244 nm and 285 nm arise from the π-π* transition of the rhenium bipyridine group.[55, 56]

Illumination of the transferred LB film at a wavelength of 365 nm LB film of ReAzoC leads to a decrease in the absorbance of the 360 nm absorption band, reaching a photostationary state after a 10 s exposure at 16.9 mW/cm^2 (Figure 4-10 (a)). The absorbance of the 360 nm peak recovered to its initial value after a 10 s exposure to 465 nm wavelength illumination at 9.5 mW/ cm^2. The photostationary state observed in the spectra of the thin film is consistent with observations in solution, as in Figure 4-10 (b). The change in the optical spectrum provides direct evidence for the *trans-cis* photoisomerization of both monolayer and solution forms of ReAzoC.

The absorption cross section was estimated using the UV-Vis spectra shown in Figure 4-10. In solution, the absorption cross section at 352 nm was 6.8×10^{-16} cm^2 for the *trans* isomer

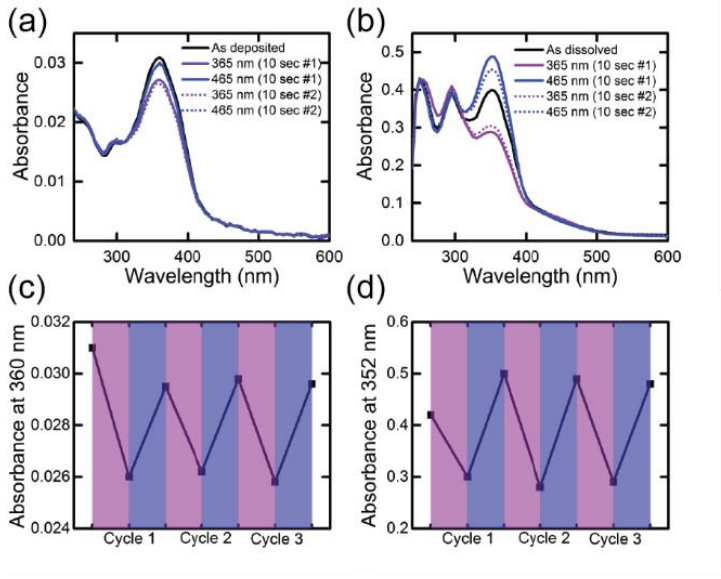

Figure 4-10: UV-Vis absorption spectra of ReAzoC for (a) a monolayer deposited using the LB method and (b) 2.74 $\times 10^{-6}$ M solution of ReAzoC in chloroform-THF (9:1). Reversible switching of the absorbance maximum of ReAzoC of (c) LB film and (d) solution after alternating cycles of UV (365 nm, 10 s) and blue (465 nm,10 s) irradiation.

and 4.0×10^{-16} cm^2 for the *cis* isomer. The absorption cross section of the molecular monolayer was 1.8×10^{-16} cm^2 for the *trans* isomer and 1.6×10^{-16} cm^2 for the *cis* isomer. The difference between the absorption cross section of ReAzoC in solution and the ReAzoC monolayer can be in part attributed to the anisotropic distribution of the molecular orientation in the monolayer. The transition dipole moment of the azobenzene π-π* transition is oriented approximately parallel to the long axis of the azobenzene group and is thus oriented nearly along the monolayer surface normal. The electric-field vector of the incident radiation is in a plane perpendicular to the surface normal under the normal-incidence conditions used for the UV-Vis measurements. The absorbance under these conditions is proportional to 3/2 $\mathrm{Sin}^2(\theta)$, where θ is the angle between the transition dipole moment of the azobenzene and the surface normal.[44] With the molecules oriented approximately normal to the surface as is the case in the ReAzoC monolayer, this factor serves to reduce the absorption in comparison to the solution. The absorption cross section of the π-π* transition in an azobenzene-containing monolayer can be estimated from

values given in ref. 46. With a correction based on the approximately 20% quantum yield of the reorientation transtition,[57] the total absorption cross section from ref. 46 is on the order of 3.5×10^{-17} cm^2. The peak position of π-π* transition in the LB monolayer was red-shifted by 8 nm relative to that in solution. The origin of this red-shift is unclear at this point. However multiple factors such as the tilt of the molecular orientation with respect to the surface normal, contributions to the maximum at 360 nm from the S2 π-π* transition in Re-bipyridine group,[33] and possible solvatochromic effects influencing the S2 transition may play a role.

The optical absorption spectra were used to estimate the fraction of molecules that undergo the *trans*-to-*cis* isomerization. The 360 nm absorption band has contributions from the absorbance of the azobenzene group in both the *cis* and *trans* isomer as well as a small contribution from the Re-bipyridine head group.[33] However, if this small contribution is neglected, an estimation of the lower limit for the fraction of molecules isomerized can be estimated by an extension of Beer's Law:

$$A = \varepsilon_{Trans} N_{Trans} + \varepsilon_{Cis} N_{Cis}$$

Equation 4-2

Here ε_n is the absorption constant for the isomer and N_n is the number of molecules of each isomer in the optical beam path, and $N_{Trans} + N_{Cis} = N_{Total}$. The absorption constants of the *trans* and cis isomer are related by a scalar *n*, the wavelength-dependent ratio of the *trans*-*cis* isomer absorption constants. Thus the absorbance of the peak can be rewritten as a function of a single isomer independent absorption constant.

$$A = n\varepsilon N_{Trans} + \varepsilon N_{Cis}$$

Equation 4-3

The fractional change in the absorbance can be related to the fraction of molecules isomerized by computing the fractional change $\frac{A-A'}{A}$, where *A* is the absorbance of the initial state and *A'* is the absorbance of the final state. With Equation 4-3 following expression for the fractional change in absorbance is determined:

$$\frac{A - A'}{A} = \frac{n\varepsilon\Delta N_{Trans} + \varepsilon\Delta N_{Cis}}{n\varepsilon N_{Trans} + \varepsilon N_{Cis}}$$

Equation 4-4

Here ΔN_{Trans} and ΔN_{Cis} are the differences between the number of molecules of the *trans* and *cis* state present in the initial and final states, respectively. Necessarily, $\Delta N_{Trans} = -\Delta N_{Cis} = \Delta N$, thus:

$$\frac{A - A'}{A} = \frac{(n-1)\Delta N}{nN_{Trans} + N_{Cis}}$$

Equation 4-5

Under the assumption that the initial state, before UV exposure can be reasonably approximated as consisting only of *trans* isomers, which is applicable because the *trans* state of the azobenzene group is the thermodynamically stable state. In this approximation, $N_{Trans} = N$ and $N_{Cis} = 0$ and equation (6) becomes:

$$\frac{\Delta N}{N} = \frac{n}{n-1}\frac{\Delta A}{A}$$

Equation 4-6

Literature values of *n* are between 5 and 10.[4, 58] The absorption spectra for ReAzoC molecules in solution (Figure 4-10 (b)) have $\frac{\Delta A}{A} = 40\%$, and thus between 44 and 50% of the molecules in solution are photoisomerized. When deposited as a monolayer (Figure 4-10 (a)),

$\frac{\Delta A}{A} = 12\%$, and thus only 13 to 15% of the molecules on the surface are photoisomerized by a UV intensity of 16.9 mW/cm^2. This limited photoisomerization is commonly observed in para-substituted azobenzenes as a result of very rapid thermal relaxation which makes the creation of large fractions of *cis* isomers difficult.[59]

The reversibility of the *trans-cis* photoisomerization of ReAzoC was characterized by alternating 10 s periods of illumination at wavelengths of 365 nm and 465 nm wavelength at optical intensities of 16.9 mW/cm^2 and 9.5 mW/cm^2, respectively. A decrease and recovery of the absorbance of the monolayer at 352 nm in solution and at 360 nm is evident in the summaries of the absorption peak heights after repeated exposures shown in Figure 4-10 (c) and (d). At low optical intensities the molecules in solution deposited in a monolayer undergo reversible photoisomerization.

4.3.2 X-ray reflectivity structural characterization

The fractional intensity of an incident x-ray beam reflected by a thin film on a substrate depends on the electron-density profile of the interface along the surface normal direction.[60–65] A model consisting of the substrate, the monolayer, and the ambient environment was used to interpret the XRR measurement. The model parameters are ρ_{Sub}, the electron density of the substrate, which is held constant, σ_{Sub} the roughness of the substrate-monolayer interface, and $L_{Monolayer}, \rho_{Monolayer}, \sigma_{Monolayer}$, which are the thickness, electron density and roughness of the monolayer-air interface, respectively. An initial point for the refinement of the reflectivity model was obtained by predicting the height using the distance along the long axis of the ReAzoC molecule from literature values of bond angles and bond lengths.[54] The initial electron density estimate was obtained by counting the number of electrons within the theoretical volume occupied by the molecule. Based on the model for the ReAzoC molecule, an ideally packed

monolayer of *trans* conformation molecules is expected to have an electron density of 0.396 $e^-/Å^3$, thickness 24 Å, and a substrate roughness near that of bare silicon. A corresponding monolayer of *cis* conformation molecules is expected to have an electron density of 0.521 $e^-/Å^3$ and a thickness of 8.45 Å. Additional geometric and experimental parameters such as sample width, beam width, and direct beam intensity are measured to allow the fit to match the measured intensity with no overall scaling parameter.

XRR measurements were performed at the University of Wisconsin-Madison and at the National Institute for Materials Science (NIMS), Tsukuba, Japan, in the research group of Dr. Kenji Sakurai. Measurements at NIMS used a custom-built x-ray reflectometer with an x-ray source operating at 1.6 kW producing Cu Kα radiation. The incident beam width measured using a knife edge was 42.6 μm. Measurements conducted at UW-Madison used a Panaltytical X'PERT MRD using Cu Kα radiation at a source power of 1.8 kW, for which the incident beam width was 220 μm. The analysis of the experimentally acquired XRR intensity distributions was conducted using the GenX software package.[66] The GenX package employs a curve fitting algorithm that adjusts values of the interface roughness, layer thickness, and density to optimize a figure of merit Log(R1):

$$Log(R1) = \frac{\sum_i \left[\left|\log_{10}\left(\sqrt{Y_i}\right) - \log_{10}\left(\sqrt{S_i}\right)\right|\right]}{\sum_i \left[\log_{10}\left(\sqrt{Y_i}\right)\right]}$$

Equation 4-7

where Y_i is the measured reflected intensity, S_i is the corresponding simulated value, and the sum spans the series of data points.

An XRR measurement of a ReAzoC monolayer deposited at a surface pressure of 25 mN/m is shown in Figure 4-11(a). The reflectivity curve for the 25 mN/m samples exhibits total external reflection at incident angles lower than $2\theta = 0.4°$ and a single broad reflectivity fringe, including an intensity minimum at $2\theta = 1.4°$ and a maximum at $2\theta = 1.8°$. Only one fringe is observed as a result of the small thickness of the monolayer and the limited dynamic range of the laboratory-based x-ray instrumentation. The reflectivity from a monolayer deposited at 15 mN/m, Figure 4-11 (b), shows a weak reflectivity fringe as seen by the changes in the curvature of reflected intensity near $2\theta = 1.5°$ and $2\theta = 2.25°$. The reflectivity signal from the drop-cast film, Figure 4-11 (c), and bare silicon, Figure 4-11 (d), do not exhibit interference fringes. The extracted electron density profiles for each sample are shown in the inset of the reflectivity curves. Fitting parameters for the XRR curves are summarized Table 4-2. For a monolayer deposited at a surface pressure of 25 mN/m, the substrate-monolayer roughness and electron density of the single layer agree with the theoretical model. The agreement between the fitting

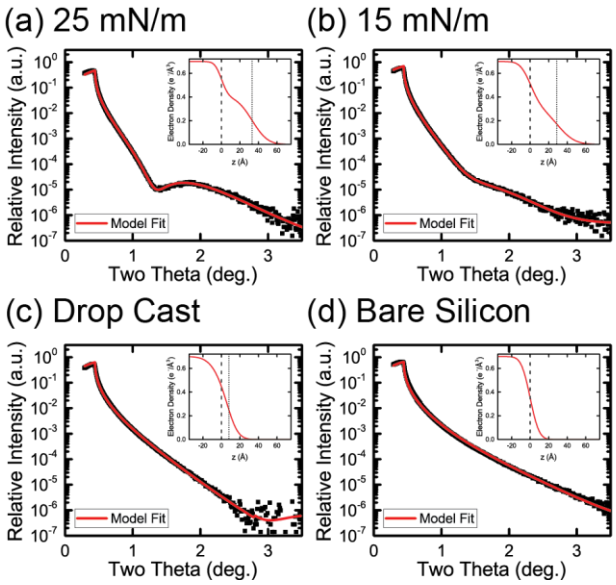

Figure 4-11: XRR of (a) ReAzoC monolayer deposited at surface pressure 25 mN/m, (b) ReAzoC monolayer deposited at surface pressure 15 mN/m, (c) drop-cast ReAzoC film, (d) bare Si/SiO_2 substrate. The red line shows the best fit using the model and parameters in Table 4-2. Insets show model electron density profiles.

parameters and the molecular model indicates that the monolayer is closely packed, with the molecules orientated and ordered with their long axis more or less normal to the surface.

A systematic XRR study of several samples shows small variations in the apparent monolayer thickness of films deposited under nominally identical deposition conditions. Thicknesses are consistent for samples in a single batch, but are different in different deposition events and substrates. The mean molecular thickness obtained by averaging the thicknesses measured for each sample is 29.6 Å with a standard deviation of 3.2 Å. A further difference between the predicted and measured heights can arise from the roughness of the substrate, which is nearly 1/3 the height of the molecule. The physical interpretation of the parameters of the XRR model is thus complicated by the relative magnitudes of the surface roughness and of the molecules.

Table 4-2: XRR fit parameters.

Sample	**Substrate-monolayer interface roughness (Å)**	**Monolayer thickness (Å)**	**Monolayer electron density ($e^-/Å^3$)**	**Monolayer-air interface roughness (Å)**
25 mN/m ReAzoC monolayer	5.9	33	0.41	13.2
15 mN/m ReAzoC monolayer	8.8	28.7	0.34	15.2
Drop cast ReAzoC monolayer	12.4	8	0.29	8.2
Si/SiO_2 substrate	7.6	N/A	N/A	N/A

An alternative to the single layer model is to conceptually split the molecule into two layers of different density with a boundary between the two layers placed at the ether group

connecting the head and the bridge groups. The result is a two-layer model with an electron rich head group with a density of 0.718 $e^-/Å^3$, 8.3 Å in thickness and an electron poor bridge and attachment group with a density of 0.226 $e^-/Å^3$, 15.7 Å in thickness. The substrate-air interface roughness of the silicon substrate, is fit to be 7.6 Å RMS. The interface can be modeled as a monolayer of molecules, assuming this two box model, conformally coating a rough silicon substrate. In this case, the out-of-plane electron density profile created by integrating the density along the in-plane direction appears to form a single layer with average density and increased thickness as a result of the comparable magnitudes of the molecular length and surface roughness and the comparable densities of the molecular head group and the Si substrate.

The XRR results exhibit a clear difference in the electron density profiles of samples deposited with different surface densities. The model fit of the monolayer deposited using a surface pressure of 15 mN/m deposited shows a reduction in magnitude of the thickness and electron density parameters. This reduction in the magnitude of the thickness and electron density is indicative of a reduced monolayer coverage with the fit parameters being a weighted average between the densities of the molecular monolayer and air. This weighted average interpretation is used to account for samples with sub monolayer coverage to account for the lack of lateral homogeneity. The reflectivity pattern is indicative of a surface with the molecules organized into closely packed islands due to the spatial constraint imposed by the lateral coherence length of x-rays. The weighted average model estimates the surface coverage for the 15 mN/m film to be 75% the value of the complete single monolayer, as compared to 68% as observed via XPS. This discrepancy arises from uncertainty in accounting for the interfacial roughness for the bare silicon and complete monolayer films used in the weighted average

model. Further reduction of those parameters in the case of the drop cast films is consistent with a randomly distributed array of molecules or the formation of three-dimensional aggregates.

4.3.3 X-ray reflectivity characterization of isomerization.

XRR provides insight into the structural changes, including changes in the thickness of the molecular layer, resulting from optical illumination. XRR studies of the reconfiguration were conducted using monolayers deposited at a surface pressure of 25 mN/m. The experimental procedure used for the structural studies of the reconfiguration process consisted of a series of alternating exposures to UV and blue light at wavelengths of 365 nm and 460 nm, respectively. The UV and blue optical intensities for this structural study were 94 mW/cm^2 and 100 mW/cm^2, respectively, far higher than the intensities used to obtain the optical spectra in Figure 4-10.

XRR measurements of the as-deposited structure are shown in Figure 4-12(a). Following this initial configuration, the monolayer was exposed to blue light for 30 s and the XRR curve

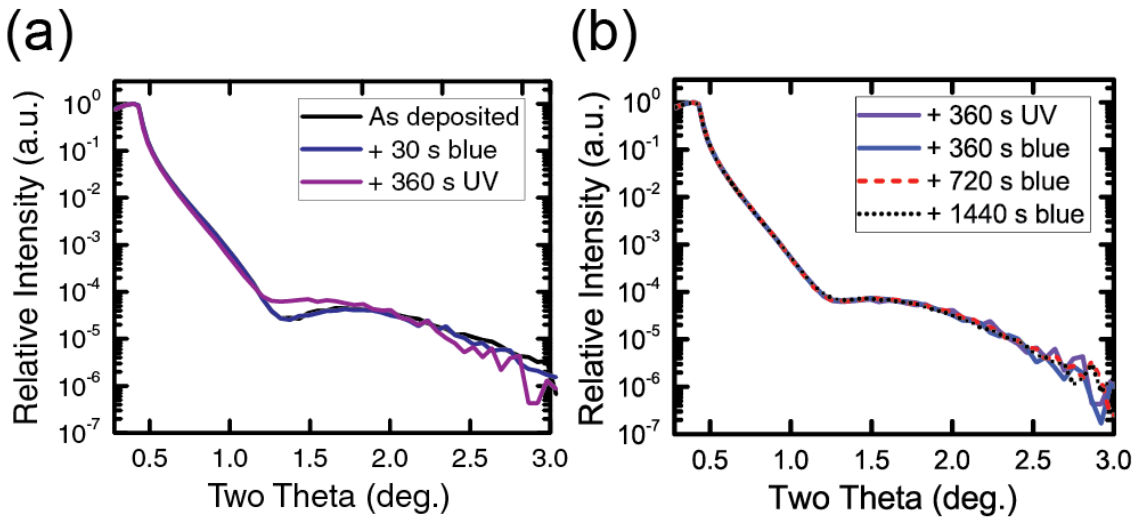

Figure 4-12: XRR characterization of optically induced structural changes. (a) XRR as-deposited, following 30 s blue illumination, and after 360 s of UV illumination. (b) Reflectivity measured after subsequent 360 s, 720 s, and 1440 s blue exposures overlaid on the reflectivity curve after 360 s UV illumination.

was remeasured. No change in the structure was observed (Figure 4-12 (a), solid blue line), as expected because the initial state is composed of molecules in the *trans* isomeric state. The same sample was then exposed to first 30 s and then 360 s of UV light. After the UV exposure there is an increase in intensity near the local minimum (Figure 4-12 (a), solid violet line). This increase in intensity near the local minima is consistent with a change in the structure due to the photoisomerization of the monolayer from the *trans* state to the *cis* state.

The XRR data can be used to estimate the fraction of the monolayer isomerized as a result of UV exposure. Using the simple structural model described above, the reflected intensity curve can be modeled as the weighted average of the reflectivity from the starting structure, which is assumed to be dominated by the *trans* isomer, and the reflectivity from a theoretical 100% *cis* monolayer. Adding the intensities in this way is appropriate for sample configurations in which the isomeric domains have lateral extents on the order of the x-ray transverse coherence length, which is 350 nm for the experimental geometry used here. An analysis of the XRR data shown in Figure 4-12 using this two-domain model gives an isomerization of 11±2% of the area of the monolayer. An analysis of UV-Vis studies under these optical conditions using Equation 4-6 gives an isomerized fraction of 47 to 52% depending on the value of the constant n. The difference between these fractions may arise because the x-ray measurements are insensitive to isomerized areas that are smaller than the lateral x-ray coherence length on the order of 100 nm.

When the XRR experiment was performed with the optical conditions as were used for the UV-Vis spectroscopy studies, no statistically significant change in the reflected intensity was observed. The combination of x-ray and spectral data thus suggests that for experiments conducted with low-intensity light, the isomerized molecules are randomly distributed, rather

than grouped into domains, because a change in the XRR curve is not observed under low intensity illumination.

The return to the *trans* state was probed by studying the structure under blue illumination following UV illumination. The initial UV exposure was followed by exposures with durations of 360 s (Figure 4-12 (d), solid blue line), 720 s (Figure 4-12, dashed red line) and 1440 s Figure 4-12, dotted black line) to light with 460 nm wavelength at an optical intensity of 100 mW/cm^2. An XRR measurement was performed after each of these exposures, but no evidence of structural change in the monolayer was observed in the XRR signal.

To further investigate the monolayer structural changes, the molecular structure was probed by a series of alternating XRR and UV-Vis spectroscopy measurements performed with same power density and exposure times as were used for the measurements shown in Figure 4-12. A 25 mN/m LB sample was prepared on a quartz substrate, its initial structure was probed using XRR, and a subsequent series of measurements were conducted using alternating optical

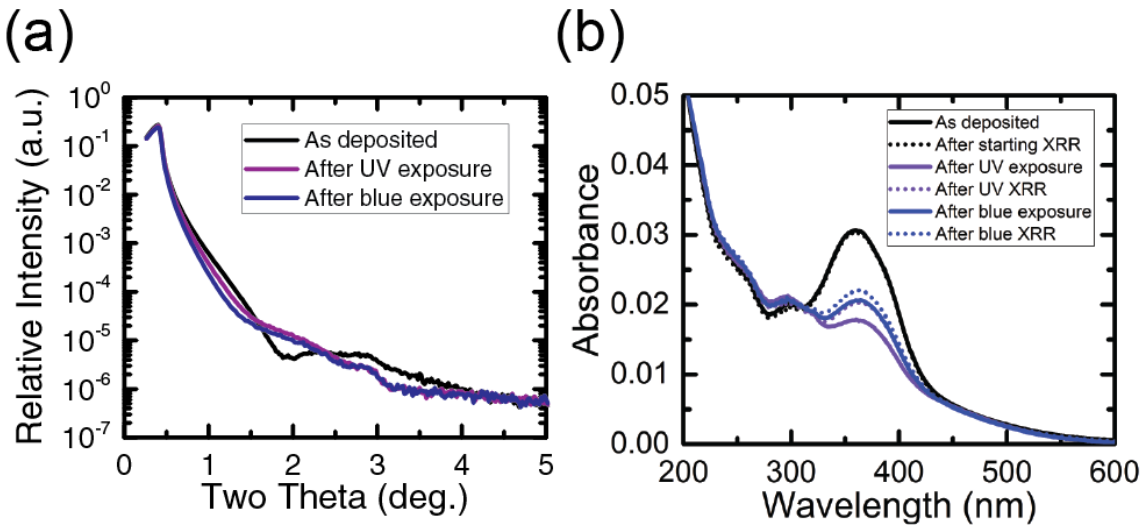

Figure 4-13: (a) XRR of a ReAzoC monolayer deposited at a surface pressure of 25 mN/m before illumination (black), after UV exposure (violet), and after subsequent blue exposure (blue). (b) Optical absorption spectra for the starting structure and before and after each XRR measurement.

illumination and XRR. The 365 nm illumination was carried out at a power density of 94 mW/cm^2 for 360 s. The 460 nm illumination was performed at a power density of 100 mW/cm^2 for 720 s. Optical spectroscopy measurements were performed before and after each XRR measurement. The resulting XRR measurements are shown in Figure 4-13 (a).

The reflectivity curve from the starting structure in Figure 4-13 (a) (black curve) shows a local minimum at $2\theta=2°$. Upon exposure to UV light (violet) the intensity at the local minimum increases and the reflectivity fringe becomes less pronounced. Upon subsequent exposure to blue light, the reflectivity curve remains unchanged. This progression in the reflectivity curves is consistent with the results observed in Figure 4-13.

The UV-Vis spectra resulting from the high power and duration optical exposure are shown in Figure 4-13 (b). The starting UV-Vis spectrum (black, solid) remains unchanged after the x-ray measurement (black, dashed). After UV exposure (violet, solid) the absorption peak at 360 nm is reduced from 0.031 to 0.018, a decrease of 42%. After the XRR measurement, the magnitude of the absorbance increases to 0.021, a recovery of 23% of the original transformation. After blue light exposure, the absorbance magnitude remains unchanged in comparison to the absorbance before blue exposure. This progression of UV-Vis spectra and with the x-ray results together indicate that a fraction of the area of monolayer undergoes *trans*-to-*cis* photoisomerization, followed by a small fraction of the isomerized portion of the monolayer recovering to the *trans* state, and no additional recovery occurring as a result of blue optical exposure. At this higher power and duration exposure, XRR and UV-Vis spectra not only exhibit an isomerization from the *trans* to *cis* state, but also indicate a suppression of the reverse *cis* to *trans* isomerization. The limited *cis* to *trans* photoisomerization is consistent with steric effects from either the bulkiness of the molecule or monolayer close-packing. Damage to

the monolayer from UV/Ozone is unlikely, as the wavelength of UV light used in the experiment is reported as generating extremely low concentrations of ozone.[67]

4.3.4 Structural evolution of ReAzoC monolayers.

Previous work has shown that large isomeric domains can form in azobenzene-containing monolayers deposited as self-assembled monolayers on gold substrates.[68] Large domains of *cis* isomers were observed via STM 90 minutes after a 15 min optical exposure at 365 nm.[68] The long range order is ascribed to a cooperative process within the monolayer. A few molecules initially photoisomerize serving as a nucleation point for the isomeric domains. Around these photoisomerized molecules the intermolecular interactions, such as electronic coupling and the exciton delocalization, are weakened, as well as the reduction in steric hindrance near the *cis* isomer.

Recently, computation work of this system was performed to investigate the underlying physics of this cooperative switching.[69] Point defects like vacancies in the azobenzene monolayer, areas with locally larger free volume or line defects between domains of trans molecule with slightly different tilt orientation serve as nucleation sites for the cis domains.[69] The results showed that the key was the distortion in the local ordering caused by the *cis* isomer reduced the steric hindrance of the twist of the N=N double bond crucial to the photoisomerization mechanism.[69] The result also showed that this effect was much more important than the endothermicity of the photoisomerization reaction of creating a *cis* isomer in a lattice of *trans* isomers.[69] This model also predicts that short irradiation times should yield different monolayer structures between nucleation from point defects or line defects.[69] Point defects are expected to yield small islands of photoisomerized molecules, while line defect would yield long strips of photoisomerized molecules.[69]

A schematic model for this domain growth is shown in Figure 4-14 (a). First, (Figure 4-14 (a)(i)), the monolayer is deposited predominately in the *trans* isomeric state. The locations of the *trans* molecules are indicated by the blue ovals. Depending on the deposition technique there may defects or areas of locally greater free volume. A defect in the monolayer is indicated by the dashed white oval. Then, (Figure 4-14 (a)(ii)), photoisomerization occurs in a small fraction of molecules near defects in the monolayer. It is also possible that there are an equilibrium number of *cis* isomers present in the deposited monolayer. The location of the *cis* isomer is indicated by the violet oval. These *cis* isomers serve as the nucleation points for large

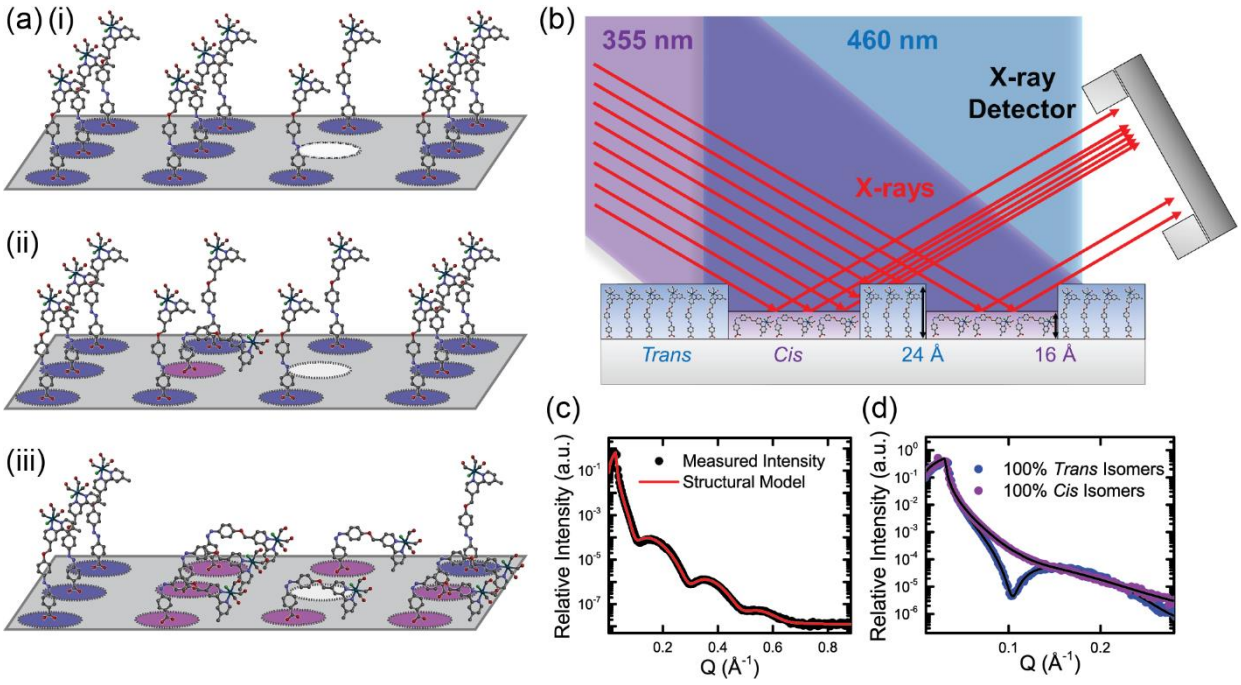

Figure 4-14: (a) Schematic model for the growth of isomeric domains in monolayers of azobenzene containing molecules (i) a monolayer of trans isomers (blue) with a defect in packing of the monolayer. (ii) Upon exoposure to UV illumination, molecules near the defect have a higher probability of photoisomerization (iii) the presence of the defect and initial cis molecule nucleates the growth of domains of cis isomers with continued optical exposure. (b) Microscopic schematic of experimental setup and isomeric monolayer composition during monolayer structural evolution. (c) X-ray reflectivity pattern of 25 mN/m monolayer deposited on quartz substrate. The red represents the fit of the structural model to the data. (d) The reflectivity from a monolayer composed of 100% trans isomers (blue) and 100% cis isomers (violet).

domains of *cis* isomers. Finally, (Figure 4-14 (a)(iii)), molecules near the *cis* molecules photoisomerize to grow into large domains.

It has also been proposed that in densely packed *trans* monolayers, intermolecular coupling and local-field effects weaken the exciton binding strength. When the exciton binding strength is increased via the creation of a *cis* isomer in the *trans* isomer lattice, the neighboring molecules become more likely to photoisomerize thus leading to large isomeric domains.[70] Additional work suggests that the excitonic coupling is so strong, that significantly hinders the *trans* to *cis* photoisomerization process. It is suggested that in order to prevent delocalization on the timescales relevant for switching that the average distance between neighboring molecules should be increased from 6-8 Å by at least a factor of four.[71, 72]

There are two challenges in extracting structural information from monolayers using XRR. The first is that the small monolayer thickness on the order of 2-3 nm produces broad interference fringes in reciprocal space. The dynamic range required to resolve multiple fringes requires a dynamic range of 10^8, which is not accessible via conventional lab sources. The second challenge is in the interpretation of scattering from monolayers with mixed isomeric composition. XRR theory assumes that the surface is laterally homogenous. However, in monolayers containing both *trans* and *cis* isomers, the height and density of the monolayer vary within the x-ray beam footprint, as shown in Figure 4-14 (b).

To overcome the first challenge and achieve the necessary dynamic range, XRR experiments were carried out at station 7-IDC of the Advanced Photon Source at Argonne National Lab. The beam energy was 10 keV with a beam size of 200 μm × 200 μm. Calibration measurements were carried out to determine an x-ray intensity which did not damage to the structure of the molecular monolayer. The beam was then attenuated to this intensity for the

experiments outlined here. The reflected intensity was captured by an avalanche photodiode. A schematic of the experimental setup is shown in Figure 4-14 (b). The second challenge was overcome through the development of a weighted average model for interpreting XRR patterns from inhomogeneous surfaces which will be discussed in detail later in this section.

To investigate the evolution of the monolayer structure during optical exposure and photoisomerization, time resolved reflectivity data were acquired by monitoring the reflected x-ray intensity during UV illumination. The UV light source was a Time-Bandwidth Duetto Laser System operated at 54 kHz at a wavelength of 355 nm. The optical power of the laser was chosen through the use of wave plate as an attenuator. The polarization of the laser beam was horizontal at the sample, independent of the angle of wave plate as a result of a polarizing beam splitter which allowed only the horizontally polarized components of the beam to pass through. The FWHM of the laser beam was 350 μm × 450 μm. The laser beam was oriented such that the angle between the sample surface and the incident laser beam was 4.92º. In this geometry, the horizontal and vertical aspect ratios of the beam are sufficient that the x-ray beam spot is always contained within the optically exposed area. Blue illumination was provided by an Engin LZ1-00DB00 LED with a peak wavelength of 460 nm.

The XRR of an optimized single monolayer deposited at a pressure of 25 mN/m via LB on a quartz substrate is shown in Figure 4-14 (c). Three reflectivity fringes are clearly visible as a result of the high dynamic range and strong ordering and high molecular packing of the monolayer. The periodicity of the fringes arises from the thickness of the molecular monolayer. The amplitude of the fringes arises from the contrast between the density of the molecular monolayer and the density of the underlying substrate as well as the roughness of the top and

bottom interfaces of the monolayer. The peak in intensity at Q = 0.032 $Å^{-1}$ is the result of the incident angle becoming greater than the angle of total external reflection for the substrate.

A theoretical model for the electron density profile of a ReAzoC monolayer of molecules in either the *trans* or the *cis* molecular conformation has been described above. For a monolayer of *trans* molecules, the structural parameters predict a thickness of 24 Å and an electron density of 0.396 $e^-/Å^3$. The red line in Figure 4-14 (c) is a result of the fit to the measured intensity using the structural model. The fit parameters for the optimized monolayer structure on quartz are shown in column (ii) of Table 4-3. These fit parameters are consistent with structural model previously developed, though the increased dynamic range and fit of multiple fringes provides important verification of the monolayer structure.

Table 4-3: Structural parameters extracted from the XRR patterns in Figure 4-15. The fit parameters of monolayer thickness, density, and roughness and substrate roughness are shown for the (i) theoretical model, (ii) a 25 mN/m ReAzoC monolayer on a quartz substrate, (iii) a 25 mN/m ReAzoC monolayer on a silicon substrate, (iv) the 25 mN/m ReAzoC monolayer on a silicon substrate after exposure to a 365 nm-wavelength photon dose of 9.94 × 10^{20} total photons/cm^2, (v) the 25 mN/m ReAzoC monolayer on a silicon substrate after exposure to a 365 nm-wavelength photon dose of 9.94 × 10^{21} total photons/cm^2.

Fit Parameter	**(i) Model**	**(ii) 0 total photons/cm^2 (Quartz)**	**(iii) 0 total photons/cm^2 (Silicon)**	**(iv) 9.94 × 10^{20} total photons/cm^2**	**(v) 9.94 × 10^{21} total photons/cm^2**
Monolayer Thickness (Å)	24	32	31	28.6	24.6
Monolayer Density ($e^-/Å^3$)	0.396	0.44	0.4	0.42	0.48
Substrate Roughness (Å)	8	3.7	4.5	7.5	10
Monolayer Roughness (Å)	N/A	3	6.1	4.8	4.2

For this study, monolayers of the ReAzoC molecule were deposited on silicon and quartz substrates. In order to evaluate the reflectivity from isomerically mixed monolayers, the structure and reflectivity signatures of a monolayer composed of 100% *trans* isomers and of a

monolayer composed of 100% cis isomers needs to be established. The structure of the monolayer created during monolayer deposition is taken to be the structure of a nearly 100% *trans* isomer monolayer since the *trans* isomer is the thermodynamically stable state at ambient conditions. The reflectivity from a monolayer deposited at 25 mN/m is shown blue in Figure 4-14 (d). The reflectivity curve from a 100% *cis* monolayer by exposing an initially *trans* monolayer to 355 nm optical illumination and remeasuring the XRR curve until the reflectivity curve no longer changed in response to additional optical illumination. This reflectivity curve is shown in violet in Figure 4-14 (d). The black lines represent model fits to the experimental data using the model described above. The model parameters extracted from these fits is shown in columns (iii) and (v) of

Table 4-3. The extracted thickness and density of the *trans* monolayer deposited on silicon are slightly less than the structural parameters extracted from the monolayer on quartz. The resulting structural parameters from this fit show a decrease in the thickness of the molecular monolayer of 6.4 Å and an increase in the density of the molecular monolayer of 0.08 $e^-/Å^3$.

To investigate the structural evolution in an isomerically mixed monolayer, a 25 mN/m monolayer was deposited on a silicon substrate. The reflectivity from this as deposited monolayer on silicon is shown as the black curve in Figure 4-14 and is the same as the blue data in Figure 4-14 (d). The ReAzoC monolayer on Si was systematically exposed to increasing optical intensity and total photon dose from the UV laser. After each exposure, the reflectivity from the monolayer was remeasured and the resulting evolution of the reflectivity pattern is shown in Figure 4-15. The result of increased total exposure is that the local minimum initially at Q=0.1 $Å^{-1}$ increases in intensity and shifts to higher scattered wavevectors. Eventually, a point

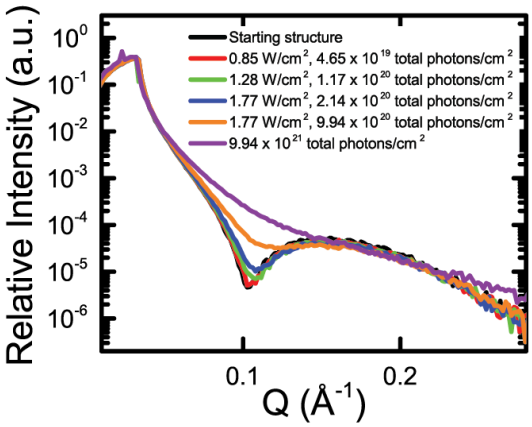

Figure 4-15: Evolution of X-ray reflectivity pattern of the same sample with exposures with increasing optical intensity and total photon dose.

is reached at which the intensity of scattered x-rays from the sample no longer changes with increased photon dose. This corresponds to the curve shown in violet in Figure 4-15, and is the same as the violet data in Figure 4-14 (d). The extracted structural parameters for an intermediate, mixed monolayer surface are shown in Table 1(iv). The decrease in thickness and monolayer density in response to UV exposure is consistent with the photoisomerization of ReAzoC into the *cis* state, which brings the electron rich Re-bipyridine head group closer to the substrate.

In order to interpret the structure of the molecular monolayer at photon doses between the pure *trans* and pure *cis* isomeric monolayer states a reflectivity model in which the lateral inhomogeneity present in isomerically mixed monolayers is accounted for has been developed. Traditional XRR modeling assumes that the surface is homogeneous in the plane direction, with no changes in density, thickness, or roughness within the footprint of the x-ray beam. However, in the case of these reconfigurable monolayers, there is necessarily the creation of a heterogeneous surface in terms of height and density.

The lateral inhomogeneity of the interface can be accounted for by treating the surface as weighted average of the scattering of a pure *trans* monolayer and a pure *cis* monolayer, which are the black and violet in Figure 4-15. This model can be used to estimate the fraction of the monolayer surface area occupied by large enough areas to be observed via XRR. This is shown schematically in Figure 4-16 (a). The purple areas represent large area of predominately *cis* isomers forming within the initial *trans* isomer monolayer structure. A sample model cross section following the dashed black line is shown below with a change in height of the monolayer between the *trans* and *cis* portions of the monolayer. The reflected x-ray intensity for each section is shown above the schematic. This simple structure model can be used to model the scattering from this inhomogeneous surface using Equation 4-8.

$$I = (1 - f)I_{Trans,Fit} + fI_{Cis,Fit}$$

Equation 4-8

In this equation, $I_{Trans,\ Fit}$ and $I_{Cis,\ Fit}$ are the simulated intensities of a pure *trans* and pure *cis* monolayer using the parameters extracted from the data in Figure 4-14 (d). Using Equation 4-8, the XRR spectrum can be predicted as a function of the fraction of the monolayer consisting of *cis* isomers. The results of this structural model are shown in Figure 4-16 (b). The evolution of the XRR pattern is most evident in the evolution of the local minimum near Q=0.1 $Å^{-1}$, with the intensity increasing and the local minimum shifting to higher Qs. This evolution accurately reproduces the evolution of the experimental reflectivity patterns shown in Figure 4-15.

This evolution in the XRR pattern indicates the grown of large *cis* isomeric domains within the predominately *trans* isomeric monolayer. Additionally, this model allows the estimation of the fraction of the monolayer photoisomerized directly from the XRR spectrum. An alternative model for photoisomerization would be a model where the molecules

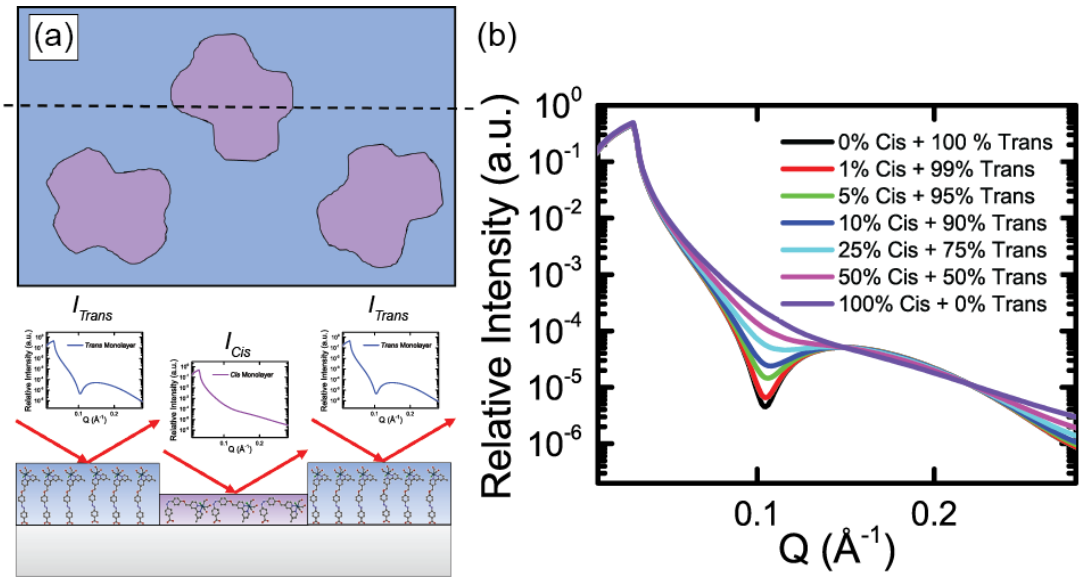

Figure 4-16: (a) (Top) Schematic top view of large areas of cis isomers forming within the monolayer (Bottom) A schematic cross section of the dashed black line in the top of the figure showing the change in height as a result of a change in the molecular conformation. (b) Predicted reflected x-ray intensity as a function of the fraction of the monolayer in the cis conformation using Equation 4-8.

photoisomerize in a spatially random distribution. However, if this model is applied is used to simulate the evolution of the XRR curves, a distinctly different progression would be observed. In the case of random photoisomerization, the increase the number of cis isomers would appear as an increase in the roughness at the air-monolayer interface. The monolayer parameters would appear to be the average of the height and electron density of the corresponding fraction of *trans* and *cis* isomers. In this model, the increasing roughness at the air-monolayer interfaces results in a decay in the reflected intensity at x-ray wavevectors larger than the local minimum. This decay in intensity at large wavevectors is not observed.

4.3.5 Isomeric domain growth in reconfigurable monolayers.

Using the isomeric domain structural model, it is possible to evaluate the structural evolution of the monolayer on the timescale of seconds. By monitoring the structural evolution in real-time structural questions such as the mechanism by which the domain growth occurs, the

speed at which this structural evolution is occurring and the dependence on optical intensity are able to be investigated. Additionally, it is possible to evaluate the stability and reversibility of the structural state.

To evaluate these dynamic structural questions, the intensity at a single x-ray incident angle was monitored as a function of time. Even at the synchrotron, the capture of a complete XRR curve over multiple angles is limited to the timescale of minutes. To improve the time resolution, the experimental setup was aligned at the point of maximum contrast between the *trans* and *cis* isomeric monolayers at $Q = 0.1$ Å^{-1} and the change in the intensity of the reflection at this angle was monitored as a function of optical intensity and total photon dosage. Optical intensities from 0.3 W/cm^2 to 4.3 W/cm^2 were used to expose previously unexposed regions of the same sample. Each sample exposure began with monitoring the reflected intensity for 10 s to establish the starting intensity and then begin to expose the sample. The intensity during the initial 10 s was then averaged and subtracted from the remaining time points to establish the change in intensity in response to the illumination. The results are shown in Figure 4-17 (a). The intensity continues to change on the timescale of 100s to the 1000s of seconds, with the rate of change in the intensity increasing with increasing optical intensity.

Using the structural model developed above, the change in the reflected intensity is converted to the fraction of the monolayer photoisomerized. Using the reflectivity curves from Figure 4-14 (d) as the 100% *trans* and 100% *cis* end points, the change in the reflected intensity from Figure 4-17 (a) are linearly related to the fraction of the monolayer isomerized. Small differences in incident intensity, sample size, angle of the reflected x-rays and starting monolayer structure are accounted for when converting the change in intensity to the fraction of the monolayer photoisomerized. Additionally, the total exposure time and optical intensity are

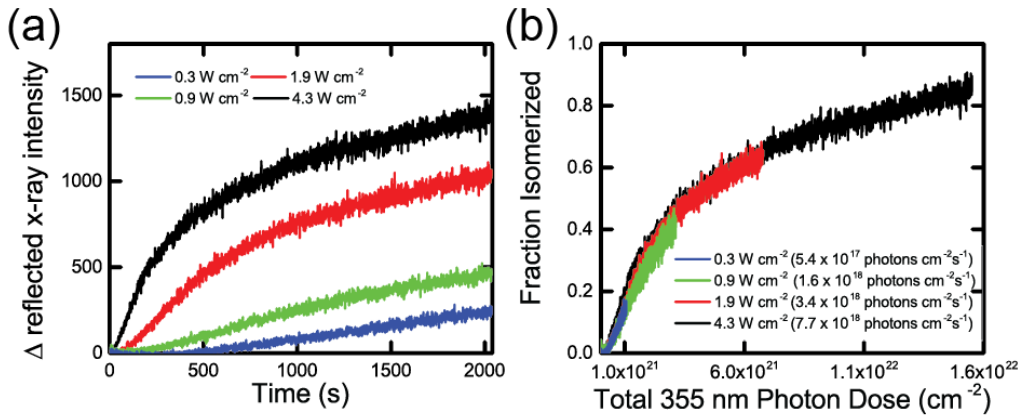

Figure 4-17: (a) Plot of the change intensity vs. exposure time for different positions on the sample exposed to different UV optical intensities. (b) Plot of the fraction of the monolayer isomerized vs. the total photons dose/cm^2. The data are converted from (a) using the structural model described in the text.

converted into the total 355 nm photon dose/cm^2. The fraction of the monolayer isomerized as a function of the total photon dose/cm^2 is shown in Figure 4-17 (b). Figure 4-17 (b) shows that fraction of the monolayer photoisomerized is independent of the optical power used and rather is only a function of the total photon dose/cm^2, with all the data following the same general curve.

The data shown in Figure 4-17 (b) also contain information about the mechanism through which the isomeric domains form in the monolayer. The data in Figure 4-17 (b) show the characteristic s shaped curve consistent with Johnson-Mehl-Avrami-Kolmogorov (JMAK) model. This curve is characterized by slow transformation rates at the beginning and end of the transformation. The JMAK model is used to describe how materials transform from one phase of matter to another, in this case the nucleation and growth of *cis* domains in a starting structure of primarily *trans* isomers. The JMAK model makes three primary assumptions. First it assumes that nucleation occurs randomly and homogenously over the entire untransformed portion. In the case of the ReAzoC monolayers, this translates to a model where the first molecules to photoisomerize from *trans* to *cis*, do so with a random spatial distribution within the monolayer. This random distribution is supported by previous measurements at low optical

intensities in which the photoisomerization was observed in UV-Vis spectroscopy measurements, but not in XRR measurements. The second and third assumptions are that the growth rate does not depend on the extent of the transformation and that the growth rate is the same in all directions.

The data in Figure 4-17 (b) can be interpreted using the JMAK model. The JMAK equation, shown in equation 2, describes the fraction transformed as a function time.

$$f = 1 - e^{-K*t^n}$$

Equation 4-9

K is a lumped parameter including the nucleation and growth rate while *n* describes the dimensionality of transformation. In the case of the photoisomerization of the ReAzoC monolayer *f* is the fraction of the monolayer in the *cis* isomeric state and *t* is replaced the total photon dose (*D*) which is simply the optical intensity used times the time after starting the exposure. Since the system is a monolayer system, the maximum expected value of *n* is n=3, which would correspond to two-dimensional domain growth with continuing nucleation, a value of n=2 indicates two dimensional growth after nucleation has stopped, and a value of n=1 would indicate one dimensional growth after nucleation has stopped.

The parameters *n* and *K* can be extracted by converting the data to the form:

$$\log(-\ln[1 - f(t)]) = \log K + n \log D$$

Equation 4-10

Using this relation, the data from Figure 4-17 (b) are replotted in Figure 4-18 (a). In this construction the slope of the data at any given point is the dimensionality of the transformation and the y-intercept is log *K* and contains information about the nucleation and growth rates of the isomeric domains. The data are very noisy at low total photon doses as a result of the small change in intensity at those times corresponding to small fraction photoisomerized. In order to extract the parameters for *n* and *K*, the four data sets in Figure 4-18 (a) are combined and smoothed using a boxcar average. This data is shown as the black circles in Figure 4-18 (b). The black circles form a locus of points with decreasing slope as the total photon dose increases. Typical JMAK plots are characterized by a single value of *n* and *K*.

However, looking at Figure 4-18 (b), it is obvious this system is not characterized by a single value of *n* and *K*. Instead the transformation is characterized by regions of three different slopes. At values of the total photon dose below 3.16×10^{20} photons/cm^2, which corresponds to a total photoisomerized fraction of 9.8%, the JMAK plot indicates that at low optical exposures and fractions isomerized, the monolayer is undergoing high rates nucleation and two dimensional growth. At values of the total photon dose between 3.16×10^{20} photons/cm^2 and 1.58×10^{21}

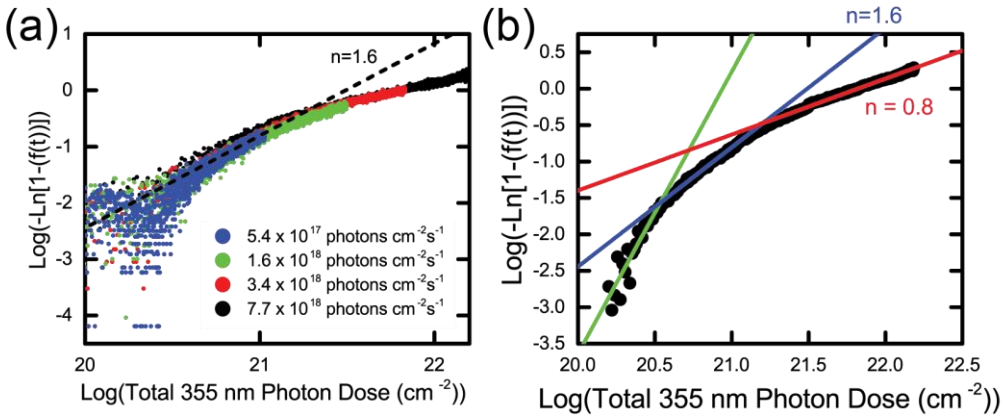

Figure 4-18: (a) JMAK plot for each different optical intensity use to photoisomerize the monolayer. (b) The data from (a) are combined and smoothed to allow extraction of the JMAK constants n and K. The fits in (b) indicate nucleation of isomeric domains followed by two-dimensional growth of the domains which slows at fractions isomerized greater than 28.5%.

photons/cm^2, between 9.8% isomerized and 28.4% isomerized, the transformation is characterized by n=1.64 and Log K = -35.2. These values indicate that in this growth regime, that nucleation has greatly slowed down or stopped all together and that the domains are growing via two-dimensional growth. At values of the total photon does greater than $10^{21.2}$, which corresponds to a total photoisomerized from of 28.4%, the transformation is characterized by n=0.76 and Log K = -16.75. The values indicate that photoisomerization rate is reduced. The reduction could be caused due to experimental factors such as the aspect ratio of the x-ray beam being 50 times longer than it is wide at small incidence angles which could mimic the signature of one-dimensional growth, or a slowing of the growth rate due to sample effects. The XRR results shown in this work are consistent with the growth of large domains of *cis* isomers within the *trans* isomeric monolayer. Additionally, the growth model is consistent with the model outlined in Figure 4-14 (a), in that a small fraction of molecules can reversibly photoisomerize followed initially by 2D growth and a reduction or elimination of additional nucleation.

It is also possible to reconsider a model in which the molecules photoisomerize with a spatially random distribution. In this case, the evolution of the fraction switched vs. total photon dose (time) curve would be expected to evolve with a curve modeled by:

$$f = 1 - e^{-K*D}$$

Equation 4-11

However, this model does not fit the data in Figure 4-17 (b) and thus it is discounted as was also done previously.

After exposure to UV light the samples were exposed to 460 nm illumination for periods of time up to 4000 s at an intensity of 9.5 mW/cm^2. However, no change in the reflected intensity

or structure was observed. This indicates an enhanced stability of the *cis* molecules within these large domains. This behavior has been observed previously and attributed to stabilization from enhanced π-π orbital overlap within the *cis* domains in comparison to isolated *cis* monomers.

4.4 Conclusions

Molecular monolayers of a new molecule with electron donating characteristics and externally reconfigurable structure have been fabricated. The physical and electronic structure of the molecules and monolayers have been characterized and show near full coverage when deposited via the LB technique. Monolayers of three different molecules ReEC, Re2TC, and ReAzoC show a closely packed structure with the molecules standing normal to the substrate, as indicated by the high quality of XRR data. Comparing the ReEC and Re2TC monolayers shows a more pronounced XRR fringe indicating a greater degree of ordering which is attributed to the more rigid bridge group and is consistent with other experimental results.

In the case of ReAzoC, the molecules and monolayers showed evidence of structural reconfiguration in response to optical exposure both in solution and when confined to a monolayer. A structural model for the photoisomerization and reconfiguration in the monolayer has been developed, in which a fraction of the monolayer is isomerized, depending on the intensity and duration of optical exposure. In this domain scattering model, the initial monolayer is deposited a single monolayer of predominately *trans* isomers. Structural reconfiguration within the monolayer progresses via the growth of large *cis* isomeric domains. Initially, a small, spatially random distribution of molecules can switch reversibly. At more intense and higher dose optical exposures, a larger fraction of the monolayer is driven into the *cis* state, but the photoisomerization process becomes irreversible. This limited reversibility of the photoisomerization in monolayers, hypothesized to be steric hindrance or other molecule-surface

interactions. Finally, the mechanism by which the large domains grow nucleation and growth mode characterized through the JMAK model with separate growth regimes of nucleation and growth, two-dimensional growth, and the appearance of one-dimensional growth.

This work has important implications on the fields of electronic organic-inorganic interfaces and on reconfigurable materials. With this work as a basis, systems with fully switchable functionality to be developed to act as switches to turn on and off charge transfer from the monolayer. Additionally, in the irreversible switching limit, these monolayers could be used as a kind of photoresist, where the charge injection can be spatially patterned to create conductive channels through the passivation of trap states. In the field of reconfigurable materials, this work has important implications in areas such as solar thermal fuels and phostoswitchable metal organic frameworks. Based on this initial work it would be important to avoid low isomerization fractions by minimizing confinement in these systems to increase the efficiency and that it may be challenging to coordinate the simultaneous photoisomerization of the azobenzene groups to effectively release the cargo stored in the metal-organic framework.

4.5 References

1. Delorme, N., Bardeau, J.-F., Bulou, A. & Poncin-Epaillard, F. Azobenzene-containing monolayer with photoswitchable wettability. *Langmuir* **21,** 12278–12282 (2005).
2. Zheng, Y. B. *et al.* Photoresponsive molecules in well-defined nanoscale environments. *Adv. Mater.* **25,** 302–312 (2013).
3. Han, M. *et al.* Realization of highly photoresponsive azobenzene-functionalized monolayers. *J. Mater. Chem.* **21,** 4696–4702 (2011).
4. Merino, E. & Ribagorda, M. Control over molecular motion using the cis-trans photoisomerization of the azo group. *Beilstein J. Org. Chem.* **8,** 1071–1090 (2012).
5. Kim, M., Safron, N. S., Huang, C., Arnold, M. S. & Gopalan, P. Light-driven reversible modulation of doping in graphene. *Nano Lett.* **12,** 182–187 (2012).
6. Weber, R. *et al.* Photoemission from azobenzene alkanethiol self-assembled monolayers. *J. Phys. Chem. B* **107,** 7768–7775 (2003).
7. Hsu, C.-C. *et al.* Environment-dependent ultrafast photoisomerization dynamics in azo dye. *J. Phys. Chem. A* **115,** 11508–11514 (2011).
8. Silvi, S., Venturi, M. & Credi, A. Light operated molecular machines. *Chem. Commun.* **47,** 2483–2489 (2011).
9. Abendroth, J. M., Bushuyev, O. S., Weiss, P. S. & Barrett, C. J. Controlling motion at the nanoscale: Rise of the molecular machines. *ACS Nano* **9,** 7746–7768 (2015).
10. Browne, W. R. & Feringa, B. L. Making molecular machines work. *Nat. Nanotechnol.* **1,** 25–35 (2006).
11. Browne, W. R. & Feringa, B. L. Light switching of molecules on surfaces. *Annu. Rev. Phys. Chem.* **60,** 407-428 (2009).

12. Zhitomirsky, D., Cho, E. & Grossman, J. C. Solid-state solar thermal fuels for heat release applications. *Adv. Energy Mater.* **6,** 1502006 (2016).

13. Luo, W. *et al.* A high energy density azobenzene/graphene hybrid: a nano-templated platform for solar thermal storage. *J. Mater. Chem. A* **3,** 11787–11795 (2015).

14. Xia, X., Yu, H., Wang, L. & ul-Abdin, Z. Recent progress in ferrocene- and azobenzene-based photoelectric responsive materials. *RSC Adv.* **6,** 105296–105316 (2016).

15. Wang, S., Song, Y. & Jiang, L. Photoresponsive surfaces with controllable wettability. *J. Photochem. Photobiol. C Photochem. Rev.* **8,** 18–29 (2007).

16. Russew, M.-M. & Hecht, S. Photoswitches: From molecules to materials. *Adv. Mater.* **22,** 3348–3360 (2010).

17. Seki, T. New strategies and implications for the photoalignment of liquid crystalline polymers. *Polym. J.* **46,** 751–768 (2014).

18. Léonard, E., Mangin, F., Villette, C., Billamboz, M. & Len, C. Azobenzenes and catalysis. *Catal. Sci. Technol.* **6,** 379–398 (2016).

19. Kolpak, A. M. & Grossman, J. C. Azobenzene-functionalized carbon nanotubes as high-energy density solar thermal fuels. *Nano Lett.* **11,** 3156–3162 (2011).

20. Feng, W., Luo, W. & Feng, Y. Photo-responsive carbon nanomaterials functionalized by azobenzene moieties: structures, properties and application. *Nanoscale* **4,** 6118–6134 (2012).

21. Qin, C. *et al.* A supramolecular assembly of cross-linked azobenzene/polymers for a high-performance light-driven actuator. *J. Mater. Chem. A* **3,** 16453–16460 (2015).

22. Zong, Y., Tawa, K., Menges, B., Rühe, J. & Knoll, W. Azobenzene-containing polyamic acid with excellent Langmuir−Blodgett−Kuhn film formation behavior suitable for all-optical switching. *Langmuir* **21,** 7036–7043 (2005).

23. Cristofolini, L., Berzina, T., Fontana, M. p. & Konovalov, O. Structure and stability of molecular layers of a photosensitive azo-polyacrylate by x-rays reflectivity and GID. *Mol. Cryst. Liq. Cryst. Sci. Technol. Sect. Mol. Cryst. Liq. Cryst.* **375,** 689–699 (2002).

24. Grätzel, M. Dye-sensitized solar cells. *J. Photochem. Photobiol. C Photochem. Rev.* **4,** 145–153 (2003).

25. O'Regan, B. & Grätzel, M. A low-cost, high-efficiency solar cell based on dye-sensitized colloidal TiO2 films. *Nature* **353,** 737–740 (1991).

26. Hagfeldt, A., Boschloo, G., Sun, L., Kloo, L. & Pettersson, H. Dye-sensitized solar cells. *Chem. Rev.* **110,** 6595–6663 (2010).

27. Anfuso, C. L. *et al.* Covalent attachment of a rhenium bipyridyl CO_2 reduction catalyst to rutile TiO_2. *J. Am. Chem. Soc.* **133,** 6922–6925 (2011).

28. Ashford, D. L. *et al.* Photoinduced electron transfer in a chromophore–catalyst assembly anchored to TiO_2. *J. Am. Chem. Soc.* **134,** 19189–19198 (2012).

29. Albert, K. J. *et al.* Cross-reactive chemical sensor arrays. *Chem. Rev.* **100,** 2595–2626 (2000).

30. Heller, A. Electrical connection of enzyme redox centers to electrodes. *J. Phys. Chem.* **96,** 3579–3587 (1992).

31. Asbury, J. B., Hao, E., Wang, Y. & Lian, T. Bridge length-dependent ultrafast electron transfer from Re polypyridyl complexes to nanocrystalline TiO_2 thin films studied by femtosecond infrared spectroscopy. *J. Phys. Chem. B* **104,** 11957–11964 (2000).

32. Xiong, W. *et al.* Transient 2D IR spectroscopy of charge injection in dye-sensitized nanocrystalline thin films. *J. Am. Chem. Soc.* **131,** 18040–18041 (2009).

33. Paoprasert, P. *et al.* Bridge-dependent interfacial electron transfer from rhenium−bipyridine complexes to TiO_2 nanocrystalline thin films. *J. Phys. Chem. C* **114,** 9898–9907 (2010).

34. Bauer, C., Boschloo, G., Mukhtar, E. & Hagfeldt, A. Electron injection and recombination in $Ru(dcbpy)_2(NCS)_2$ sensitized nanostructured ZnO. *J. Phys. Chem. B* **105,** 5585–5588 (2001).

35. Basu, K. *et al.* Enhanced photovoltaic properties in dye sensitized solar cells by surface treatment of SnO_2 photoanodes. *Sci. Rep.* **6,** 23312 (2016).

36. Christianson, J. R. & Schmidt, J. R. Structural heterogeneity and dynamics of dyes on TiO_2: implications for charge transfer across organic–inorganic interfaces. *Phys. Chem. Chem. Phys.* **17,** 3731–3740 (2015).

37. Ruther, R. E., Cui, Q. & Hamers, R. J. Conformational disorder enhances electron transfer through alkyl monolayers: Ferrocene on conductive diamond. *J. Am. Chem. Soc.* **135,** 5751–5761 (2013).

38. Walters, K. A., Premvardhan, L. L., Liu, Y., Peteanu, L. A. & Schanze, K. S. Metal-to-ligand charge transfer absorption in a rhenium(I) complex that contains a π-conjugated bipyridine acceptor ligand. *Chem. Phys. Lett.* **339,** 255–262 (2001).

39. Busby, M. *et al.* Rhenium-to-benzoylpyridine and rhenium-to-bipyridine MLCT excited states of fac-$[Re(Cl)(4\text{-benzoylpyridine})_2(CO)_3]$ and fac-$[Re(4\text{-benzoylpyridine})(CO)_3(bpy)]^+$: A time-resolved spectroscopic and spectroelectrochemical study. *Inorg. Chem.* **43,** 4523–4530 (2004).

40. Paoprasert, P. *et al.* Dipolar chromophore functional layers in organic field effect transistors. *Adv. Mater.* **20,** 4180–4184 (2008).

41. Ferri, V. *et al.* Light-powered electrical switch based on cargo-lifting azobenzene monolayers. *Angew. Chem. Int. Ed.* **47,** 3407–3409 (2008).

42. Lednev, I. K. *et al.* Femtosecond time-resolved UV-visible absorption spectroscopy of trans-azobenzene: dependence on excitation wavelength. *Chem. Phys. Lett.* **290,** 68–74 (1998).

43. Lednev, I. K., Ye, T.-Q., Hester, R. E. & Moore, J. N. Femtosecond time-resolved UV−visible absorption spectroscopy of trans-azobenzene in solution. *J. Phys. Chem.* **100,** 13338–13341 (1996).

44. Krekiehn, N. R. *et al.* UV/Vis spectroscopy studies of the photoisomerization kinetics in self-assembled azobenzene-containing adlayers. *Langmuir* **31,** 8362–8370 (2015).

45. Valley, D. T., Onstott, M., Malyk, S. & Benderskii, A. V. Steric hindrance of photoswitching in self-assembled monolayers of azobenzene and alkane thiols. *Langmuir* **29,** 11623–11631 (2013).

46. Wagner, S. *et al.* Reversible photoisomerization of an azobenzene-functionalized self-assembled monolayer probed by sum-frequency generation vibrational spectroscopy. *Phys. Chem. Chem. Phys.* **11,** 6242–6248 (2009).

47. Moldt, T. *et al.* Tailoring the properties of surface-immobilized azobenzenes by monolayer dilution and surface curvature. *Langmuir* **31,** 1048–1057 (2015).

48. Joo, Y. *et al.* Structured layer of rhenium dye on SiO_2 and TiO_2 surfaces by Langmuir–Blodgett technique. *Langmuir* **30,** 6104–6113 (2014).

49. El Garah, M., Palmino, F. & Cherioux, F. Reversible photoswitching of azobenzene-based monolayers physisorbed on a mica surface. *Langmuir* **26,** 943–949 (2010).

50. Tamada, K. *et al.* Structure and growth of hexyl azobenzene thiol SAMs on Au(111). *Langmuir* **14,** 3264–3271 (1998).

51. Wen, Y. *et al.* Photochemical-controlled switching based on azobenzene monolayer modified silicon (111) surface. *J. Phys. Chem. B* **109,** 14465–14468 (2005).

52. Laaser, J. E. *et al.* Dye self-association identified by intermolecular couplings between vibrational Modes as revealed by infrared spectroscopy, and implications for electron injection. *J. Phys. Chem. C* **118,** 5854–5861 (2014).

53. Asbury, J. B., Hao, E., Wang, Y., Ghosh, H. N. & Lian, T. Ultrafast electron transfer dynamics from molecular adsorbates to semiconductor nanocrystalline thin films. *J. Phys. Chem. B* **105,** 4545–4557 (2001).

54. Dominey, R. N., Hauser, B., Hubbard, J. & Dunham, J. Structural, spectral, and charge-transfer properties of $ClRe(CO)_3$(2-PP) [2-PP = N-(2-pyridinylmethylene)phenylamine] and $ClRe(CO)_3$(2-PC) [2-PC = N-(2-pyridinylmethylene)cyclohexylamine]. *Inorg. Chem.* **30,** 4754–4758 (1991).

55. Henry, M. S. & Hoffman, M. Z. Photophysics and photochemistry of aromatic nitrogen heterocycles. Fluorescence from 2,2'-bipyridine and 1,10-phenanthroline. *J. Phys. Chem.* **83,** 618–625 (1979).

56. Pilz, C. S. & Steinem, C. Modulation of the conductance of a 2,2'-bipyridine-functionalized peptidic ion channel by Ni^{2+}. *Eur. Biophys. J. EBJ* **37,** 1065–1071 (2008).

57. Birnbaum, P. P. & Style, D. W. G. The photo-isomerization of some azobenzene derivatives. *Trans. Faraday Soc.* **50,** 1192–1196 (1954).

58. Sierocki, P. *et al.* Photoisomerization of azobenzene derivatives in nanostructured silica. *J. Phys. Chem. B* **110,** 24390–24398 (2006).

59. Samanta, S., McCormick, T. M., Schmidt, S. K., Seferos, D. S. & Woolley, G. A. Robust visible light photoswitching with ortho-thiol substituted azobenzenes. *Chem. Commun.* **49,** 10314–10316 (2013).

60. Jens Als-Nielsen & Des McMorrow. *Elements of Modern X-ray Physics*. (John Wiley & Sons, Ltd, 2011).

61. Parratt, L. G. Surface studies of solids by total reflection of x-rays. *Phys. Rev.* **95,** 359–369 (1954).

62. *X-ray and Neutron Reflectivity*. **770,** (Springer Berlin Heidelberg, 2009).

63. Sakurai, K. *Introduction to X-Ray Reflectivity*. (Kodansya, 2008).

64. Sakurai, K. & Iida, A. Fourier analysis of interference structure in x-ray specular reflection from thin films. *Jpn. J. Appl. Phys.* **31,** L113–L115 (1992).

65. Stoev, K. N. & Sakurai, K. Review on grazing incidence x-ray spectrometry and reflectometry. *Spectrochim. Acta Part B At. Spectrosc.* **54,** 41–82 (1999).

66. Björck, M. & Andersson, G. *GenX* : an extensible x-ray reflectivity refinement program utilizing differential evolution. *J. Appl. Crystallogr.* **40,** 1174–1178 (2007).

67. Vig, J. R. UV/ozone cleaning of surfaces. *J. Vac. Sci. Technol. A* **3,** 1027–1034 (1985).

68. Pace, G. *et al.* Cooperative light-induced molecular movements of highly ordered azobenzene self-assembled monolayers. *Proc. Natl. Acad. Sci.* **104,** 9937–9942 (2007).

69. Cantatore, V., Granucci, G., Rousseau, G., Padula, G. & Persico, M. Photoisomerization of self-assembled monolayers of azobiphenyls: Simulations highlight the role of packing and defects. *J. Phys. Chem. Lett.* **7,** 4027–4031 (2016).

70. Optical properties of azobenzene-functionalized self-assembled monolayers: Intermolecular coupling and many-body interactions. *J. Chem. Phys.* **145,** 234701 (2016).

71. Utecht, M., Klamroth, T. & Saalfrank, P. Optical absorption and excitonic coupling in azobenzenes forming self-assembled monolayers: a study based on density functional theory. *Phys. Chem. Chem. Phys.* **13,** 21608–21614 (2011).

72. Gahl, C. *et al.* Structure and excitonic coupling in self-assembled monolayers of azobenzene-functionalized alkanethiols. *J. Am. Chem. Soc.* **132,** 1831–1838 (2010).

73. McElhinny, K. M. *et al.* Optically reconfigurable monolayer of azobenzene donor molecules on oxide surfaces. *Langmuir* (2017). **9,** 2157-2168 (2017)

Chapter 5: Surface faceting energetics and kinetics evaluated by x-ray reflectivity

Portions of this chapter were adapted with permission from McElhinny et al., Surface Science, **647, 90-95, (2016).*

5.1 Introduction

The formation of surface facets provides insight into the chemistry and energetics of crystal surfaces and their interfaces with other materials. The faceting of an initially planar surface occurs through a process of nanometer scale self-assembly that exposes new crystal faces and creates additional surface area.[1] While surface faceting is ultimately driven by a minimization of the total surface free energy, the evolution of the surface upon, for example, the creation of interfaces, is controlled by kinetic processes including nucleation and diffusion.[1] By studying the surface geometry and processing conditions that lead to faceting, it is possible to examine the interplay between thermodynamics and kinetics in complex interfacial systems. Although faceting phenomena have most often been observed with atomic or molecular absorbates, recent observations have found that faceting can also occur during the formation of two-dimensional materials.

In particular, the formation of Ge facets below graphene grown on Ge (001) via chemical vapor deposition was recently reported.[2] These Ge facets form during the deposition of graphene at elevated temperatures and are stable under ambient conditions after rapid cooling to room temperature.[2] The faceting is highly selective, as it only occurs in areas where graphene has nucleated and is even observed below relatively small crystals with dimensions less than 10 nm. Atomic force microscopy shows that the Ge/graphene faceting pattern exhibits four-fold symmetry, with approximately equal area occupying each of the four facet domains.[2] The nanometer-scale structure of the faceted Ge/graphene surface is clear from scanning tunneling

microscopy studies, which show that the facets are stable under ambient conditions and upon reintroduction into vacuum.[2] These Ge facets belong to the {10L} family. Interestingly, such faceting was not reported in other studies of graphene growth on Ge (001), which may be due to differences in growth conditions, differences in the thermal profile, or the absence of characterization of the Ge surface.[3, 4]

The formation of {10L} facets has been previously observed on Ge surfaces under a number of conditions. The heteroepitaxial growth of elastically strained Ge with a thickness of a few atomic layers on Si (001) results in the formation of Ge islands with {105} facets, allowing the elastic relaxation of the near-surface region and lowering the total strain energy.[5,6] The Ge {107} facet is formed as a result of mounding in Sn-mediated Ge/Ge (001) homoepitaxy.[7] Contributions to the relative energetic stability of facets on Ge include the atomic reconstruction of the faceted surface and the strain dependence of the Ge surface energy.[6, 8]

The work in this thesis has focused on developing and performing systematic x-ray reflectivity (XRR) studies probing the faceting of Ge (001) surfaces during the chemical vapor deposition of continuous graphene layers as a window into the interplay between the surface kinetics and thermodynamics. This technique offers a statistical measurement of the surface facets angles, orientations, and angular distributions of the Ge facets beneath the graphene layer. These measurements are then used provide insight into the underlying energetics of the Ge/graphene during the deposition process. Unlike atomic force microscopy and scanning tunneling microscopy measurements, x-ray scattering measurements provide precise insight into the orientation and roughness of the facets over large areas, providing precise statistical averages for the faceted surface structure.

The creation of multiple surfaces with different orientations splits the surface diffraction spots in surface x-ray diffraction and reflectivity, producing multiple crystal truncation rods.[9] For an accurately oriented high-index surface, each truncation rod passes through both the origin of reciprocal space and a series of Bragg reflections. With small misorientations, the origin and each Bragg reflection produce a rod of intensity at a specular angle depending on the misorientation.[9] At the small angles of x-ray incidence on which focused on in this work, the specular reflection from the surface is thus split by the pattern of facets.[10] In the limit of the x-ray beams with short transverse coherence lengths produced by laboratory x-ray sources, the scattering pattern of surfaces with multiple facets can be accurately approximated as the appropriately weighted sum of the intensities of a series of misoriented surfaces. XRR studies of faceted surfaces have included step-driven faceting in Si[11–13], faceting in Au[14] and Pt,[15] and earlier studies on Cu surfaces.[10] In a technical sense, the results reported here extend XRR methods to the special case of Ge/graphene and describe the analysis methods necessary to perform such studies using large two-dimensional x-ray detectors.

Understanding the surface energetics and interactions of the Ge/graphene system is also important to advance the synthesis of graphene on semiconducting substrates, and in ultimately promoting better compatibility of graphene with conventional microelectronics.[2, 3] The formation of facets during the synthesis of graphene nanoribbons on Ge (001) is particularly interesting, as this growth process has the potential to lead to arrays of high-quality semiconducting nanoribbons directly on a substrate compatible with conventional microelectronics.

5.2 Formation of single-layer graphene on a Ge(001) surface

The synthesis of the graphene sheets on germanium substrates presented here was developed by Bobby Jacobberger and the Arnold Group at UW-Madison. The following discussion serves to explain the samples and set up the processing conditions used for the XRR studies.

The faceting of the Ge surfaces was investigated using Ge/graphene samples grown at temperatures of 870 °C, 910 °C, and 920 °C at atmospheric pressure using 4.6 sccm of CH_4 as the carbon precursor and a mixture of 200 sccm of Ar and 100 sccm of H_2 as the reducing carrier gas. Growth times of 42, 12, and 10 hours were used for synthesis at 870 °C, 910 °C, and 920 °C, respectively, to ensure that a continuous layer of graphene covered the entire surface. Following growth, the samples were rapidly cooled in the same environment used during synthesis by sliding the furnace away from the growth zone to bring the samples to room temperature. This process resulted in complete coverage of the surface by a single layer of graphene distributed across sharp hill-and-valley facets.[2] Figure 5-1 (a) and (b) show SEM and AFM images, respectively, of the local surface faceting of the Ge under the graphene. The

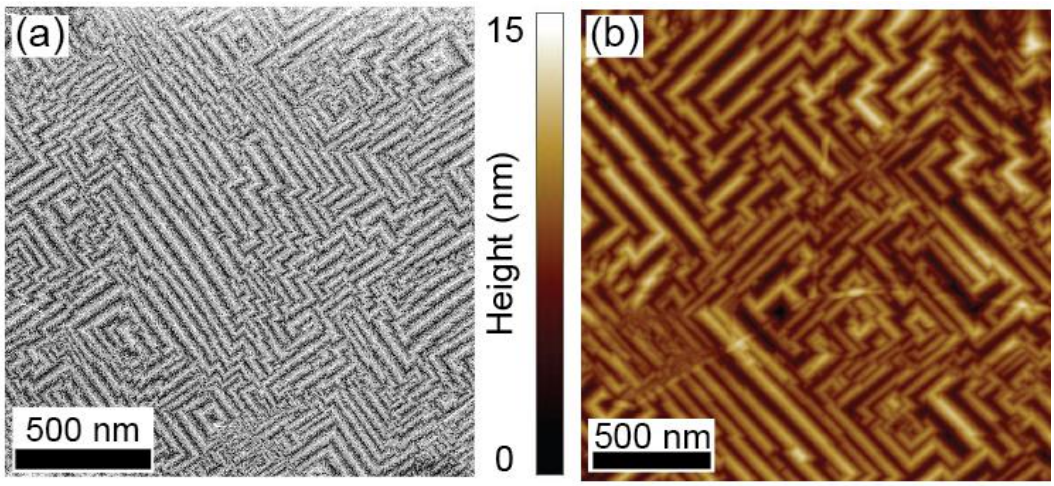

Figure 5-1: (a) SEM and (b) AFM images of faceted Ge (001)/graphene.

dimensions of the faceted structure visible in the SEM and AFM images are typically less than 6 nm high and nearly 70 nm wide, valley-to-valley, along their short axis. The ridges between facets are nearly parallel to the [100] and [010] directions. The faint ripples visible in the AFM image in Figure 5-1 (b) arise from wrinkling of the graphene during cooling as a result of the mismatch in the thermal expansion coefficient between the graphene and the Ge. Interestingly, graphene growth followed by a much slower cooling rate of 0.5 °C/min results in a different Ge faceting motif, which will be discussed in more detail below.

5.3 Two-dimensional x-ray reflectivity from faceted surfaces

A systematic precise study of the faceting angles was performed using XRR. The Ge/graphene surface produces specular x-ray reflections from the facets that form during the growth of the graphene layer. Reflectivity measurements can be interpreted with geometric optics in methods similar to previous studies of faceting of Si surfaces.[12, 16] These methods must be adapted for the use of large-area two-dimensional x-ray detectors that permit the collection of intensity data from multiple surface truncation rods simultaneously.

XRR measurements were performed with a Bruker D8 Discover with a VÅNTEC 500 Area Detector in a theta-theta geometry with the detector subtending an opening angle of 39°. A Bruker IμS microfocus x-ray source was operated at 50 W to produce a Cu kα incident x-ray beam with a flux estimated to be 2.3×10^7 counts per second and a beam divergence of 0.03°. The incident beam had a diameter of 0.5 mm, which was sufficiently small to ensure that the incident beam footprint was never larger than the dimensions of the sample, but sufficiently large to gain ensemble information about the faceting.

In XRR measurements of planar surfaces, a theta-two theta scan is performed to measure the scattered intensity along the specular rod of reciprocal space with scattered wavevector (0, 0, q_z).[17] The faceted Ge surface presents a more complex XRR problem. Here the special case in which the footprint of the incident x-ray beam lies along a [100] direction is considered. In this case, two of the facets of the Ge/graphene surface are illuminated at sufficiently small angle to produce specular reflections. Intensities from these two facets as well as from small areas retaining the (001) orientation lead to the creation of three surface rods simultaneously.

The geometrical arrangement of the XRR measurement is shown in Figure 5-2. The sample surface orientation is defined as a function of several angles. The surface normal of the average sample surface, denoted n_{avg}, serves as the φ axis. A rotation around n_{avg} is denoted by angle φ. The θ axis is fixed normal to the φ axis. The incident beam is normal to the θ axis and

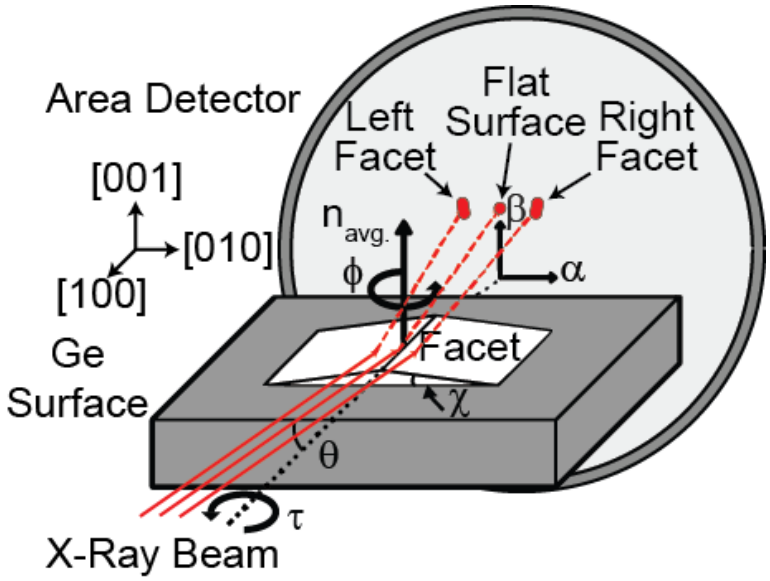

Figure 5-2: Schematic of the geometry of the x-ray experiment. Reflected x-rays form three distinct spots: one from the right facet, one from the left facet, and one from the flat surface. The geometry of the problem is defined by three angles. The x-ray incident angle relative to the average surface is given by θ. The total angle of the reflecting plane is τ and φ is the angle of azimuthal sample rotation around the average surface normal. The angle χ defines the angle of the facet with respect to the average surface. The angular location of the reflected x-ray beams is given by the angles α and β.

moves with θ. Thus a right handed coordinate system can be defined in which the θ axis is in the x direction, the φ axis is in the y direction, and the z direction is the beam direction at $\theta = 0°$. The tilt angle τ is defined as the angle between the surface normal of the reflecting facet and the phi axis. The τ axis is normal to the φ axis and rotates with φ. The tilt angle τ is the sum of the angle of the facets on the surface χ and a small rotation of the sample around an axis parallel to the beam axis at $\theta = 0°$.[12] This small misorientation of the sample with respect to the incident beam causes the left and right facets to appear to have slightly different values of τ, an effect which will be discussed further below. The angular locations of the reflections on the x-ray detector are measured as angles α and β, the azimuthal and polar elevation with respect to the incident beam, respectively. α is the angular location of the x-ray reflection measured around an axis normal to the incident beam and in the same plane as the ϕ axis. Note that the ϕ axis tilts as θ changes. β is the angular location of the reflection measured around a fixed axis coincident with the θ axis. The values $\alpha = \beta = 0$ corresponds to the location of the direct x-ray beam on the detector, indicated schematically by a transmitted beam spot in Figure 5-2. These angles can in turn be used to determine the orientation of the surface from which the x-rays are reflected. The surface facets are assumed to be oriented approximately along the incident beam footprint with a small azimuthal misorientation φ (Figure 5-2). With these definitions, the detector angles α and β can be expressed as:

$$\alpha(\theta, \tau, \varphi) = -\tan^{-1}\left[\frac{2\cos\varphi\ \sin\tau\ (\cos\theta\ \sin\tau\sin\varphi + \cos\tau\sin\theta)}{-1 + 2\cos^2\theta\sin^2\tau\ \sin^2\varphi + 2\cos^2\tau\ \sin^2\theta + \sin 2\tau\ \sin\varphi\sin 2\theta}\right]$$

Equation 5-1

$$\beta(\theta, \tau, \varphi) = \sin^{-1}[2(\cos\theta \sin\tau \sin\varphi + \cos\tau \sin\theta)(\cos\tau \cos\theta - \sin\tau \sin\varphi \sin\theta)]$$

Equation 5-2

In the case where the azimuthal angle φ is zero, such that the direction of the x-ray beam is along the long axis of the facets, the relationship then simplifies to:

$$\alpha(\theta, \tau) = \tan^{-1}[\frac{2\sin\tau \cos\tau \ \sin\theta])}{1 - 2\cos^2\tau \ \sin^2\theta}]$$

Equation 5-3

$$\beta(\theta, \tau) = \sin^{-1}[2\cos^2\tau \cos\theta \sin\theta]$$

Equation 5-4

When the small angle approximation is applied to θ and τ, the relationship further simplifies to:

$$\alpha(\theta, \tau) = \frac{2\tau\theta(-2 + \tau^2)}{-2 + \theta^2(-2 + \tau^2)^2}$$

Equation 5-5

$$\beta(\theta, \tau) = -\frac{1}{4}\theta(-2 + \theta^2)(-2 + \tau^2)^2$$

Equation 5-6

With these relationships, the tilt angle, τ, can be calculated from the position of the reflection on the detector by substituting measured values of α and β into equations (3) and (4) and numerically solving the system of equations for θ and τ.

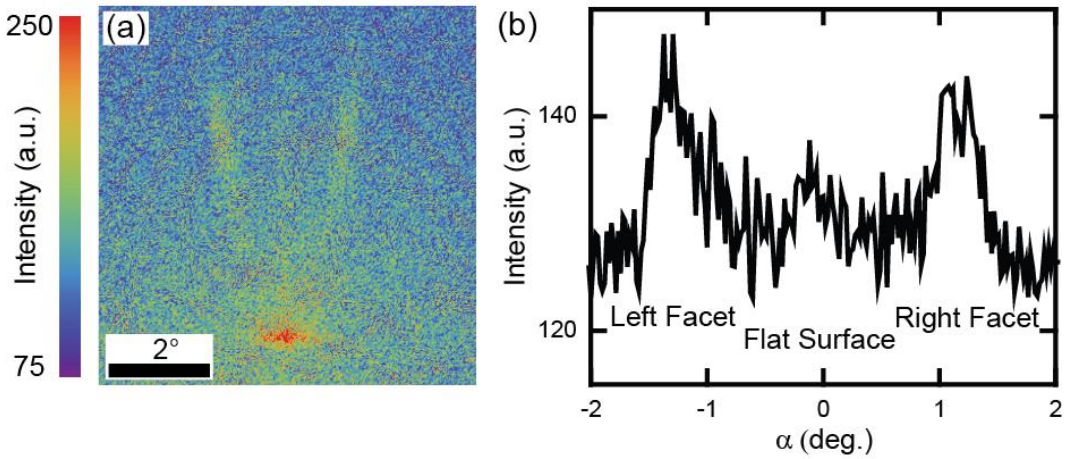

Figure 5-3: (a) X-ray scattering pattern acquired with an incident angle of 4°, from the Ge/graphene sample grown at 910 °C. The center streak is the x-ray reflection from the portion of the surface aligned with the average surface. The left and right streaks arise from reflections from the left and right facets. (b) Intensity profile taken horizontally across the image in (a).

A detector image and a reflectivity profile extracted along the horizontal direction across the image are shown in Figure 5-3 (a) and (b), respectively. The three intensity maxima in the detector image comprise two reflections from the facets (the maxima to the left and to the right of the center of the image) and a single central reflection from unfaceted regions in which the local surface normal is oriented along the average macroscopic surface normal.[12] In comparison, the reflectivity of the starting, unfaceted Ge surface produces a detector image consisting of a single sharp high-intensity reflection.

5.4 Surface faceting angle dependence on growth temperature

The in-plane symmetry of the faceted surface was probed by studying the XRR as a function of the azimuthal orientation of the sample. A series of scattering patterns were acquired at values of the azimuthal angle φ ranging from 0° to 360° with an incident angle θ=2° and exposure times of 30 seconds per pattern. Maxima in the total reflected intensity from a region of interest which includes the scattering from the flat surface and right and left facets are observed at multiples of 90°, as shown in Figure 5-4 (a). The reflection from the flat surface

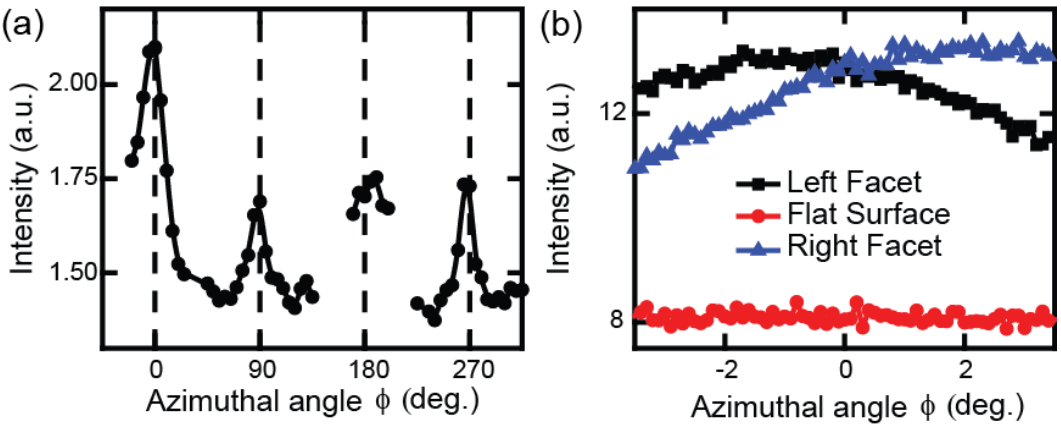

Figure 5-4: (a) Azimuthal (φ) data showing that the maxima in the total reflected intensity, from a region which includes the reflectivity from the flat surface and right and left facets, are observed at multiples of 90°. The reflection from the flat surface appears throughout the 360° scan, while the reflection for the right and left facets appears and disappears every 90°. (b) Intensities of the right, left, and center streak as function of the azimuthal angle φ over a narrow range. With the assumption that there is equal population of right and left facets, alignment of the x-ray beam with the long axis of the faceting occurs at the point at which the intensities of the scattering from the right and left facets are equal.

appears throughout the 360° scan, while the reflection for the right and left facets appears and disappears at 90° increments. The surface thus has four-fold symmetry, with the facets preferentially oriented close to the <100> directions of the Ge (001) substrate.[2] A similar four-fold symmetry is apparent in the SEM and AFM images in Figure 5-1 (a) and (b). Figure 5-4 (b) shows the intensity of each streak as a function of a very narrow range in φ. The intensity of each of the individual reflections from the facets varies in this narrow range because the effective incident angle with respect to the facets is changing. Figure 5-4 (b) was used to determine the alignment of the sample in which the long axis of the facet is precisely parallel to the projection of the x-ray beam on the surface, taking φ=0 as the point of equal intensities of the two reflections.

Precise measurements of the faceting angles were performed by examining the variation of the angular positions of the reflected beams as a function of the x-ray incident angle. A series of detector images was collected at values of the incident angle θ from 4° to 5.5° in 0.5°

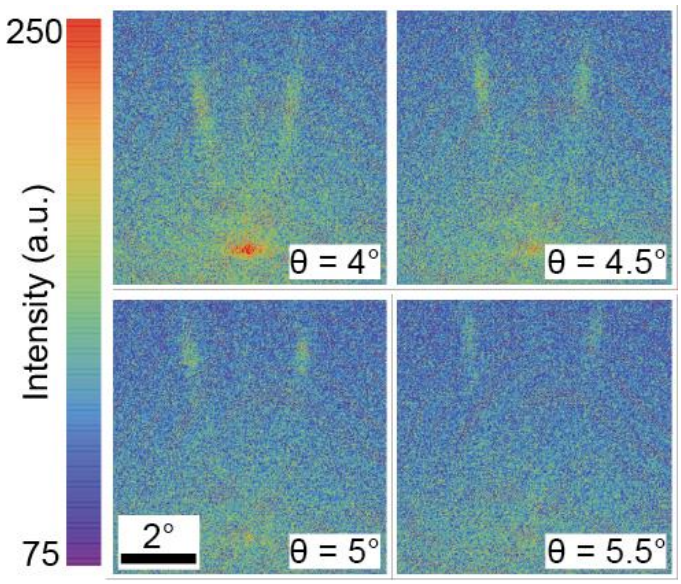

Figure 5-5: Detector images at the indicated incident angles from Ge/graphene grown at 910 ℃.

increments. These measurements were conducted at the angle set as φ=0 in Figure 5-4. The value of θ in this case is far larger than the critical angle for total external reflection, θ_c=0.32°, and the intensity for each reflected beam is thus several orders of magnitude weaker than the incident beam. The images were acquired using exposure times of 3600 seconds. The series of detector images for the sample grown at 910 °C is shown in Figure 5-5. Two reflections, one from each of the two facets illuminated at small angle at φ=0, move to higher angles and decrease in intensity as θ increases. A faint streak of intensity from the flat surface can be observed between the two facet streaks.

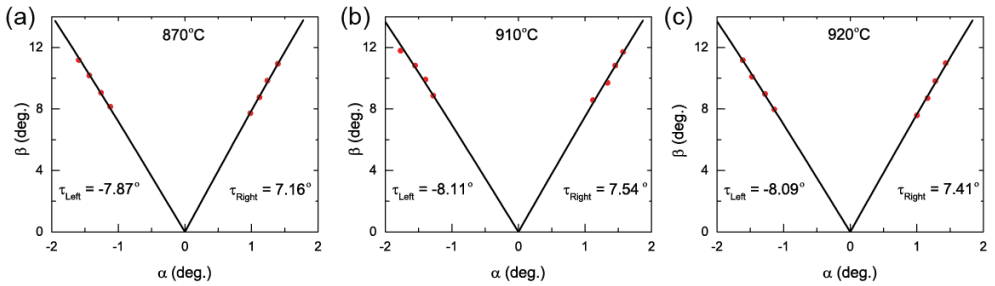

Figure 5-6: Angular positions α and β of x-ray reflections for samples grown at (a) 870 ℃, (b) 910 ℃, and (c) 920 ℃. The solid black lines are α and β for the total tilt angle χ of each reflection averaged over all incident angles.

The facet angle can be determined from the detector images by examining the dependence of the locations of the intense reflections, α and β, on the incident angle θ. Figure 5-6 shows the angles α and β associated with the point of maximum intensity of the reflections from the facets of samples grown at different temperatures. Each set of values of α and β are used to determine the precise values of θ and τ using Equation 5-3 and Equation 5-4 above. The angles listed on Table 5-1 are the total misorientation designated as the tilt angle τ, which includes both the crystallographic angle of the facet and the misorientation of the sample. The measured values of α and β and the corresponding fit values of θ and τ for each temperature and incident angle are shown in Table 5-1.

Table 5-1: The measured values of α *and* β *and the corresponding fit values of* θ *and* τ *for each temperature and incident angle.*

Growth Temperature	**Facet**	**Measured α(°)**	**Measured β (°)**	**Fit θ (°)**	**Fit τ (°)**
870°C	Left	-1.12	8.15	4.15	-7.76
		-1.26	9.05	4.61	-7.83
		-1.44	10.18	5.19	-7.91
		-1.59	11.18	5.70	-7.97
	Right	0.98	7.72	3.92	7.20
		1.12	8.76	4.45	7.21
		1.24	9.83	4.99	7.08
		1.40	10.94	5.56	7.15

910°C	Left	-1.28	8.86	4.52	-8.12
		-1.40	9.91	5.05	-7.91
		-1.55	10.82	5.52	-8.04
		-1.77	11.79	6.02	-8.37
	Right	1.12	8.57	4.36	7.38
		1.34	9.70	4.94	7.75
		1.46	10.82	5.51	7.53
		1.57	11.71	5.96	7.50
920°C	Left	-1.14	7.97	4.07	-8.07
		-1.28	8.97	4.58	-8.02
		-1.48	10.10	5.16	-8.19
		-1.61	11.16	5.70	-8.08
	Right	1.00	7.59	3.86	7.47
		1.16	8.70	4.43	7.51
		1.28	9.82	4.99	7.32
		1.44	10.97	5.58	7.33

The tilt angle τ is determined for each individual point with an accuracy that systematically increases with increasing θ, ranging from $\Delta\tau$=0.4° at θ=4° to $\Delta\tau$=0.3° at θ=5.5° for the sample grown at 910 °C. The fit curves plotted in Figure 5-6 are calculated as a function of θ for the given average τ for each facet.

The values from the individual points from different θ are averaged to determine the average tilt angle for the right and left facets, which reduces the uncertainty significantly. For example, in the case of the 910 °C the uncertainty in the average value is ± 0.16° . The two values of the tilt angle τ for the right and left facet are then averaged to determine the average tilt angle for a sample grown at the given temperature. The error in average tilt angle for a given temperature is reduced to ± 0.12°.

The average value of τ for the two facets is plotted in Figure 5-7 as a function of the growth temperature. The error bars are computed by propagating the single measurement error. The horizontal dashed lines indicate the facet angle of the nearest {10L} facets to the data. A

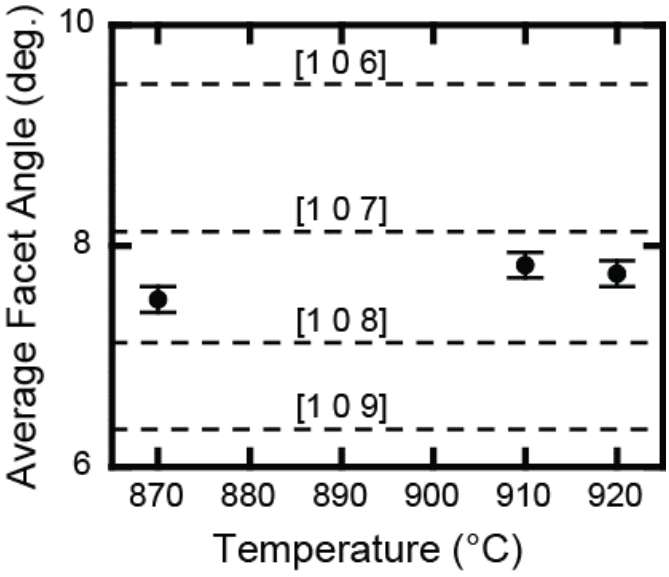

Figure 5-7: Temperature dependence of facet angles. Horizontal dashed lines are angles of the {1 0 L} family of crystal facets.

slight variation of the faceting angle with growth temperature is observed. At 870 °C, the facet angle is closest to the {108} facet at 7.13°, while the higher temperature points are closer to the {107} facet at 8.13°. These are both significantly different than the commonly observed {105} facet observed in Si-Ge systems.[6] This growth regime (870°C - 920°C) was chosen because it is the regime over which high-quality monolayer graphene growth is achieved, as indicated by Raman spectroscopy. Specifically, the Raman D:G ratio was negligible (less than 0.1) over this temperature range, indicating a low defect density. The trend in the faceting angle with temperature suggests that while the faceting process is dominated by the energetics of the crystal surface, kinetic processes, such as limiting the growth rate to allow for surface diffusion, still play a role in the formation of facets in this temperature regime.

A further question is whether or not all facet angles are equal or if the angles of the four sets of facets apparent in Figure 5-1 are slightly different. For example, a physical difference in angle can arise from the effects of stresses due to sample miscut. If all facet angles are equivalent, however, a difference between the apparent values of τ can also arise from a small overall misorientation of the sample with respect to the incident beam. To investigate this, the average value of τ from the two facets is compared to the τ value for the reflection from the flat surface for the sample grown at 910 °C. The average value of the right and left facet is τ = -0.29° ± 0.12° compared to τ = -0.52° ± 0.21° for the flat surface. These two values are the same within error, and the angles of the left and right facet are thus identical within the resolution of the measurement. Hence, the average value of τ for a given sample is the angle (χ) of the surface facets. The mean value of all of the samples is 7.7°±0.07°.

While reflectivity from the starting planar Ge surface appears as a single spot on the x-ray detector consistent with the incident beam profile, the reflectivity from these faceted surfaces is elongated into streaks of intensity. The length and width of the streaks on the detector provide insight into the angular distribution of the surface facets. In the limiting case of zero roughness, the length of the streaks along their long axis can be explained by a distribution in facet orientations in a combination of the θ and φ angles. By taking the angular derivative of Equation 5-4, it is shown that the angular extent of the streak is twice the change in θ. The sample grown at 910 °C, has an angular width corresponding to a variation in θ of 0.30° ± 0.02°. Similarly, taking the angular derivative of Equation 5-2 shows that the angular extent of the streak given by 1/4 times the range of φ. The sample grown at 910 °C has an angular width corresponding to a variation in φ of 2.26° ± 0.17°. Thus, in the limit of zero surface roughness, the elongation of the streaks could be due to rotational disorder of the facets by as large as 0.30° in θ or as large as 2.26° in φ.

The width of the streaks perpendicular to their long axis can be explained by a distribution in facet orientations in the χ angles. Since χ varies with the same relationships as τ, taking the angular derivative of Equation 5-4 shows that the angular width of the streak is 0.136 times the change in χ at 4° and 0.188 times the change in χ at 5.5°. The sample grown at 910 °C has an angular width corresponding to a variation in χ of 1.14° ± 0.08°. However, it is unclear whether this distribution arises from variation within the individual facets or from variation between different facets. Additionally, while the model assumes sharp peaks and troughs with flat plateaus, it is possible that a more rounded hill-and-valley structure could account for the observed variation in the facet angle. The presentation of the reflectivity as streaks provides insight into the surface homogeneity over a large length scale.

Table 5-2 shows the angular widths of the facet reflections as a function of sample growth temperature. As sample growth temperature increases, the distribution of facet orientations narrows, suggesting that the higher growth temperature allows the system to reach a state closer to its thermodynamically favored state.

Table 5-2: The angular widths of the facet reflections as a function of sample growth temperature.

Growth Temperature	**870°C**	**910°C**	**920°C**
Variation in θ	0.28° ± 0.01°	0.30° ± 0.02°	0.22° ± 0.01°
Variation in φ	2.47° ± 0.09°	2.26° ± 0.17°	1.85° ± 0.11°
Variation in χ	1.05° ± 0.11°	1.15° ± 0.08°	0.85° ± 0.06°

5.5 Surface faceting angle dependence on cooling rate

Further insight into the interplay between kinetics and thermodynamics at the Ge/graphene interface is obtained by varying the rate at which the sample is cooled after growth.

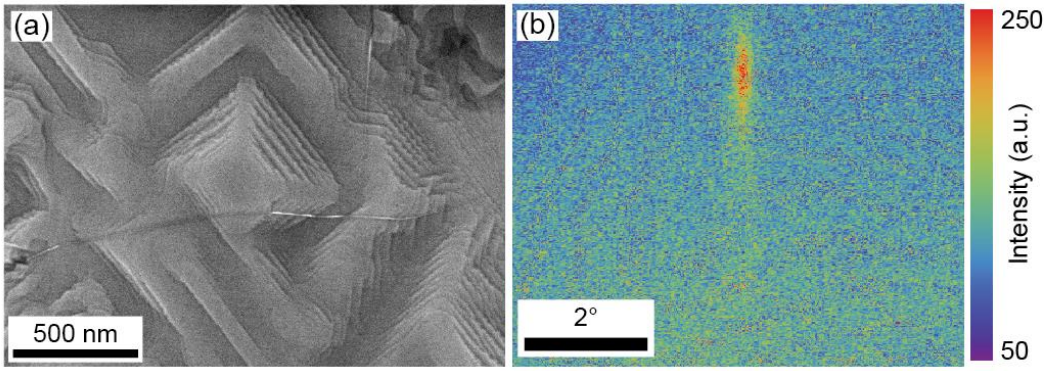

Figure 5-8: SEM image of Ge surface after slow cooling. In the case of slow cooling, the surface is a terraced structure. (b) X-ray reflectivity pattern from a sample which was slowly cooled. The angled streaks observed from the hill-and-valley structure are absent, as would be expected from a terraced structure composed of a (001) faceted surface.

A SEM image of the Ge surface for a sample cooled at 0.5 °C/min, is shown in Figure 5-8 (a). If a slow cool rate is used, the surface adopts a terraced structure instead of the hill-and-valley structure observed using faster cooling rates. A reflectivity pattern from the terraced structure is shown in Figure 5-8 (b). The reflectivity pattern shows an elongated streak from the (001) oriented surface and there is no evidence of reflectivity from angled facets. We hypothesize that during the previously discussed, fast cooling process, the facets are quenched into place. However, when a relatively slow cooling rate is used, the temperature decreases below the value at which the {107} facets are stable, and the (001) facets are favored. It was previously shown that the faceted Ge surface becomes atomically-flat after annealing at 800 °C.[2] Thus, we believe that the temperature at which the {107} facets becomes more energetically-favorable than the (001) facet is between 800 and 870 °C. It is not yet clear if other transitions exist between these two temperatures. The formation of the terraced structure implies that the faceting is kinetically-limited by surface diffusion. At lower temperatures, the germanium diffusion length during the cooling time is short, leading to the formation of terraces rather than a planar (001) surface.

5.6 Conclusions

The underlying Ge (001) surface facets beneath the graphene layer during growth to form a four-fold symmetric faceted surface structure. The faceting is symmetric with a faceting angle of 7.7°±0.07°, corresponding to the {107} facet of Ge. The angular distribution of facet angles could arise from a rotational disorder of the facets by as large as 0.30° in θ or as large as 2.26° in φ. The facet angle and angular distributions vary slightly with temperature in the growth regime indicating that the faceting of Ge(001) during graphene growth is dominated by the surface energetics. However, the slight dependence and the development of a terraced structure as a

result of a reducing the cooling rate after growth indicates that there is a strong competition with surface diffusion kinetics, with a transition temperature between 800 and 870 °C.

Substrate faceting is closely linked with the formation of high quality 2D materials. Within the last year, faceting of Cu, Ge, Ir, and SiC have all been shown to be advantageous for the growth of high quality and large area graphene monolayers.[18–21] Understanding the fundamental surface energetics and kinetics at work in graphene/substrate systems holds the key to property improvement and device commercialization. XRR techniques offer key insights into the competition between energetics and kinetics at the 2D material/substrate interface. The techniques developed here are also readily extensible to in-situ measurements to probe the growth dynamics with unprecedented spatial and temporal resolution.

5.7 References

1. Madey, T. E., Chen, W., Wang, H., Kaghazchi, P. & Jacob, T. Nanoscale surface chemistry over faceted substrates: structure, reactivity and nanotemplates. *Chem. Soc. Rev.* **37,** 2310–2327 (2008).
2. Jacobberger, R. M. *et al.* Direct oriented growth of armchair graphene nanoribbons on germanium. *Nat Commun* **6,** 8006 (2015).
3. Wang, G. *et al.* Direct growth of graphene film on germanium substrate. *Sci. Rep.* **3,** 2465 (2013).
4. Lippert, G. *et al.* Graphene grown on Ge(0 0 1) from atomic source. *Carbon* **75,** 104–112 (2014).
5. Mo, Y.-W., Swartzentruber, B. S., Kariotis, R., Webb, M. B. & Lagally, M. G. Growth and equilibrium structures in the epitaxy of Si on Si(001). *Phys. Rev. Lett.* **63,** 2393–2396 (1989).
6. Lu, G.-H. & Liu, F. Towards quantitative understanding of formation and stability of Ge hut islands on Si(001). *Phys. Rev. Lett.* **94,** 176103 (2005).
7. Bratland, K. A. *et al.* Sn-mediated Ge⁄Ge(001) growth by low-temperature molecular-beam epitaxy: Surface smoothening and enhanced epitaxial thickness. *J. Appl. Phys.* **97,** 044904 (2005).
8. Shklyaev, O. E., Beck, M. J., Asta, M., Miksis, M. J. & Voorhees, P. W. Role of strain-dependent surface energies in Ge/Si(100) island formation. *Phys. Rev. Lett.* **94,** 176102 (2005).
9. Held, G. & Brock, J. Calculation of x-ray-diffraction profiles from vicinal surfaces. *Phys. Rev. B* **51,** 7262–7268 (1995).

10. Ocko, B. & Mochrie, S. Reversible faceting of the copper (110) surface: X-ray Fresnel reflectivity. *Phys. Rev. B* **38,** 7378–7384 (1988).

11. Song, S., Mochrie, S. & Stephenson, G. Faceting kinetics of stepped Si(113) surfaces: A time-resolved x-ray scattering study. *Phys. Rev. Lett.* **74,** 5240–5243 (1995).

12. Song, S., Yoon, M. & Mochrie, S. G. J. Faceting, tricriticality, and attractive interactions between steps in the orientational phase diagram of silicon surfaces between [113] and [55 12]. *Surf. Sci.* **334,** 153–169 (1995).

13. Song, S., Yoon, M., Mochrie, S. G. J., Stephenson, G. B. & Milner, S. T. Faceting kinetics of stepped Si(113) surfaces: Dynamic scaling and nano-scale grooves. *Surf. Sci.* **372,** 37–63 (1997).

14. Watson, G. *et al.* Faceting and reconstruction of stepped Au(111). *Phys. Rev. B* **52,** 12329–12344 (1995).

15. Watson, G., Gibbs, D., Zehner, D., Yoon, M. & Mochrie, S. Faceting transformations of the stepped Pt(001) surface. *Phys. Rev. Lett.* **71,** 3166–3169 (1993).

16. Song, S. & Mochrie, S. G. J. Attractive step-step interactions, tricriticality, and faceting in the orientational phase diagram of silicon surfaces between [113] and [114]. *Phys. Rev. B* **51,** 10068–10084 (1995).

17. Jens Als-Nielsen & Des McMorrow. *Elements of Modern X-ray Physics*. (John Wiley & Sons, Ltd, 2011).

18. Lee, H. C. *et al.* Facet-mediated growth of high-quality monolayer graphene on arbitrarily rough copper surfaces. *Adv. Mater.* **28,** 2010–2017 (2016).

19. Pasternak, I. *et al.* Large-area high-quality graphene on Ge(001)/Si(001) substrates. *Nanoscale* **8,** 11241–11247 (2016).

20. Šrut Rakić, I. *et al.* Step-induced faceting and related electronic effects for graphene on Ir(332). *Carbon* **110,** 267–277 (2016).

21. Galves, L. A. *et al.* The effect of the SiC(0001) surface morphology on the growth of epitaxial mono-layer graphene nanoribbons. *Carbon* **115,** 162–168 (2017).